Hiroyuki Yoshida
Wenli Cai (Eds.)

Virtual Colonoscopy and Abdominal Imaging

Computational Challenges and Clinical Opportunities

Second International Workshop
Held in Conjunction with MICCAI 2010
Beijing, China, September 2010, Revised Selected Papers

LNCS 6668

Springer

Lecture Notes in Computer Science 6668

Commenced Publication in 1973
Founding and Former Series Editors:
Gerhard Goos, Juris Hartmanis, and Jan van Leeuwen

Hiroyuki Yoshida Wenli Cai (Eds.)

Virtual Colonoscopy and Abdominal Imaging

Computational Challenges and Clinical Opportunities

Second International Workshop
Held in Conjunction with MICCAI 2010
Beijing, China, September 20, 2010
Revised Selected Papers

Springer

Volume Editors

Hiroyuki Yoshida
Massachusetts General Hospital and Harvard Medical School
3D Imaging Research, Department of Radiology
25 New Chardon Street, Suite 400C, Boston, MA 02114, USA
E-mail: yoshida.hiro@mgh.harvard.edu

Wenli Cai
Massachusetts General Hospital and Harvard Medical School
3D Imaging Research, Department of Radiology
25 New Chardon Street, Suite 400C, Boston, MA 02114, USA
E-mail: cai.wenli@mgh.harvard.edu

ISSN 0302-9743 e-ISSN 1611-3349
ISBN 978-3-642-25718-6 e-ISBN 978-3-642-25719-3
DOI 10.1007/978-3-642-25719-3
Springer Heidelberg Dordrecht London New York

Library of Congress Control Number: Applied for

CR Subject Classification (1998): J.3, I.4, H.5.2, I.5, I.2.10, I.3.5

LNCS Sublibrary: SL 6 – Image Processing, Computer Vision, Pattern Recognition, and Graphics

Typesetting: Camera-ready by author, data conversion by Scientific Publishing Services, Chennai, India

Printed on acid-free paper

Springer is part of Springer Science+Business Media (www.springer.com)

Preface

The Second International Workshop on Computational Challenges and Clinical Opportunities in Virtual Colonoscopy and Abdominal Imaging was held in conjunction with the 13th International Conference on Medical Image Computing and Computer-Assisted Intervention (MICCAI) on September 20, 2010 in Beijing, China.

The purpose of this international workshop was to provide a comprehensive forum by bringing together world-class researchers in the fields of virtual colonoscopy (also known as CT colonography) and abdominal imaging to review state-of-the-art techniques and share novel and emerging analysis and visualization techniques in this rapidly growing field.

Recent large-scale, multicenter clinical trials conducted in several countries have demonstrated that virtual colonoscopy is an effective modality for screening colorectal cancer. Accordingly, computational and visualization requirements for virtual colonoscopy in clinical practice are becoming much more demanding, leading to the development of advanced techniques for fulfilling the new clinical needs. In parallel, there are increasing computational and visualization challenges in abdominal imaging, such as CT/MR enterography, segmentation and tumor characterization in the liver, kidney, and bladder. In these areas, organ and disease appearances are more complex and subtle, and thus computational complexity in image analysis is high. We thus solicited original and review papers addressing the computational challenges and clinical opportunities in virtual colonoscopy and abdominal imaging.

In response to the call for paper, a total of 26 papers were initially submitted to the workshop. They underwent a rigorous, double-blinded peer-review process, with each paper being reviewed by a minimum of two expert reviewers from the Scientific Review Committee. Based on the review results, 22 papers were accepted by the workshop. With an additional five invited lectures, the workshop accommodated a total of 24 oral presentations and three poster presentations. Among them, 19 papers were revised and re-submitted by the authors as proceedings papers to be included in this Virtual Colonoscopy and Abdominal Imaging proceedings volume.

We would like to express our sincere appreciation to the authors whose contributions to this proceedings book have required considerable commitments of time and effort. We also thank Wenli Cai and Jianhua Yao, the General Chairs of the workshop, for their outstanding job in organizing the workshop program, and Hongbing Lu for her excellent job in the on-site organization of the workshop.

September 2011

Hiroyuki Yoshida
Wenli Cai

Workshop Organization

General Chairs

Wenli Cai	Massachusetts General Hospital / Harvard Medical School, USA
Jianhua Yao	National Institutes of Health, USA

Local Organizer

Hongbing Lu	Fourth Military Medical University, China

Organizing Committee

Wenli Cai	Massachusetts General Hospital / Harvard Medical School, USA
Jerome Liang	State University of New York at Stony Brook, USA
Hongbing Lu	Fourth Military Medical University, China
Janne Nappi	Massachusetts General Hospital / Harvard Medical School, USA
Ronald Summers	National Institutes of Health, USA
Kenji Suzuki	University of Chicago, USA
Jianhua Yao	National Institutes of Health, USA
Hiroyuki Yoshida	Massachusetts General Hospital / Harvard Medical School, USA

Workshop Committee

Jamshid Dehmeshki	Kingston University, UK
Joel G. Fletcher	Mayo Clinic, USA
Stefaan Gryspeerdt	Stedelijk Ziekenhuis, Belgium
Kenneth R. Hoffmann	University at Buffalo, USA
Gen Iinuma	National Cancer Center, Japan
Lakhmi C. Jain	University of South Australia, Australia
Arie E. Kaufman	Stony Brook University, USA
Ron Kikinis	Brigham and Women's Hospital / Harvard Medical School, USA
Se Hyung Kim	Seoul National University Hospital, Korea
Kensaku Mori	Nagoya University, Japan
Sandy Napel	Stanford University, USA
Emanuele Neri	University of Pisa, Italy
Noboru Niki	Tokushima University, Japan

Yoshinobu Sato	Osaka University, Japan
Jay Tian	Chinese Academy of Sciences, China
Frans Voss	Delft University of Technology, The Netherlands

Scientific Review Committee

Wenli Cai	Massachusetts General Hospital / Harvard Medical School, USA
Jerome Liang	State University of New York at Stony Brook, USA
Hongbing Lu	Fourth Military Medical University, China
Kenneth R. Hoffmann	University at Buffalo, USA
Janne Nappi	Massachusetts General Hospital / Harvard Medical School, USA
Kenji Suzuki	University of Chicago, USA
Frans Voss	Delft University of Technology, The Netherlands
Jianhua Yao	National Institutes of Health, USA
Hiroyuki Yoshida	Massachusetts General Hospital / Harvard Medical School, USA

Proceedings Editors

Hiroyuki Yoshida	Massachusetts General Hospital / Harvard Medical School, USA
Wenli Cai	Massachusetts General Hospital / Harvard Medical School, USA

Table of Contents

CT Colonography CAD

Abdominal Imaging

Virtual Colonoscopy

Electronic Cleansing in CT Colonography: Past, Present, and Future

Wenli Cai and Hiroyuki Yoshida

Massachusetts General Hospital and Harvard Medical School,
25 New Chardon Street, 400C,
Boston, MA 02114, USA
{cai.wenli,yoshida.hiro}@mgh.harvard.edu

Abstract. Fecal tagging is a means of 'marking' fecal residues (stool and fluid) in a colon by use of the oral administration of a positive contrast agent (barium or iodine) in CT Colonography (CTC). Electronic cleansing (EC) is an emerging technique for removal of tagged fecal materials in fecal tagging CTC images after the image acquisition, and thus to avoid the physical bowel cleansing prior to CT scanning. In this syllabus, we present a brief overview about the past, present, and the future developments of EC technology in fecal tagging CTC.

Keywords: CT colonography, fecal tagging, electronic cleansing, bowel preparation.

1 Introduction

CT colonography (CTC), also known as virtual colonoscopy, is a promising technique for non-invasive colon cancer screening that can be an alternative to optical colonoscopy [1, 2]. Fecal tagging is an emerging method of tagging stool and fluid remaining in the colon by a radiopaque oral contrast agent for effectively differentiating them from colonic polyps [3-5]. Electronic cleansing (EC) is an emerging technique for removal of tagged fecal materials in fecal tagging CTC images, effectively cleansing the colon after image acquisition [6-8]. EC "virtually cleanses" the tagged fecal materials that can obscure the colonial mucosal surface, especially small lesions that are submerged in or adjacent to the tagged materials.

2 Fecal-Tagging CTC

A well-cleansed and well-distended colon, such as that shown in Figure 1a, which was prepared by physical bowel cleansing, is ideal for high-quality CTC examination, but is unfavorable for the patient. Fecal tagging is a means of 'marking' fecal residues (stool and fluid) in a colon by use of the oral administration of a positive contrast agent (barium or iodine). Fecal tagging for CTC is often combined with a certain amount of cathartic or laxative agent, such as sodium phosphate, bisacodyl, or

H. Yoshida et al. (Eds.): Virtual Colonoscopy and Abdominal Imaging 2010, LNCS 6668, pp. 1–8, 2011.

magnesium citrate, that draws fluid into the bowel lumen to induce peristalsis and eliminate bowel contents. There are three major types of bowel preparation for fecal tagging in CTC examination based upon the dose of catharsis applied: full-dose cathartic preparation (Figure 1b), reduced-dose cathartic preparation (Figure 1c), and non-cathartic preparation (Figure 1d).

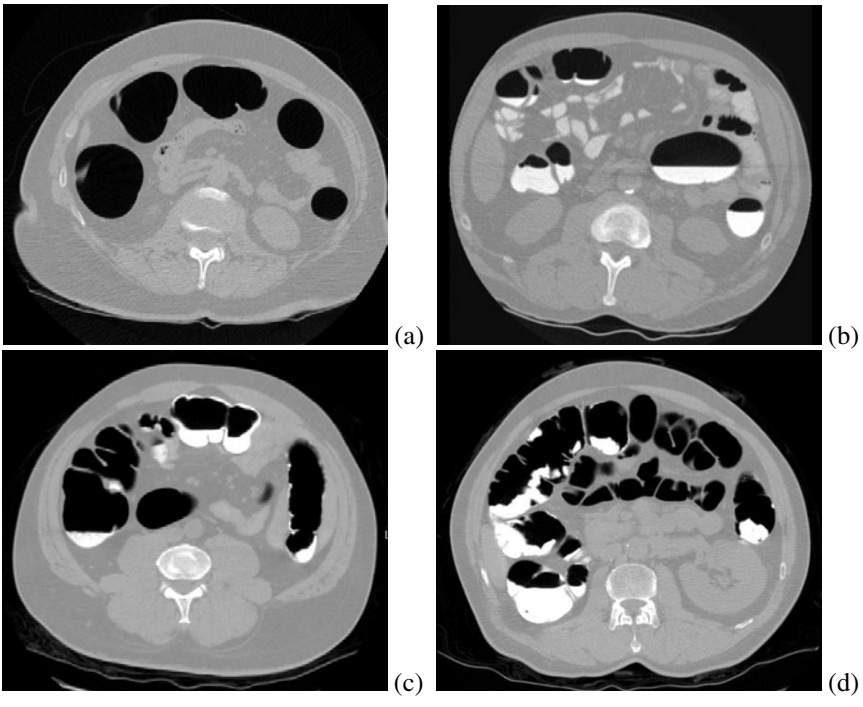

Fig. 1. Illustration of CTC images with different bowel preparations. (a) CTC image with a physically-cleansed and well-distended colon. (b) Fecal tagging CTC image with full-dose cathartic preparation. (c) Fecal tagging CTC image with reduced-dose cathartic preparation. (d) Fecal tagging CTC image with non-cathartic preparation. Same contrast agent, non-ionic iodine contrast agent (Omnipaque iohexol 300, GE Healthcare, Princeton, NJ), was employed in the bowel preparation of (b-d).

In addition to the perceived discomfort and inconvenience associated with full cathartic preparation, many studies have warned of potential problems associated with the full cathartic preparation, including renal failure, preexisting electrolyte abnormalities, congestive heart failure, ascites, or ileus [9-11]. Thus, clinical investigators have been investigating for reduced- or non-cathartic methods that can offer patients a well-tolerated and safely performed bowel preparation while providing a sensitivity/specificity similar to that of full cathartic preparation in CTC examination [5, 12, 13]. In particular, non-cathartic fecal-tagging CTC (or for short: non-cathartic CTC), also known as laxative-free CTC, is regarded as a promising

next-generation fecal-tagging CTC technique for eliminating the patients' primary concerns about undergoing colon screening.

The goal of EC is the "virtual cleansing" of the colon by removal of the tagged fluids as well as the tagged semi-fluid/solid fecal materials in CTC images and generating "cleansed" images such as that shown in Figure 1a. Such an approach, called electronic cleansing (EC) of the colon, is a promising technique for applying CTC examination, especially for non-cathartic CTC, in colon cancer screening.

3 Early Work of EC

The early work on EC dates back to the late '90s [14-16]. The term "electronic cleansing" was first introduced by Wax and Liang at SUNY Stony Brook [14]. At its early stage, EC was designed to the removal of the tagged fluid in the cathartic fecal-tagging CTC, such as that shown in Figure 1b, based on the following EC assumptions:

- Tagged fluid appears as a bowl-shaped liquid pool located at the bottom of the colonic lumen due to the gravitational effect.
- Tagged fluid has a large, flat, horizontal surface contacting the colonic air lumen, named air-tagging boundary (AT-boundary).
- Tagging is homogeneous, i.e., the CT values within the fluid pool are almost constant.

Based on the above EC assumptions, there were two groups of EC methods developed in the early stage. The methods developed by SUNY's research group employed the classifier of tagged fluid by use of its statistical image features. Chen *et al.* used a Markov random field (MRF) for classification of each voxel by its local feature vector [17]. Li *et al.* reported an improvement by using a hidden MRF to integrate the neighborhood information for removal of non-uniformly tagged fluid [18].

Another group of EC methods used an edge model in image segmentation to delineate the tagged regions. Lakare *et al.* used segment rays to analyze the intensity profile as they traverse through the data set for identifying the boundary of tagged fluid [19]. Zalis *et al.* used the Sobel approximation of the image gradient, followed by a dilation operator, to identify the AT-boundaries of the tagged fluid [20]. Serlie *et al.* employed a three-material (air, soft tissue, and tagged fluid) transition model by using histogram analysis [21]. They also used the CT values and their gradient to characterize the boundary of tagged fluid.

Large-scale CTC trials, such as the National CT Colonography Trial (ACRIN 6664) [22], the US DoD screening trial by Pickhardt *et al.* [23], and the clinical trial by Kim *et al.* [24], which employed full cathartic bowel preparation aided by EC, have demonstrated that CTC yields a sensitivity comparable to that of optical colonoscopy in the detection of clinically significant polyps in a screening population.

4 Current Status of EC

In a recent large survey of 759 respondents ≥50 years old, one third (32%) identified the cathartic bowel preparation as the most troublesome part of colon cancer screening, and a significant number of patients would have the CTC more frequently if cathartic bowel preparation was not required [25]. Thus, clinical investigators recently started to employ the reduced- or non-cathartic bowel preparation in CTC that can offer patients a well-tolerated and safely performed bowel preparation while providing a sensitivity/specificity similar to that of full cathartic preparation in CTC examination [5, 12, 13].

However, the aforementioned EC assumptions do not sustain in the reduced- or non-cathartic CTC images, as observed in comparison of Figure 1 (c,d) with Figure 1b. The early EC methods that were developed for the cathartic CTC remain severely limited in removing irregularly shaped, randomly distributed, inhomogeneously tagged, semi-solid stool that is the typical fecal residue in non-cathartic CTC, and they tend to generate severe cleansing artifacts that impair the diagnostic utility of the electronically cleansed CTC images. Therefore, the following three types of cleansing artifacts persist with the prior EC methods, impairing the diagnostic utility of electronically cleansed CTC images, especially in non-cathartic CTC [26].

- *Soft-tissue structure degradation*: This type of artifact is caused by pseudo-enhancement due to the presence of adjacent high-radiodensity tagged materials [27, 28]. A part or the entirety of submerged soft-tissue structures are misclassified as tagged materials and thus are erroneously removed, resulting in degraded or eliminated folds or polyps.
- *Pseudo-soft-tissue structures and false fistula*: This type of artifact is caused by the partial volume effect at the AT-boundary: AT-boundaries are partially removed, generating pseudo soft-tissue structures, or soft-tissues are erroneously removed as AT-boundaries, making holes on a fold or on the colonic wall.
- Incomplete cleansing: This type of artifact is caused by the partial removal of tagged fecal materials that are semi-solid, heterogeneously mixtures of air bubbles, fat, undigested foodstuff, and an uneven distribution of the contrast agent.

Recent EC research has been focusing on the non-cathartic CTC studies. Along with their early work, Wang *et al.* presented a partial volume image segmentation method for classifying voxels that are composed of multiple materials [29]. Carston *et al.* used a neighborhood voxel-counting method to classify a voxel as stool, tissue, or air [30]. They later expanded their method to combine it with quadratic regression, morphologic operations, and a distance transform [31]. Although not strictly an EC method, Franaszek *et al.* used region growing, fuzzy connectedness, and Laplacian level-set methods for removal of tagged fluid to reveal polyps submerged in the tagged regions [32]. Cai *et al.* presented an structure-analysis (SA) cleansing method that used the local morphologic information to enhance fold-like and polyp-like structures submerged in the tagged materials, whereas other structures were de-enhanced and thus subtracted from the CTC images [33]. Recently, they proposed a

material decomposition (MD) cleansing method that decomposed the tagged regions into a set of local homogeneous regions by application of a 3D watershed transform and a SVM classifier to different material by use of the image textures [34].

Clinical trials on non-cathartic CTC are still limited. Johnson *et al.* first demonstrated that the non-cathartic CTC was similar in performance to cathartic CTC [35]. They also assessed the major artifacts encountered in the cleansed non-cathartic CTC images. A recent large-scale multi-center non-cathartic CTC trial by Zalis *et al.* demonstrated high sensitivity and specificity for adenoma detection in a screening cohort by use of the SA-cleansing method [42].

5 Future Challenges of EC

The quality of cleansed non-cathartic CTC images is still inferior compared to that of the cathartic CTC. Partial volume effect and tagging inhomogeneity are the major causes of EC artifacts, in particular in non-cathartic CTC. Current EC solutions are heuristic and thus provide only an incomplete solution to address these issues. The detection of the partial volume effect and material differentiation are traditional technical challenges in image processing.

The dual-energy CT (DECT) theory was first introduced by Alvarez and Macovski three decades ago [36, 37]. With the recent technical advances such as dual-source, ultrafast kVp switching and a dual-layer detector configuration, DECT scanners have significantly improved their image quality and become widely available for clinical use through top-of-the-line CT scanners from major manufacturers such as the SOMATOM Definition and Definition Flash (Siemens AG, Munich, Germany) [38] and LightSpeed CT750 HD (GE Healthcare, Chalfont St. Giles, UK) [39]. The material differentiation capability of DECT, i.e., the material composition can be estimated by analysis of the two attenuation values acquired simultaneously at two energies, works especially well in materials with large atomic numbers such as iodine—one of the commonly used contrast agents in non-cathartic CTC.

Thus, dual-energy CTC provides a promising solution for the challenges in EC caused by the partial volume effect and inhomogeneous tagging in residual fecal materials. Recently, Carmi *et al.* [40] and Cai *et al.* [41] independently developed EC schemes for dual-energy CTC images, and demonstrated that non-cathartic dual-energy CTC has the potential to improve significantly the quality of EC.

6 Conclusion

An EC-aided non-cathartic fecal-tagging CTC examination could substantially improve the screening compliance, safety, and capacity of colorectal screening, and thus to substantially increase the screening rate and the early detection of colonic polyps and cancers. Although the current EC schemes provide a solution to cathartic CTC, it is imperfect when they are applied to the non-cathartic CTC that is shown to be as effectiveness in detecting polyps as that of the cathartic CTC. Dual-energy CTC is an emerging and promising solution for the EC challenges in non-cathartic CTC.

Acknowledgments. This work was supported in part by Grant No. CA095279 and CA131718 from the US Public Health Service, and by Research Scholar Grant RSG-05-088-01-CCE from the American Cancer Society.

References

1. Morrin, M.M., LaMont, J.T.: Screening virtual colonoscopy—ready for prime time? N. Engl. J. Med. 349, 2261–2264 (2003)
2. Levin, B., Brooks, D., Smith, R.A., Stone, A.: Emerging technologies in screening for colorectal cancer: CT colonography, immunochemical fecal occult blood tests, and stool screening using molecular markers. CA Cancer J. Clin. 53, 44–55 (2003)
3. Callstrom, M.R., Johnson, C.D., Fletcher, J.G., et al.: CT colonography without cathartic preparation: feasibility study. Radiology 219, 693–698 (2001)
4. Zalis, M.: Patient Preparation. In: Dachman, A.H. (ed.) Atlas of Virtual Colonoscopy, pp. 33–36. Springer, New York (2003)
5. Lefere, P., Gryspeerdt, S., Baekelandt, M., Van Holsbeeck, B.: Laxative-free CT colonography. AJR Am. J. Roentgenol. 183, 945–948 (2004)
6. Zalis, M.E., Perumpillichira, J., Del Frate, C., Hahn, P.F.: CT colonography: digital subtraction bowel cleansing with mucosal reconstruction: initial observations. Radiology 226, 911–917 (2003)
7. Pickhardt, P.J., Choi, J.H.: Electronic cleansing and stool tagging in CT colonography: advantages and pitfalls with primary three-dimensional evaluation. AJR Am. J. Roentgenol. 181, 799–805 (2003)
8. Zalis, M.E., Magee, C., Perumpillichira, J.J., Blake, M.A., Sahani, D.V., Hahn, P.F.: Optimizing minimal preparation digital subtraction CT colonography: prospective comparison in 150 patients. Radiology 203(suppl.), 432 (2004)
9. Clarkston, W.K., Tsen, T.N., Dies, D.F., Schratz, C.L., Vaswani, S.K., Bjerregaard, P.: Oral sodium phosphate versus sulfate-free polyethylene glycol electrolyte lavage solution in outpatient preparation for colonoscopy: a prospective comparison. Gastrointest Endosc 43, 42–48 (1996)
10. Orias, M., Mahnensmith, R.L., Perazella, M.: Extreme hyperphosphatemia and acute renal failure after a phosphorus-containing bowel regimen. Am. J. Nephrol. 19, 60–63 (1999)
11. Beloosesky, Y., Grinblat, J., Weiss, A., Grosman, B., Gafter, U., Chagnac, A.: Electrolyte disorders following oral sodium phosphate administration for bowel cleansing in elderly patients. Arch. Intern. Med. 163, 803–808 (2003)
12. Iannaccone, R., Laghi, A., Catalano, C., et al.: Computed tomographic colonography without cathartic preparation for the detection of colorectal polyps. Gastroenterology 127, 1300–1311 (2004)
13. Johnson, K.T., Carston, M.J., Wentz, R.J., Manduca, A., Anderson, S.M., Johnson, C.D.: Development of a cathartic-free colorectal cancer screening test using virtual colonoscopy: a feasibility study. AJR Am. J. Roentgenol. 36, 29–36 (2007)
14. Wax, M., Liang, Z., Chiou, R., Kaufman, A., Viswambharan, A.: Electronic colon cleansing for virtual colonscopy. The 1st Symposium on Virtual Colonscopy 94 (1998)
15. Liang, Z., Yang, F., Wax, M., et al.: Inclusion of a priori information in segmentation of colon lumen for 3D virtual colonoscopy. In: IEEE Nuclear Science Society - Medical Imaging Conference, pp. 1423–1427 (1997)
16. Liang, Z., Chen, D., Chiou, R., et al.: On segmentation of colon lumen for virtual colonoscopy. SPIE Medical Imaging, 270–278 (1999)

17. Chen, D., Liang, Z., Wax, M.R., Li, L., Li, B., Kaufman, A.E.: A novel approach to extract colon lumen from CT images for virtual colonoscopy. IEEE Trans. Med. Imaging 19, 1220–1226 (2000)
18. Li, L., Chen, D., Lakare, S., et al.: An image segmentation approach to extract colon lumen through colonic material tagging and hidden markov random field model for virtual colonoscopy. SPIE Medical Imaging, 406–411 (2002)
19. Lakare, S., Chen, D., Li, L., Kaufman, A., Liang, Z.: Electronic colon cleansing using segmentation rays for virtual colonoscopy. SPIE Medical Imaging, 412–418 (2002)
20. Zalis, M.E., Perumpillichira, J., Hahn, P.F.: Digital subtraction bowel cleansing for CT colonography using morphological and linear filtration methods. IEEE Trans. Med. Imaging 23, 1335–1343 (2004)
21. Serlie, I.W., Truyen, R., Florie, J., Post, F.H., van Vliet, L.J., Vos, F.M.: Computed cleansing for virtual colonoscopy using a three-material transition model. In: Ellis, R.E., Peters, T.M. (eds.) MICCAI 2003. LNCS, vol. 2879, pp. 175–183. Springer, Heidelberg (2003)
22. Johnson, C.D., Chen, M.H., Toledano, A.Y., et al.: Accuracy of CT colonography for detection of large adenomas and cancers. N. Engl. J. Med. 359, 1207–1217 (2008)
23. Pickhardt, P.J., Choi, J.R., Hwang, I., et al.: Computed tomographic virtual colonoscopy to screen for colorectal neoplasia in asymptomatic adults. N. Engl. J. Med. 349, 2191–2200 (2003)
24. Kim, D.H., Pickhardt, P.J., Taylor, A.J., et al.: CT colonography versus colonoscopy for the detection of advanced neoplasia. The New England Journal of Medicine 357, 1403–1412 (2007)
25. Beebe, T.J., Johnson, C.D., Stoner, S.M., Anderson, K.J., Limburg, P.: Assessing attitudes toward laxative preparation in colorectal cancer screening and effects on future testing: potential receptivity to computed tomographic colonography. In: Mayo Clinic Proceedings, vol. 82, pp. 666–671 (2007)
26. Cai, W., Yoshida, H., Zalis, M.E., Nappi, J.J., Harris, G.: Informatics in Radiology: Electronic Cleansing for Non-cathartic CT Colonography: A Structure-Analysis Scheme. Radiographics (2010)
27. Heneghan, J.P., Spielmann, A.L., Sheafor, D.H., Kliewer, M.A., DeLong, D.M., Nelson, R.C.: Pseudoenhancement of simple renal cysts: a comparison of single and multidetector helical CT. Journal of Computer Assisted Tomography 26, 90–94 (2002)
28. Maki, D.D., Birnbaum, B.A., Chakraborty, D.P., Jacobs, J.E., Carvalho, B.M., Herman, G.T.: Renal cyst pseudoenhancement: beam-hardening effects on CT numbers. Radiology 213, 468–472 (1999)
29. Wang, Z., Liang, Z., Li, X., et al.: An improved electronic colon cleansing method for detection of colonic polyps by virtual colonoscopy. IEEE Transactions on Bio-Medical Engineering 53, 1635–1646 (2006)
30. Carston, M.J., Wentz, R.J., Manduca, A., Johnson, D.: CT colonography of the unprepraed colon: an evaluation of electronic stool subtraction. Medical Imaging 2005: Physiology, Function, and Structure from Medial Images 5746, 424–431 (2005)
31. Carston, M.J., Manduca, A., Johnson, D. Electornic stool subtraction using quadratic regression, morphological operations, and distance transform. Medical Imaging 2007: Physiology, Function, and Structure from Medical Images 2007; 6511:6511W 1-12.
32. Franaszek, M., Summers, R.M., Pickhardt, P.J., Choi, J.R.: Hybrid segmentation of colon filled with air and opacified fluid for CT colonography. IEEE Transactions on Medical Imaging 25, 358–368 (2006)

33. Cai, W., Zalis, M.E., Näppi, J., Harris, G.J., Yoshida, H.: Structure-analysis method for electronic cleansing in cathartic and noncathartic CT colonography. Med. Phys. 35, 3259–3277 (2008)
34. Cai, W., Zalis, M., Yoshida, H.: Mosaic decomposition method for detection and removal of inhomogeneously tagged regions in electronic cleansing for CT colonography. In: Proc. of SPIE 2008, vol. 6915 (2008)
35. Johnson, C.D., Manduca, A., Fletcher, J.G., et al.: Noncathartic CT colonography with stool tagging: performance with and without electronic stool subtraction. AJR Am. J. Roentgenol. 190, 361–366 (2008)
36. Macovski, A., Alvarez, R.E., Chan, J.L., Stonestrom, J.P., Zatz, L.M.: Energy dependent reconstruction in X-ray computerized tomography. Comput. Biol. Med. 6, 325–334 (1976)
37. Alvarez, R.E., Macovski, A.: Energy-selective reconstructions in X-ray computerised tomography. Phys. Med. Biol. 21, 733–744 (1976)
38. Flohr, T., McCollough, C., Bruder, H., et al.: First performance evaluation of a dual-source CT (DSCT) system. Eur. Radiol. 16, 1405–1405 (2006)
39. GE Healthcare - Computed Tomography - GE Lightspeed CT750HD, http://www.gehealthcare.com/euen/ct/products/products_technologies/750_HD/lspeed_750hd_index.html
40. Carmi, R., Kafri, G., Goshen, L., et al.: A unique noncathartic CT colonography approach by using two-layer dual-energy MDCT and a special algorithmic colon cleansing method. In: IEEE 2008 NSS-MIC Conference (2008), M10:132
41. Cai, W., Liu, B., Yoshida, H.: Dual-energy electronic cleansing scheme for non-cathartic CT Colonography: a phantom study. Radiological Society of North America Scientific Assembly and Annual Meeting Program (2009), 466-466-467
42. Zalis, M.E., Hahn, P.F., Blake, M.A., Perez-Johnston, R., Yoshida, H., Yee, J., et al.: Prospective Performance Evaluation of Non-cathartic, Computer-aided (CAD) CT Colonography (CTC) in a 615 Subject Screening Cohor. In: Radiological Society of North America Scientific Assembly and Annual Meeting Program (to appear), Radiological Society of North America, Oak Brook, IL (2010) (to appear)

Improved Curvature Estimation for Shape Analysis in Computer-Aided Detection of Colonic Polyps

Hongbin Zhu, Yi Fan, and Zhengrong Liang

Department of Radiology, State University of New York, Stony Brook, NY 11794, USA
{hbzhu,yifan,jzliang}@mil.sunysb.edu

Abstract. In current methods of computer-aided detection (CAD) of colonic polyps, curvature-based shape measures, like the shape index, curvedness, sphericity ratio, Gaussian curvature, mean curvature, etc., are widely used to analyze the local shapes in the colon wall. Therefore, the curvature estimation is an essential step, which is often conducted through kernel methods. However, spurious calculations indicating high curvature are frequently observed when the kernel contains two surfaces (this happens for objects like a thin slab, sphere, etc.). In this study, we adapted the Knutsson mapping method to solve this problem, so that we can improve the curvature estimation for CAD of colonic polyps in virtual colonoscopy.

Keywords: colonic polyps, computer-aided detection, shape analysis, curvature, Knutsson mapping.

1 Purpose

According to the up-to-date statistics from the American Cancer Society (ACS) [1], colorectal cancer ranked as the third most common occurrence of both cancer deaths and new cancer cases in 2008 for both men and women in the United States. Computer-aided detection (CAD) of colonic polyps (precursors of colon cancer) is emerging as a promising technique to help physicians in detecting polyps for diagnosis [2].

In most of the available CAD systems, principal curvatures, estimated through kernel methods [3, 4], are widely used for shape analysis to characterize colon polyps [2, 5-13]. The shape analysis is often conducted through principal curvatures directly [9] or through measures derived from them, such as the mean, Gaussian curvatures, and the sphericity ratio [2, 5, 8], as well as the shape index and curvedness [6, 7, 10-13]. However, spurious estimations of principal curvatures are observed when the kernel contains more than two surfaces [14]. This is due to the discontinuity at thin structures where the gradient magnitude is very small and even nearly zero. Fortunately, such a discontinuity problem can be solved with an existing method, i.e., mapping of the discontinuous orientation field to a continuous one through Knutsson mapping [15]. In this study, we applied the Knutsson mapping technique to estimate the principal curvatures in CTC images, and we focused on exploring the possible

H. Yoshida et al. (Eds.): Virtual Colonoscopy and Abdominal Imaging 2010, LNCS 6668, pp. 9–14, 2011.

benefits brought by such improved curvature estimation. Rigorous evaluations, based on both phantom study and real patient studies, were conducted to demonstrate the impact for CAD of colonic polyps.

2 Methods

In this section, we outline just three curvature estimation techniques, i.e., the Knutsson mapping method and two widely used kernel methods, for a self-contained presentation. The details of each technique are referred to in the related references. In this study, we focused on exploring the benefits for CAD of colonic polyps brought by the Knutsson mapping method by considering its immunity to the discontinuity problem, which has not been investigated yet in the literature.

2.1 Kernel Methods for Principal Curvature Estimation

In differential geometry [16], for any point on a smooth surface, any non-singular curve through the point on the surface will have its own tangent vector $\boldsymbol{T}$ lying in the tangent plane of the surface orthogonal to the normal vector. The curvature associated with $\boldsymbol{T}$ at the point is then defined as

$$k_T = k \cdot V, \tag{1}$$

where **k** is the curvature vector of the curve at the point, and $\boldsymbol{N}$ is the unit normal at the point on the surface. All non-singular curves with the same tangent vector $\boldsymbol{T}$ will have the same curvature k_T. Among all the possible tangent vectors, the maximum and minimum values of k_T at the point are called the *principal curvatures*, k_1 and k_2, and the directions of the corresponding tangent vectors are called *principal directions*.

To resolve the principal curvatures with computers for implicit surfaces (e.g., iso-surfaces) embedded in three-dimensional (3D) volume images, kernel methods were then developed [3, 4]. In [3], Equation (1) was rewritten as

$$k_T = -(\boldsymbol{T}^t M_H \boldsymbol{T}) / \|\boldsymbol{g}\|, \tag{2}$$

where M_H is the Hessian matrix of the volume image, and $\boldsymbol{g}$ is the gradient vector (the normal vector). After resolving a minimization problem, the principal curvatures and directions were expressed as functions of the first and second derivatives of the image. In [4], the authors started their derivation based on the first and second fundamental forms, and their solutions were presented as

$$k_{1,2} = H \pm \sqrt{\Delta} \; with \, \Delta = H^2 - K, \tag{3}$$

where $H = (k_1 + k_2)/2$, $K = k_1 k_2$ are the mean and Gaussian curvatures, which are

$$H = \frac{1}{2\|\boldsymbol{g}\|^3}\Big[I_x^2(I_{yy} + I_{zz}) - 2I_y I_z I_{yz} + I_y^2(I_{xx} + I_{zz}) - 2I_x I_z I_{xz} + I_z^2(I_{xx} + I_{yy}) - 2I_x I_y I_{xy} \Big], \tag{4}$$

$$K = \frac{1}{\|\boldsymbol{g}\|^4}\Big[I_x^2(I_{yy}I_{zz} - I_{yz}^2) + 2I_yI_z(I_{xz}I_{xy} - I_{xx}I_{yz}) + I_y^2(I_{xx}I_{zz} - I_{xz}^2) + 2I_xI_z(I_{yz}I_{xy} - I_{yy}I_{xz}) + I_z^2(I_{xx}I_{yy} - I_{xy}^2) + 2I_xI_y(I_{xz}I_{yz} - I_{zz}I_{xy})\Big] \quad . \tag{5}$$

In Equations (4) and (5), the notions of I with various subscripts indicate the various partial derivatives of image intensity I. Therefore, both methods in [3, 4] denoted the principal curvatures as functions of the first and second spatial derivatives of the volume images, which are often estimated through the first and second derivatives of Gaussian kernels.

2.2 Knutsson Mapping Method

In the aforementioned kernel methods, the curvature is essentially evaluated as $I_{TT}/\|\nabla I\|$, where $\boldsymbol{T}$ represents the associated principal direction, and I_{TT} indicates the second derivative of the image intensity along the principal direction. Therefore, severe overestimation occurs when the gradient magnitude $\|\nabla I\|$ vanishes. Rieger *et al*. [23] presented a Knutsson mapping-based method to solve the discontinuity problem.

The curvature k in direction $\boldsymbol{T}$ can also be defined as the magnitude of the change of the surface normal N:

$$k_{\boldsymbol{T}} = \|\nabla_{\boldsymbol{T}} N\|. \tag{6}$$

The normal N and the two principal directions T1 and T2 can be retrieved through the eigenvalue analysis of the gradient structure tensor $\overline{G} = \overline{\mathbf{v}\mathbf{v}^t}$ with $\mathbf{v} = \nabla I$. In the above definition, the gradient magnitude is excluded, and the discontinuity problem of the gradient magnitude is removed. However, the discontinuity issue of the orientation field ±N still remains. Direct computation of the partial derivative of the discontinuous orientation field will lead to spurious curvatures. The idea of the mapping method is to map the orientation field into a continuous representation with a mapping M, so that $\|\delta M(\mathbf{v})\| = \kappa\|\delta\mathbf{v}\|$ holds. The Knutsson mapping $M(\mathbf{v}) = \mathbf{v}\mathbf{v}^t/\|\mathbf{v}\| = \pi r^2$ is used with $\kappa = \sqrt{2}$ for $\|\mathbf{v}\| = cons.$ The norm of the mapped derivative is linearly related to the norm of the derivative of the original orientation v. The principal curvatures can then be calculated as

$$|k_{1,2}| = \frac{1}{\sqrt{2}}\left\|\nabla_{T_{1,2}} M(N)\right\|. \tag{7}$$

The sign of the curvature is the negative of the sign of $\boldsymbol{T}^t M_{\mathrm{H}} \boldsymbol{T}$, where M_{H} represents the Hessian matrix.

3 Results

For comparison, the above-mentioned two widely used kernel methods introduced by Monga *et al*. [3] and Thirion *et al*. [4], referred to as Monga's and Thirion's method, are implemented. The three methods are applied to a phantom (shown in Figure 1) and a patient colon. In Figure 1, the inner and outer radii of the spherical shell are 34 and 36. The initial image intensity on the shell is 100, and is then smoothed with Gaussian kernel at σ=2. The resulting curvatures of the points on the circle of radius 35 (k_1=k_2=1/35 ≈ 0.0294) were investigated among the three methods for evaluation.

Fig. 1. The cross section of the 3D spherical shell

For the phantom in Figure 1, the mean and variance of the resulting |k1| and |k2| at 360 sample points (the sampling angle is 1 degree) on the aforementioned circle are listed in Table 1. The results from the new method are almost equal to the theoretical values. However, the results from the other two methods have severe overestimation.

Table 1. The statistics of the $|k_1|$ and $|k_2|$ resulting from the three methods

	Monga's method		Thirion's method		New method	
	mean	variance	mean	Variance	mean	variance
$\|k_1\|$	69.94	3.62e+2	82.93	4.92e+2	**0.0293**	3.34e-8
$\|k_2\|$	54.21	5.12e+2	92.72	5.84e+2	**0.0293**	3.39e-8

Figure 2 shows part of an axial slice of a patient and the related 3D endoscopic display. The red point in the left image indicates a voxel on a thin fold, as shown in the right image in Figure 2. The point is classified as a voxel on the colon wall by our segmentation method. The curvatures ($|k_1|$, $|k_2|$) on it are estimated as (19.656, 2.323), (15.852, 1.494), (0.015, 0.014) by Monga's, Thirion's, and the new method, respectively. Based on visual inspection, the structure near the point is very flat, and the curvatures should be very small. Obviously, the results from the new method are reasonable, whereas those from the other two methods are severe overestimates.

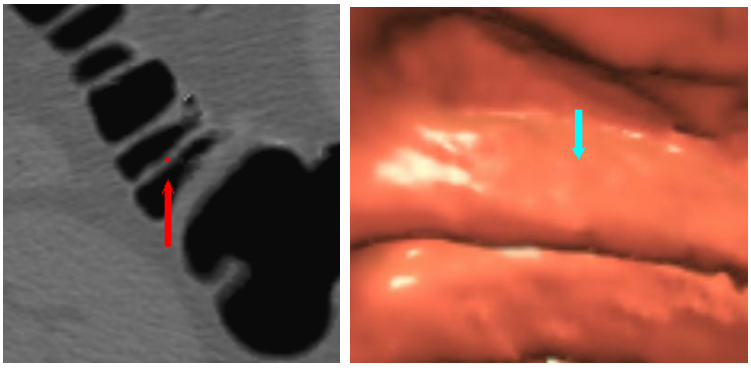

Fig. 2. Left -- part of one axial slice of a patient. Right -- the related 3D endoscopic view. The red point indicated by the red arrow in the left image corresponds to the location indicated by the arrow in the right image.

4 Conclusion

From the results on the phantom and patient data, the new method greatly improves the curvature estimation for the voxels on the thin shell objects. This method will benefit the shape analysis for some colonic objects, like haustral folds and even some long polyps. In our future work, we will investigate the possible benefits of the new method for shape analysis in computer-aided polyp detection in virtual colonoscopy.

References

1. American Cancer Society. Cancer Facts & Figures 2008. American Cancer Society, Atlanta (2008)
2. Summers, R., Yao, J., Pickhardt, P., Franaszek, M., Bitter, I., Brickman, D., Krishna, V., Choi, R.: Computed tomographic virtual colonoscopy computer-aided polyp detection in a screening population. Gastroenterology 129, 1832–1844 (2005)
3. Monga, O., Ayache, N., Sander, P.T.: From voxel to intrinsic surface features. Image and Vision Computing 10(6), 403–417 (1992)
4. Thirion, J.P., Gourdon, A.: Computing the differential characteristics of isointensity surfaces. Computer Vision and Image Understanding 61(2), 190–202 (1995)
5. Summers, R., Beaulieu, C., Pusanik, L., Malley, J., Jeffrey, R., Glazer, D., Napel, S.: Automated polyp detector for CT colonography: feasibility study. Radiology 216, 284–290 (2000)
6. Yoshida, H., Nappi, J.: Three-dimensional computer-aided diagnosis scheme for detection of colonic polyps. IEEE Transactions on Medical Imaging 20(12), 1261–1274 (2001)
7. Wang, Z., Liang, Z., Li, L., Li, X., Anderson, J., Harrington, D.: Reduction of false positives by internal features for polyp detection in CT-based virtual colonoscopy. Medical. Physics 32(12), 3602–3616 (2005)

8. Konukoglu, E., Acar, B., Paik, D., Beaulieu, C., Rosenberg, J., Napel, S.: Polyp enhancing level set evolution of colon wall: method and pilot study. IEEE Transactions on Medical Imaging 26(12), 1649–1656 (2007)
9. van Wijk, C., van Ravesteijn, V.F., Vos, F.M., van Vliet, L.J.: Detection and segmentation of colonic polyps on implicit isosurfaces by second principal curvature flow. IEEE Transactions on Medical Imaging 29(3), 688–698 (2010)
10. Wang, S., Zhu, H., Lu, H., Liang, Z.: Volume-based feature analysis of mucosa for automatic initial polyp detection in virtual colonoscopy. International Journal of Computer Assisted Radiology and Surgery 3(1-2), 131–142 (2008)
11. Zhu, H., Duan, C., Pickhardt, P., Wang, S., Liang, Z.: Computer-aided detection of colonic polyps with level set-based adaptive convolution in volumetric mucosa to advance CT colonography toward a screening modality. Cancer Management and Research 1(1), 1–13 (2009)
12. Zhu, H., Fan, Y., Lu, H., Liang, Z.: Improving initial polyp candidate extraction for CT colonography. Physics in Medicine and Biology 55, 2087–2102 (2010)
13. Zhu, H., Liang, Z., Pickhardt, P., Barish, M., You, J., Fan, Y., Lu, H., Posniak, E., Richards, R., Cohen, H.: Increasing computer-aided detection specificity by projection features for CT colonography. Medical. Physics 37(4), 1468–1481 (2010)
14. Campbell, S., Summers, R.: Analysis of kernel method for surface curvature estimation. International Congress Series 1268, 999–1003 (2004)
15. Rieger, B., Timmermans, F.J., Van Vliet, L.J., Verbeek, P.W.: On curvature estimation of ISO surfaces in 3D gray-value images and the computation of shape descriptors. IEEE Transactions on Pattern Analysis and Machine Intelligence 26(8), 1088–1094 (2004)
16. Lipschutz, M.: Differential Geometry. McGraw-Hill (1969)

Characterizing Colonic Detections in CT Colonography Using Curvature-Based Feature Descriptor and Bag-of-Words Model

Javed M. Aman, Ronald M. Summers, and Jianhua Yao

Radiology and Imaging Sciences Department, Clinical Center,
National Institutes of Health, Bethesda, MD, USA

Abstract. We present a method based on the content-based image retrieval (CBIR) paradigm to enhance the performance of computer aided detection (CAD) in computed tomographic colonography (CTC). The method explores curvature-based feature descriptors in conjunction with bag-of-words (BoW) models to characterize colonic detections. The diffusion distance is adopted to improve feature matching and clustering. Word selection is also applied to remove non-informative words. A representative database is constructed to categorize different types of detections. Query detections are compared with the database for classification. We evaluated the performance of the system by using digital phantoms of common structures in the colon as well as real CAD detections. The results demonstrated the potential of our technique for distinguishing common structures within the colon as well as for classifying true and false-positive CAD detections.

Keywords: CAD, CT colonography, affine invariant feature, bag-of-words.

1 Introduction

Cancer screening and early detection are an important step in colon cancer prevention. Optical colonoscopy (OC) is the traditional colon cancer screening procedure. However, because of its invasiveness, many patients forego this procedure. Computed tomographic colonography (CTC) has emerged as a minimally invasive screening procedure. CTC can benefit from CAD systems to improve the sensitivity and reduce the interpretation time [1]. Most CAD systems require post processing to reduce the number of false positives. We propose a method based on the Content-Based Image Retrieval (CBIR) paradigm to enhance the CAD performance.

CBIR is a computer vision technique for searching for similar images within an image database. It has been used in applications such as medical image searching [2] and artwork retrieval [3]. The images in a CBIR system are characterized as a set of feature descriptors computed directly from the images. Detecting affine transformation-invariant salient feature points in an image is important for the success of a CBIR system. The scale-invariant feature transform (SIFT) proposed by Lowe [6] is one of such feature descriptors. However, images vary greatly in the number of

H. Yoshida et al. (Eds.): Virtual Colonoscopy and Abdominal Imaging 2010, LNCS 6668, pp. 15–23, 2011.

feature points, which makes the comparison of two images difficult. The subsequent classification also requires a feature vector of fixed dimension. A vector quantization (VQ) technique was proposed to handle this problem. The bag-of-words (BoW) model [4] was one of the VQ techniques and was first introduced in natural language processing and then in computer vision and information retrieval, especially for object categorization. In the BoW model, feature points are grouped into clusters or "words" that represent the specific feature pattern shared by all feature points in the clusters. By mapping of its feature points into words, an image can be represented as a "bag of words" which can be employed in further classification.

In this paper, we propose a SIFT-like feature descriptor based on curvatures and incorporate it with the BoW model in a CBIR framework. Our method was validated with both phantom and clinical CTC data and demonstrated promising results.

2 Methods

Our system is a post-processing step for a CAD system on CTC. The CAD system segments the colon and generates a set of potential polyp detections based on local curvature and CT attenuation. Post-processing steps (such as support vector machines and CBIR) then further filter the detections to reduce the number of false positives. In our CBIR framework, the detections are cropped from the original CTC images by use of their segmentation boundaries. The cropped images are then re-sampled to uniform 64*64*64 blocks by use of B-Spline interpolation. Affine-invariant feature points are extracted from the image, and BoW models are generated. A database is constructed that stores representative detection images and their associated BoW models. A new detection is then compared against the database, and the retrieval results are employed to make a classification decision.

2.1 Curvature-Based Feature Descriptor

Feature points are salient points in the image that contain rich local image information. It is desirable that the feature descriptor is affine-invariant, so that similar images in different poses and scales present similar features. Features used in our method are derived from the n-dimensional scale-invariant feature transform (N-SIFT) method proposed by Cheung et al. [5], which was generalized from the 2D SIFT originally proposed by Lowe [6]. The method is comprised of two steps: feature point detection and feature descriptor generation.

In SIFT, feature points are related to the extrema points in the image's gradient space. A set of Gaussian smoothing filters (at different sigma scales) is applied to the image to generate a set of difference of Gaussian (DoG) images. Pixels that are extrema in their surrounding 3x3x3 neighborhoods in DoG are preliminary feature points. Duplicate points found in multiple DoG images are trimmed, leaving only the points with the greatest magnitude. The feature points are detected in a multi-scale image pyramid. The image in the successive scale is a linearly interpolated,

downsampled version of the Gaussian smoothed image in the previous scale. Feature points are detected in each scale independently, and their positions are then restored to the first scale. Figure 1b and 1d show feature points detected on a true-positive and false-positive image from CTC.

In the original SIFT implementation, the feature descriptor is constructed from a local image gradient that is weighted by the distance to the feature point. Cheung et al. [5] showed that gradient-based features can only cope with up to 10° rotation variation. In order to increase the robustness to the rotation, we propose a curvature-based feature descriptor. The shape index describes the local surface shape and is computed from the principal curvatures captured by a local Hessian matrix,

$$s = \frac{2}{\pi} \arctan \frac{\kappa_2 + \kappa_1}{\kappa_2 - \kappa_1} \tag{1}$$

Here κ_1 and κ_2 are the principal curvatures, and s is the shape index. The value ranges from 0.0 to 1.0, which corresponds to concavities and convexities such as ruts, troughs, caps, domes, and ridges [7]. The shape index is both scale- and rotation-invariant. A histogram of the shape index in a 9x9x9 neighborhood of the feature point is used as the feature descriptor. The histogram is binned from 0.0 to 1.0 at 0.05 intervals, for 20 bins.

The similarity between two feature descriptors can be evaluated by their distance. The most straightforward is the Euclidean distance, where a bin-to-bin distance is summed up. However, the Euclidean distance does not take into account the relationship between neighboring bins and may suffer from a rounding effect when assigning the histogram. To handle this situation, we apply a diffusion distance metric for comparison of our feature descriptors [8]. The diffusion distance is a cross-bin comparator of histograms. It models the difference between two histograms as a temperature field and considers the diffusion process on the field. A Gaussian pyramid scheme is implemented to discretize the continuous diffusion process and the sum of the norm over all of the pyramid layers. The diffusion distance is computed as follows. First, the difference between the two histograms is set as the first layer of the pyramid. The next layer is the downsampled (by two) histogram of the previous layer convolved with a Gaussian filter (σ=0.5). This process is repeated until there is only one bin in the histogram. The sum of the differences in all layers is the diffusion distance.

$$\begin{aligned} K(h_1, h_2) &= \sum_{i=0}^{n} |d_i| \\ d_0 &= h_1 - h_2, \quad d_i(x) = d_{i-1}(x)_{\downarrow 2} * \varphi(x, 0.5) \end{aligned} \tag{2}$$

Here K is the diffusion distance, h_1 and h_2 are two feature descriptors, d_0 is the difference of the histograms at the first layer, d_i is the downsampled version of d_{i-1} and φ is a Gaussian function.

2.2 Bag-of-Words (BoW) Model

After the feature points are extracted, the detection image can be characterized by a set of feature descriptors. We then employ the vector quantization (VQ) technique [4] to generate a codebook from the feature descriptors. The descriptors are clustered by use of the K-means clustering algorithm [9], and the center of each cluster is a codeword. The codeword is indexed, and the histogram of the codeword appearances in an image is used as the Bag-of-Words model and applied in the subsequent image classification.

K-means clustering has two primary pitfalls: sensitivity to initial cluster centers and high computational complexity. To overcome these, a kd-tree data structure is introduced. The kd-tree organizes the feature space orthogonally and hierarchically. It is a binary tree dividing a high-dimensional space and is constructed as follows: starting from the root, for every non-leaf node, a splitting hyperplane at the median point of the longest axis of the node divides the space into two subspaces (nodes). The splitting process is iterated until there is only one point in each node (leaf). Initial cluster centers are taken from points in nodes at the same level of the tree to ensure they are well separated. Although this does not technically solve the sensitivity to the initialization problem, it does allow better clustering as opposed to randomly selecting the seed points. The spatial separation of points also improves the performance of the K-means clustering by allowing it to ignore interactions between distant points. A filtering algorithm [9] of K-means clustering is applied to the kd-tree to obtain the cluster centers (i.e. codewords). During each iteration, the feature points are associated with their closest cluster centers, and the cluster centers are updated by their associated feature points. The process is repeated until the cluster center is stabilized. The kd-tree reduces the complexity from $O(n^2)$ to O(nlogn).

The BoW is a histogram recording the count of codeword occurrences in a particular image. Each feature point is associated with a codeword in the codebook. The association is computed as,

$$association(k,c,r) = \frac{\|c-k\|}{r \bullet |c-k|} \tag{3}$$

Here, k is a feature point, c is the codeword, and r is the radius of a codeword which describes the radius of the cluster represented by the codeword. A feature point is assigned the codeword with maximum association value, and one count of the codeword occurrence will be added to the BoW histogram. The histograms are normalized to account for the differences in the number of feature points among images. Figure 1c and 1f show the BoW histograms of the two detections in Figure 1a and 1d.

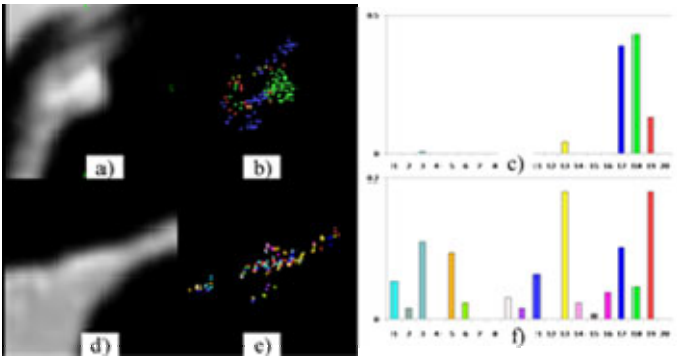

Fig. 1. Feature points and Bag-of-Words models. a) a true positive detection; b) feature points of a); c) BoW model of a); d) a false positive detection; e) features points of d); f) BoW model of d). The color code in the histogram corresponding to that for the feature points.

Not all of the codewords are useful in the object recognition. Noisy words may exaggerate the difference between similar BoW histograms. Non-informative words, such as words common across images, may skew the comparison. We apply a forward stepwise word selection scheme to choose the informative words for classification. For any word in the codebook, if removing it improves the performance, it will be dropped from the codebook, otherwise it is kept.

2.3 Content-Based Image Retrieval (CBIR)

Our system is built in a CBIR framework. We construct a database of representative detections and use it to assist classification. The database stores the detection images and their BoW histogram, and it contains equal numbers of detections in each category (TP and FP in our case). Because we have far more FP detections than TP detections in our training data, all TPs are put in the database, and FPs are randomly selected to match the number of TPs. Another strategy is to conduct a K-means clustering on the FP detections, and the centers of the clusters are used as representative detections.

Given a new detection, its BoW histogram is computed and queried against those in the database. The results are ranked by their similarities to the query, and only the top matches are retrieved. The number of the retrieval results is known as the search depth. Based on the labels (TP or FP) of the retrieval results, the attribute of the query image can be determined. Two metrics can be computed from the retrieval results. One is the TP ratio (TPr), i.e., the number of TP detections in the retrieval set divided by the search depth. The other is the normalized discounted cumulative gain (nDCG), which is a common measure of information retrieval effectiveness [10].

$$nDCG_p = \frac{\sum_{i=1}^{p} \frac{(2^{rel_i} - 1)}{\log_2(1+i)}}{\sum_{i=1}^{p} \frac{1}{\log_2(1+i)}} \tag{4}$$

Here, rel_i is the relevance variable (either 1 for a match or 0 for a non-match), p is the search depth. nDCG equals to 1 if all of the matches in the result set are relevant.

3 Experiments and Results

3.1 Phantom Experiments

Four types of realistic phantoms of common colon structures were generated: folds, walls, dents, and polyps. These were created by use of Boolean shape operators on simple shapes such as prisms, ellipsoids, and cylinders. Colon walls are modeled as the surface of cylinders with different radius. Dents are models as ellipsoids cut into the colon wall. Polyps are modeled as ellipsoids protruding from the colon wall. Folds are also modeled as thin and elongated ellipsoids. For further complication, intensity and structural noise are added to the phantoms. Intensity noise is Gaussian noise added to the pixel intensity. Structural noise is intended to add bumps and dents (in the form of 3*3*3 balls) to the colon surface.

Ten phantoms of varying size and shape of each of the four types were generated. Two noise levels, 10% intensity and 5% structural, and 20% intensity and 10% structural, were added to the phantoms. There were a total of 120 phantoms (40 clean and 40 noisy at two noise levels, respectively). Figure 2 shows examples of noisy phantom and their BoW models.

We randomly selected half of the phantoms (60) to train the codebook of 20 codewords and build the database. We then evaluated the performance by using the remaining phantoms. The retrieval depth was 15. We compared the nDCG of the system by using Euclidean distance (ed) vs. diffusion distance (dd), and no word selection (nws) vs. word selection (ws) (see Table 1).

Our method shows a strong ability to distinguish different structures in the colon. The word selection showed mixed results, marginally improving or weakening the matching of different structures. Codebooks generated by use of the diffusion distance metric show a better retrieval performance for the fold type, but a decreased performance for the wall type. The polyp phantoms showed perfect matching, because they exhibited high convex curvature feature points which were uncommon in the other structures.

3.2 CTC Experiments

We tested our method on 162 CTC studies. The CAD system based on a support vector machine resulted in 1274 detections. Of them, 94 were defined to be TPs based

on OC findings, whereas 1180 were FPs. There were 11 polyps less than 6mm, 51 between 6 and 9mm, and 32 larger than 9mm. We conducted a ten-fold cross-validation. In each run, we used nine tenths of the data to construct the representative database, and the remaining one tenth was used for testing. The number of codewords was 20. Figure 3 shows the retrieval results of the detections shown in Figure 1. Table 2 lists the mean performance of the 10-fold cross-validation. Figure 4 shows the FROC curves generated by the ROCKIT toolkit [11]. The CBIR was able to eliminate 40% of the FPs (4.3 FP per case) while maintaining the sensitivity at 91%.

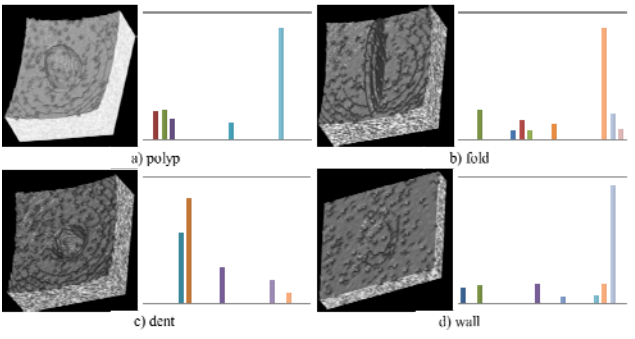

Fig. 2. Noisy phantom examples (left) and their BoW models (right)

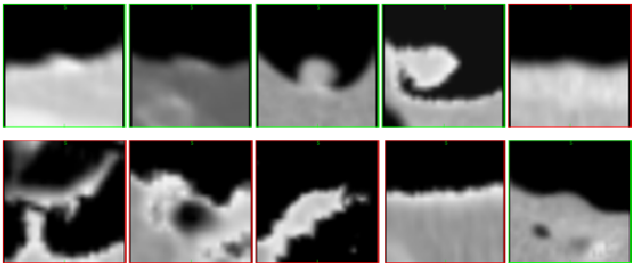

Fig. 3. Retrieval results from CBIR. First row: results of the TP detection in Figure 1a); Second row: results of the FP detection in Figure 1d). Images with green frames are TP detections, and those with red frames are FP detections.

Table 1. Summary of performance in phantom data (nDCG)

nDCG	ed-nws	ed-ws	dd-nws	dd-ws
Polyp	1.00	1.00	1.00	1.00
Fold	0.75	0.75	0.88	0.88
Dent	0.82	0.82	0.82	0.82
Wall	0.77	0.70	0.68	0.68
All	0.82	0.82	0.84	0.85

Table 2. Summary of performance in CTC data

Type	TPr	nDCG
TP	0.68 +/- 0.24	0.68 +/- 0.25
FP	0.35 +/- 0.27	0.62 +/- 0.28

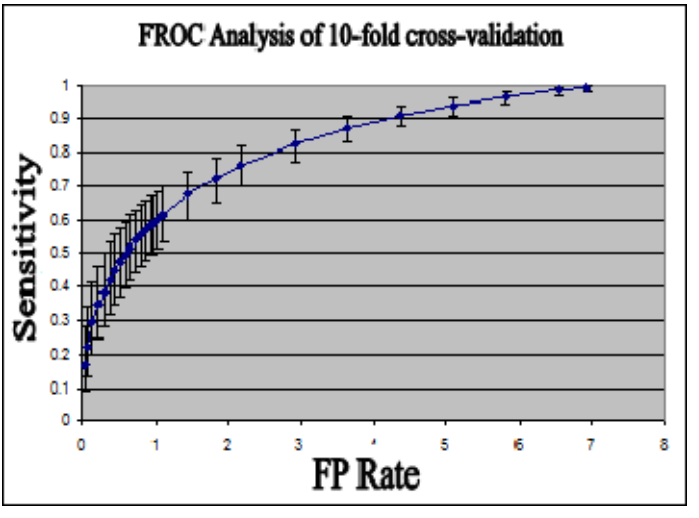

Fig. 4. FROC analysis of CTC data

4 Discussion and Conclusion

We proposed an approach to characterizing the colonic detection in CTC by using a curvature-based feature descriptor and Bag-of-Words models. The curvature-based feature descriptor provides an affine-invariant description of salient points in an image and the BoW model provides a standard platform for comparing detections. We also employed the CBIR paradigm to determine the detection attribute by using a database of pre-selected representative examples. The method was validated on both synthetic phantoms and clinical CTC data.

There is room for improvement in both the feature descriptor and the BoW model. The spatial location of the feature point can be encoded in the descriptor to assist the object recognition and image classification. Techniques developed in information retrieval such as stop word removal and various word-weighting schemes can be adopted in the BoW model. Different strategies such as document frequency, χ^2 statistics, and mutual information can also be explored in the word selection process. The CBIR technique adopted in our system is similar to the k-Nearest Neighbor (kNN) classifier. Other advanced classification techniques such as a neural network, support vector machine, and Bayes model can be applied.

References

1. Summers, R.M., et al.: Computed Tomographic Virtual Colonoscopy Computer-Aided Polyp Detection in a Screening Population. Gastroenterology 129, 1832–1844 (2005)
2. Muller, H., et al.: Review of content-based image retrieval systems in medical applications—clinical benefits and future directions. International Journal of Medical Informatics 72, 1–23 (2004)
3. Guicca, G., Schettini, R.: A relevance feedback mechanism for content-based image retrieval. Info. Proc. and Manag. 35, 605–632 (1999)
4. Yang, J., et al.: Evaluating bag-of-visual-words representations in scene classification. In: International Workshop on Multimedia Information Retrieval. ACM, Augsburg (2007)
5. Cheung, W., Hamarneh, G.: n-SIFT: n-Dimensional Scale Invariant Feature Transform. IEEE Transactions on Image Processing 18(9), 2012–2021 (2009)
6. Lowe, D.G.: Distinctive image features from scale-invariant keypoints. International Journal of Computer Vision 60, 91–110 (2004)
7. Koenderink, J.J., van Doorn, A.J.: Surface shape and curvature scales. Image and Vision Computing 10(8), 557–565 (1992)
8. Ling, H., Okada, K.: Diffusion Distance for Histogram Comparison. In: IEEE Conference on Computer Vision and Pattern Recognition, New York, USA (2006)
9. Kanungo, T., et al.: An Efficient k-Means Clustering Algorithm: Analysis and Implementation. IEEE Transactions on Pattern Analysis and Machine Intelligence 24(7), 881–892 (2003)
10. Croft, B., Metzler, D., Strohman, T.: Search Engines: Information Retrieval in Practice. Addison Wesley (2009)
11. ROCKIT, Kurt Rossman Laboratories. University of Chicago, Chicago, IL (2004)

Haustral Fold Segmentation of CT Colonography Using Ridge Line Detection

Hongbin Zhu[1], Lihong Li[2], Yi Fan[1], and Zhengrong Liang[1]

[1] Department of Radiology, State University of New York, Stony Brook, NY 11794, USA
{hbzhu,yifan,jzliang}@mil.sunysb.edu
[2] Dept. of Engineering Science & Physics, City Univ. of New York at College of Staten Island, Staten Island, NY 10314, USA
lihong.li@csi.cuny.edu

Abstract. In computed tomographic colonography, colonic/haustral folds often serve as important anatomic landmarks for various tasks, such as virtual endoscopic navigation, tenia coli extraction, prone/supine registration, and polyp matching. In this paper, we present an automatic fold segmentation method based on the negative ridge line detection method. Because haustral folds meet the normal colon wall at negative ridge lines, automatic fold segmentation can be achieved by taking the negative ridge lines as fold boundaries. Preliminary results on patient data are very promising.

Keywords: haustral fold detection, CT colonography, differential properties, ridge line, and triangle mesh.

1 Purpose

This study aims to segment haustral folds automatically and to provide an anatomic reference, which will benefit virtual endoscopic navigation, tenia coli extraction, supine/prone registration, and polyp matching.

2 Methods

In this approach, the whole pipeline can be outlined in three stages: colon surface extraction, crest line detection, and fold segmentation, as shown in Figure 1.

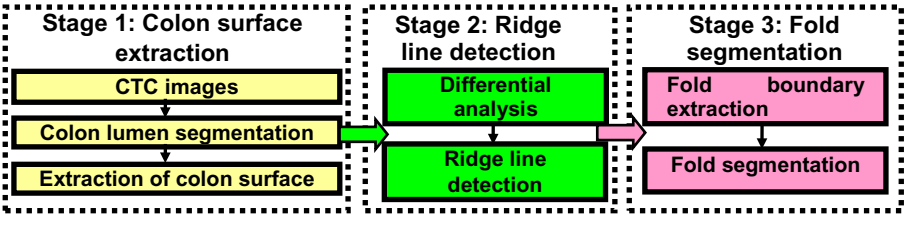

Fig. 1. Pipeline of the presented fold segmentation method

H. Yoshida et al. (Eds.): Virtual Colonoscopy and Abdominal Imaging 2010, LNCS 6668, pp. 24–31, 2011.

2.1 Colon Surface Extraction

CTC images (Figure 2(a)) are processed by a soft image segmentation method [1, 2] with the outputs of the cleansed CTC image (Figure 2(b)) and the colon lumen image (the image without the green curve in (Figure 2(c))). The level-set method [3] is then applied to the colon lumen image to retrieve a one-voxel-layer (the green curve in Figure 2(c), as the starting layer in [3]) representing the colon wall. Following that, the marching cube method [4] is used to construct the triangle mesh representation of the colon surface (Figure 2(d)).

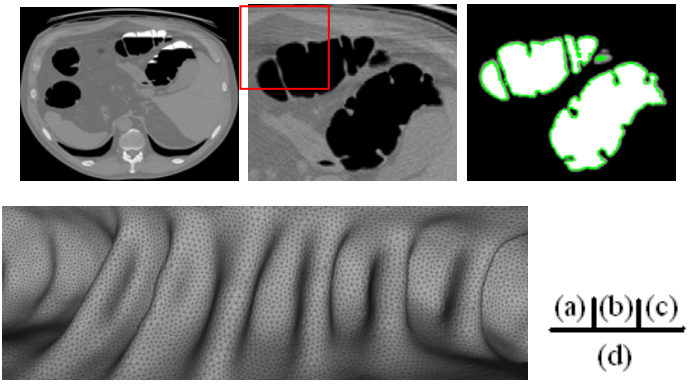

Fig. 2. The process of colon surface extraction. (a) An original CTC image; (b) cleansed CTC image; (c) segmented colon lumen image, where the green curve indicates the one-voxel-layer of the colon wall; (d) the constructed triangle mesh of the colon surface. Note: (b) and (c) are zoomed images of the part in the red rectangle in (a).

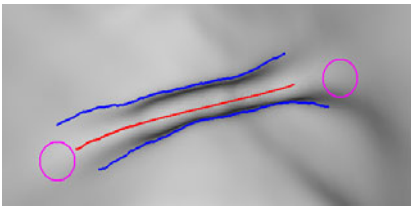

Fig. 3. A typical haustral fold in a patient colon. The red curve indicates the positive ridge at the top of the fold, and the blue curves represent the negative ridges where the fold meets the flat colon wall. Areas near the two circles indicate the two ends of the fold, where there is no ridge defined.

2.2 Ridge Line Detection

Typical haustral folds are thin and elongated structures. As shown in Figure 3, the fold protrudes from the flat colon wall into the colon lumen. Generally, the surface bends concavely where the fold meets the flat colon wall, and it bends convexly at the

top of the fold. The curves on a surface along which the surface bends most sharply are referred to as ridges [5, 6], i.e., the loci of points where the absolute values of the principal curvature are local maximums along the associated curvature directions. The positive maximum and negative minimum indicate the convex and concave bends, respectively, as shown with the red and blue curves in Figure 3. Straightforwardly, the concave bends, i.e., the negative ridges, can serve as the boundary to segment the haustral fold. However, at the two ends of the fold (as circled in Figure 3), the fold might merge into the flat wall smoothly, and there is no ridge point at these locations. The negative ridge breaks here, as shown by the two disconnected negative ridges in Figure 3. In this study, we first detected the negative ridges. Then, we generated closed fold boundaries for the purpose of fold segmentation.

2.2.1 Differential Analysis

Umbilic points have identical curvatures in all directions in their tangent plane, and the bend (including bending degree and direction) in their neighborhood is locally symmetric (e.g., the points in planar/circular area). Therefore, no principal directions can be well defined at umbilic points. Fortunately, ridge points have noticeably different bend in different directions, and umbilic points will not appear on ridges. As mentioned above, negative ridge points have minimum principal curvatures along the curvature line. Therefore, third- and forth-order differential properties (first- and second-order derivatives of curvatures) on the mesh have to be estimated. Theoretically, in a neighborhood of a point, the surface can be locally parameterized as a height function. In the Monge coordinate system, where the z-axis is aligned with the normal, and x, y-axis are aligned with the principal directions, the surface can be represented by the following canonical height function form:

$$\begin{aligned} z(x,y) = &\frac{1}{2}(k_1 x^2 + k_2 y^2) + \frac{1}{6}(b_0 x^3 + 3b_1 x^2 y + 3b_2 x y^2 + b_3 y^3) \\ &+ \frac{1}{24}(c_0 x^4 + 4c_1 x^3 y + 6c_2 x^2 y^2 + 4c_3 x y^3 + c_4 y^4) + O(\|x,y\|^5) \end{aligned} \tag{1}$$

where the coefficients k_1, k_2 are the two principal curvatures, and b_0, …, b_3, c_0, …, c_4 are coefficients of higher order terms. If we assume that $k_1 > k_2$, i.e., the first and second principal curvature, x, y-axis are then associated with the first and second principal directions. The Taylor expansion of k_1 and k_2 along the first and second principal directions at the origin are

$$k_1(x) = k_1 + b_0 x + \frac{P_1}{2(k_1 - k_2)} x^2 + O(x^3) \tag{2}$$

$$k_2(y) = k_2 + b_3 y + \frac{P_2}{2(k_2 - k_1)} y^2 + O(y^3) \tag{3}$$

where $P_1 = 3b_1^2 + (k_1 - k_2)(c_0 - 3k_1^3)$, $P_2 = 3b_2^2 + (k_2 - k_1)(c_4 - 3k_2^3)$. In order to estimate the coefficients that indicate the high-order differential properties in Equation (1), the 4-jet fitting method in [7] is employed.

2.2.2 Ridge Line Detection

Points on ridge lines have extreme principal curvatures along the associated curvature directions. Therefore, a point is a

- positive ridge point if $b_0 = 0$ and $P_1 < 0$ and $k_1 > |k_2|$;
- negative ridge point if $b_3 = 0$ and $P_2 > 0$ and $k_2 < -|k_1|$.

Linear interpolation is used to approximate those differential properties of the points on the surface beyond those mesh vertices. If two ridge points are detected on the edges of a triangle, they are connected by a straight line segment. If all three edges of a triangle have ridge points, the points are connected with the centroid of the triangle. In this study, because we focus on seeking for fold boundaries, the ridge lines of interest are the negative ones. In the following text, the term "ridge line" refers to a negative ridge line for simplicity.

Because high-order differential properties are very sensitive to small bends and noise, a large amount of ridge lines is yielded, as shown in Figure 4(a). Therefore, the most prominent ridges should be selected. Because ridge line characterizes with sharp bend, i.e., a large absolute curvature value, the integral of the curvature along the ridge line may serve as the *strength* of the ridge line [6]. Furthermore, for more prominent ridges, the curvature varies more along its curvature line. Therefore, the integral of the second-order derivative of the curvature (which can be estimated with Equation (3)) may serve as the *sharpness* of the ridges [8]. By thresholding of these two features of the ridges, meaningless ridges are filtered out and prominent ridges remain, as shown in Figure 4(b).

2.3 Fold Segmentation

2.3.1 Fold Boundary Extraction

So far, the remaining ridges are morphologically prominent. However, the "flat" colon wall, even including the fold surface, is not smooth. Extra ridges, such as the ridges beyond the fold boundaries in Figure 4(b), do not indicate the fold boundaries and could survive from the above two filters. Therefore, an anatomic analysis should be conducted to design extra filters to remove such redundant ridges.

The human colon is generally a tubular object. Three axes, i.e., the longitudinal, radial, and circumferential ones, can serve as the references for describing locations in the colon. Based on these references, the haustral folds have several anatomic characteristics, as follows:

- They are thin structures and have a small longitudinal extent.
- They are flat structures, and their boundaries are usually smooth.
- They are elongated in the circumferential direction of the human colon, and standing on the colon wall in the radial direction.

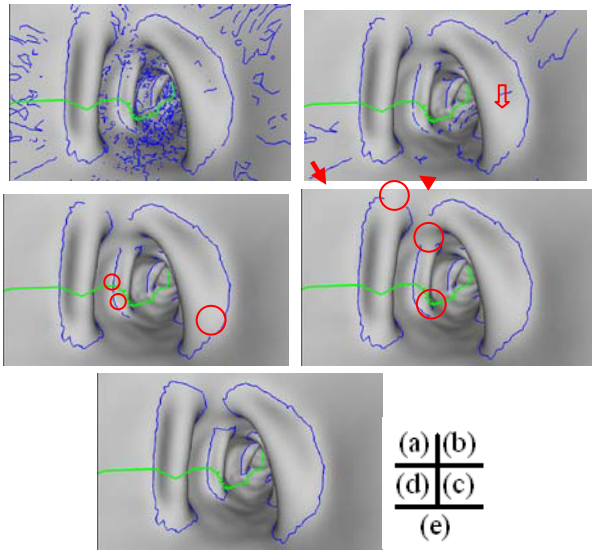

Fig. 4. The process of fold boundary extraction. The green thick curve represents the centerline. (a) The original unfiltered ridges. (b) The remaining prominent ridges filtered with the strength and sharpness. (c) The surviving ridges indicating fold boundaries after thresholding of the three anatomically relevant features. (d) Ridges after removal of the small disconnections. (e) Closed fold boundaries by connecting the associated ridges at the fold ends.

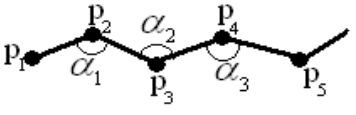

Fig. 5. Illustration of a typical ridge. p_i is ridge point (on edges of the triangle mesh), and p_ip_{i+1} is ridge segment, where $i = 1, 2, \cdots$. α_i is the angle between two neighboring ridge segments.

Based on the above knowledge, several anatomically relevant features are designed for each ridge in order to select those ridges indicating true fold boundaries. We also extract the center line of the colon [9] to help design these features:

- *Zigzagness*: $Z_r = (mean\{\alpha_i\} - \pi)^2 + \mathrm{var}\{\alpha_i\}$, where $\mathrm{mean}\{\alpha_i\}$ and $\mathrm{var}\{\alpha_i\}$ are the mean and variance of the angles shown in Figure 5. Therefore, a larger Z_r means that the ridge is more zigzag, like the ridge indicated by the arrowhead in Figure 4(b).
- *Centerline alignment*: $CA_r = L_r^c / L_r$, where L_r denotes the length of the ridge. For each ridge point p_i, it associates with a point, c_i, on the centerline, indicating the minimum distance from the ridge point to the centerline. Thus, L_r^c represents the maximum length along the centerline between any pair of c_i. Therefore, if a

ridge aligns with the centerline (i.e., extends along the longitudinal direction), a large CA_r (approaching to 1) can be expected (e.g., the ridge flagged with the solid arrow in Figure 4(b)), whereas for ridges perpendicular to the centerline, the CA_r will be small (approaching 0).

- *Radialness*: $R_r = (\max\{f_i\} - \min\{f_i\})/L_r$, where f_i is the distance from ridge point p_i to its associated centerline point c_i. Therefore, R_r will be large for ridges extending in the radial direction (e.g., the ridge pointed to by the hollow arrow in Figure 4(b)), whereas values are small for those extending in the circumferential direction.

By thresholding of the above three features, ridges indicating the boundaries of haustral folds remain, as shown in Figure 4(c).

So far, the surviving ridges are ready to serve as seeds for fold boundaries. However, as mentioned above, the differential property-based ridge detector is sensitive to small bends of the surface, and the seeding ridges appear disconnected even beyond the fold ends, as indicated by the circled disconnections in Figure 4(c). Fortunately, such disconnections are usually small. We can connect any two ridges if their distance is smaller than a thresholding value L_c. The connected seeding ridges are shown in Figure 4(d).

To form a closed fold boundary, these ridges still need to be connected at the ends of the fold, as circled in Figure 4(d). As can be seen, the seeding ridges might be connected at both (closed already), one, or none of the two ends of the fold. Therefore, we close the seeding ridges with the following steps:

1. For all closed seeding ridges, we do not do anything;
2. For all seeding ridges disconnecting just at one end of the fold, we connect them at another end of the fold;
3. For the remained seeding ridges disconnecting at both ends of the fold, we first need to pair the two ridges belonging to one fold. Two seeding ridges can be paired together if they are close and approximately parallel, and if there is at least one prominent positive ridge (representing the fold top) in between. Finally, the paired seeding ridges are connected at the two ends of the fold.

Figure 4(e) shows the closed ridge lines representing the fold boundaries. It should be noted that all of the ridge connections mentioned above are implemented by finding the geodesic path [10] on the triangle mesh.

2.3.2 Fold Segmentation

Once we have a closed boundary, the mesh is split into two subsets of triangles. The body of the fold can be easily retrieved by selecting the smaller triangle subset. The resulting fold segmentations are shown in Figure 6.

3 Results

We tested the whole algorithm on one patient data set with 191 haustral folds. During the process of fold boundary extraction, the applied thresholds are as listed in Table 1, and Figure 4 shows the process with endoscopic views. By cutting open parts of the patient colon, the final resulting fold segmentation is shown in Figure 6, where the segmented folds are highlighted in blue.

Table 1. Thresholds for extracting fold boundaries

Strength	Sharpness	Zigzagness	Centerline alignment	Radialness
.8	80,000	0.5	0.2	0.3

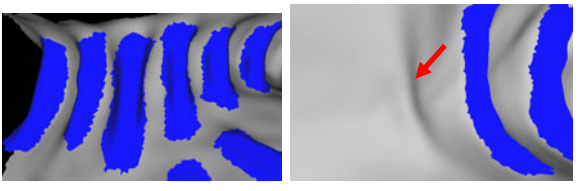

Fig. 6. Final results on parts of the experimental patient colon. The segmented folds are shown in blue. Left: The segmented haustral folds in one part. Right: The segmented haustral folds in another part. The fold pointed to by the arrow is too small and was missed by our algorithm.

With the above parameters, 161 segmentations were yielded. On inspection of the whole colon, they were all true haustral folds (i.e., 84.3% detection sensitivity), whereas 30 others were missed. These missed folds were mostly small ones with small height, and they bent very little from the flat colon wall to grow protrusions. Therefore, the generated negative ridge lines often appeared to be "weak", and to have small strength and sharpness values. As a result, these ridge lines would be removed by the strength and sharpness filters. Further investigation should be conducted if these small folds were significant for a particular application.

4 Conclusion

In this study, we proposed a haustral fold segmentation algorithm by using ridge line detection for CT colonography. We applied the algorithm to a patient case, in which 84.3% of all the haustral folds were successfully segmented. The resulting haustral folds had clear boundaries, which will subsequently benefit further processing like tenia coli extraction.

In our future work, the algorithm will be tested with a large number of patient datasets. We also noticed that the current performance measurement did not merit the term "segmentation", while it was only for "detection". More accurate evaluation measures will be explored in an assessment of the performance of the algorithm, e.g., by comparison with the manual segmentation by physicians.

References

1. Liang, Z., Wang, S.: An EM approach to MAP solution of segmenting tissue mixtures: a numerical analysis. IEEE Transactions on Medical Imaging 28(2), 297–310 (2009)
2. Wang, S., Li, L., Cohen, H., Mankes, S., Chen, J., Liang, Z.: An EM approach to MAP solution of segmenting tissue mixture percentages with application to CT-based virtual colonoscopy. Medical. Physics 35(12), 5787–5798 (2008)
3. Zhu, H., Duan, C., Pickhardt, P., Wang, S., Liang, Z.: Computer-aided detection of colonic polyps with level set-based adaptive convolution in volumetric mucosa to advance CT colonography toward a screening modality. Cancer Management and Research 1(1), 1–13 (2009)
4. Lorensen, W.E., Cline, H.E.: Marching cubes: A high resolution 3D surface construction algorithm. Computer Graphics 21(4), 163–169 (1987)
5. Monga, O., Benayoun, S., Faugeras, O.: From partial derivatives of 3D density images to ridge lines. In: Proc. CVPR 1992, pp. 354–359. IEEE (1992)
6. Ohtake, Y., Belyaev, A., Seidel, H.: Ridge-valey lines on meshes via implicit surface fitting. ACM Transaction on Graphics (TOG) 23(3), 609–612 (2004)
7. Cazals, F., Pouget, M.: Estimating differential quantities using polynomial fitting of osculating jets. Computer Aided Geometric Design 22, 121–124 (2005)
8. Cazals, F., Pouget, M.: Topoly driven algorithms for ridge extraction on meshes, Technical Report RR-5526, INRIA (2005)
9. Wan, M., Liang, Z., Ke, Q., Hong, L., Bitter, I., Kaufman, A.: Automatic centerline extraction for virtual colonoscopy. IEEE Transactions on Medical Imaging 21(12), 1450–1460 (2002)
10. Mitchell, J.S.B., Mount, D.M., Papadimitriou, C.H.: The discrete geodesic problem. SIAM Journal on Computing 16(4), 647–668 (1987)

Recent Advances in Reduction of False Positives in Computerized Detection of Polyps in CT Colonography

Kenji Suzuki

Department of Radiology, The University of Chicago,
5841 South Maryland Avenue, Chicago, IL 60637
suzuki@uchicago.edu

Abstract. One of the major challenges in computer-aided detection (CADe) of polyps in CT colonography (CTC) is the reduction of false-positive detections (FPs) without a concomitant reduction in sensitivity. Major sources of FPs generated by CADe schemes include haustral folds, residual stool, rectal tubes, the ileocecal valve, and extra-colonic structures such as the small bowel and stomach. A large number of FPs is likely to confound the radiologist's task of image interpretation, lower the radiologist's efficiency, and cause radiologists to lose their confidence in CADe as a useful tool. Therefore, it is important to reduce the number of FPs as much as possible while maintaining a high sensitivity. In this paper, FP reduction techniques used in CADe schemes for detection of polyps in CTC are reviewed.

Keywords: classifier, pixel-based machine learning, computer-aided diagnosis, artificial neural network, support vector machine, colorectal cancer.

1 Introduction

Colorectal cancer is the second leading cause of cancer deaths in the United States [1]. Evidence suggests that early detection and removal of polyps (i.e., precursors of colorectal cancer) can reduce the incidence of colorectal cancer [2, 3]. CT colonography (CTC), also known as virtual colonoscopy, is a technique for detecting colorectal neoplasms by use of CT scans of the colon [4]. The diagnostic performance of CTC in detecting polyps, however, remains uncertain due to a propensity for perceptual errors [5]. Computer-aided detection (CADe) of polyps has been investigated to address that issue with CTC [6, 7]. CADe has the potential to improve radiologists' diagnostic performance in the detection of polyps [6, 7].

Several investigators have developed automated or semi-automated CADe schemes for the detection of polyps in CTC [8-14]. Although current CADe schemes could be useful for the detection of polyps, some limitations remain. One of the major limitations with current CADe schemes is a relatively large number of false-positive detections (FPs), which could adversely affect the clinical application of CADe for colorectal cancer screening. A large number of FPs is likely to confound the radiologist's task of image interpretation and thus lower radiologist efficiency. In addition, radiologists may lose their confidence in CADe as a useful tool. Therefore,

H. Yoshida et al. (Eds.): Virtual Colonoscopy and Abdominal Imaging 2010, LNCS 6668, pp. 32–39, 2011.

it is important to reduce the number of FPs as much as possible while maintaining a high sensitivity. In this paper, FP reduction techniques used in CADe schemes for detection of polyps in CTC are reviewed.

2 Classes of FP Reduction Techniques

Major sources of FPs generated by CADe schemes include haustral folds, residual stool, rectal tubes, the ileocecal valve, and extra-colonic structures such as the small bowel and stomach [7]. Various techniques have been developed for the reduction of FPs in CADe schemes for detection of polyps in CTC. There are three classes of FP reduction techniques developed for CADe schemes: feature-based classifiers, pixel-based machine learning (PML), and non-machine-learning-based methods. The three classes of FP reduction techniques described in the literature are reviewed briefly below.

2.1 Feature-Based Classifiers

A general idea of feature-based classifiers is using features of polyp candidates as the input information to a classifier. First, polyp candidates are segmented by use of a segmentation method. Next, features are extracted from the segmented polyps. Then, extracted features are entered as input to a classifier such as linear discriminant analysis (LDA) [15], quadratic discriminant analysis [15], a multilayer perceptron (one of the most popular is the artificial neural network (ANN) model) [16], and a support-vector machine (SVM) [17]. The classifier is trained with sets of input features and correct class labels. A class label of 1 is assigned to the output unit when a training sample is a polyp, and 0 is assigned to the output unit when it is a non-polyp.

Many investigators employed feature-based classifiers as FP reduction techniques. Näppi et al. developed a method for FP reduction based on volumetric features [18]. Gokturk et al. [19] developed an FP reduction method based on an SVM with histograms used as shape signature. Acar et al. [20] used edge-displacement fields to model the changes in consecutive cross-sectional views of CTC data and quadratic discriminant analysis for FP reduction. Jerebko et al. [21] used a multilayer perceptron to classify polyp candidates in their CADe scheme and improved the performance by incorporating a committee of multilayer perceptrons [22] and a committee of SVMs [23]. Wang et al. [24] developed an FP reduction method based on LDA with internal features (geometric, morphologic, and textural) of polyps. Li et al. [25] developed an FP reduction method based on an SVM classifier with wavelet-based features. Wang et al. [26] improved SVM performance by using nonlinear dimensionality reduction (i.e., diffusion map and locally linear embedding). Yao at al. [27] employed a topographic height map for calculating features for an SVM classifier for FP reduction. Hongbin et al. [28] developed projection features for an SVM classifier for FP reduction.

2.2 Pixel-Based Machine Learning (PML)

Recently, as available computational power increased dramatically, pixel/voxel-based machine learning (PML) emerged in medical image processing/analysis which use pixel/voxel values in images directly instead of features calculated from segmented regions as input information; thus, feature calculation or segmentation is not required. Because the PML can avoid errors caused by inaccurate feature calculation and segmentation, the performance of the PML can potentially be higher than that of common feature-based classifiers.

In the field of image processing, ANN-based supervised nonlinear image-processing techniques, known as "neural filters" [29], and "neural edge enhancers" [30], have been investigated for the reduction of quantum noise in coronary angiograms [31] and upper gastric radiographs [29] and for the supervised detection of left ventricular contours traced by cardiologists in ventriculograms [32]. By extending the neural filter and the neural edge enhancer, two-dimensional (2D) massive-training artificial neural networks (MTANNs) [33], which are a class of a PML based on an ANN regression model, have been developed to accommodate the task of distinguishing a specific opacity from other opacities in medical images. The MTANN learns the relationship between input images and corresponding “teaching” images (i.e., ideal or desired images) to distinguish lesions from non-lesions (i.e., FPs). The MTANN is trained with a massive number of subregions/subvolumes extracted from input images together with teaching pixels; hence the term “massive training”. 2D MTANNs have been applied for reduction of FPs in the computerized detection of lung nodules in low-dose CT [33-35] and chest radiography [36, 37], for distinction between benign and malignant lung nodules in CT [38], for suppression of ribs in chest radiographs [39], and for enhancing lesions on CT images [40].

Suzuki et al. developed a 3D MTANN by extending the structure of a 2D MTANN to process 3D volume data in CTC. The architecture and training of a 3D MTANN are shown in Fig. 1. A 3D MTANN consists of a linear-output multilayer ANN regression model, which is capable of operating on voxel data directly [32],[30]. The 3D MTANN is trained with input CTC volumes and the corresponding “teaching” volumes for enhancement of polyps and suppression of non-polyps. The input to the 3D MTANN consists of voxel values in a sub-volume, V_S, extracted from an input volume. The output of the 3D MTANN is a continuous scalar value, which is associated with the center voxel in the sub-volume and is represented by

$$O(x, y, z) = NN\{I(x - p, y - q, z - r) \mid (p, q, r) \in V_S\}, \tag{1}$$

where $NN(\cdot)$ is the output of the linear-output ANN regression model, and $I(x,y,z)$ is a voxel value of the input volume. For enhancement of polyps and suppression of non-polyps in CTC volumes, the teaching volume contains a 3D Gaussian distribution with standard deviation σ_T. This distribution represents the “likelihood of being a polyp” for a polyp and zero for a non-polyp:

$$T(x, y, z) = \begin{cases} \dfrac{1}{\sqrt{2\pi}\sigma_T} \exp\left\{-\dfrac{(x^2 + y^2 + z^2)}{2\sigma_T{}^2}\right\} & \textit{for a polyp} \\ 0 & \textit{otherwise}. \end{cases} \tag{2}$$

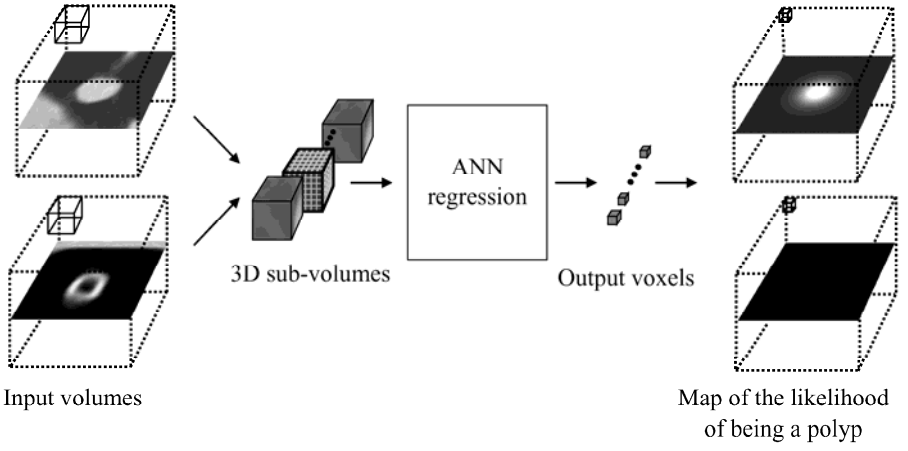

Fig. 1. Architecture and training of a 3D MTANN consisting of a linear-output multilayer ANN regression model and a massive-subvolumes training scheme

2.3 Non-machine-Learning-Based Methods

Some investigators developed FP reduction techniques based on non-machine-learning ways. Näppi et al. [41] developed a method for FP reduction based on supine-prone correspondence. Näppi et al. [42] also developed feature-guided analysis in colon segmentation and feature analysis of polyp candidates and compared them with their previously developed fuzzy clustering. They were able to reduce 70-75% more FPs with their new method, which combines both a non-machine-learning-based method and a feature-based classifer.

2.4 Reduction of Specific Type of FP

Some investigators developed techniques to reduce a specific type of FP. Suzuki et al. developed a 3D MTANN for distinction between polyps and rectal tubes in 3D CTC volumetric data [43]. Rectal tubes are one of major FPs produced by CADe schemes. Although rectal tubes are relatively obvious FPs, radiologists may lose their confidence in CADe as an effective tool if the CADe scheme generates such obvious FPs. Therefore, removal of rectal-tube-induced FPs is desirable. To address this issue, Suzuki et al. applied a 3D MTANN to the removal of rectal-tube-induced FPs. The 3D MTANN eliminated all rectal-tube-induced FPs, which corresponds to 8.9% (20/224) of all FPs, without removal of any true positives. Iordanescu et al. [44] developed an image-segmentation-based approach for the reduction of FPs due to rectal tubes. Their method finds the hole of a rectal tube by matched filtering, extrapolates the axis, and segments the rectal tube by a conditional morphologic dilation method. This method was able to track and label 72% of rectal tubes successfully, and to reduce FPs by 9.2%. Summers et al. [45] developed a method for the reduction of FPs caused by the ileocecal valve, which is a major FP source. Their method eliminated 61% of FPs due to the ileocecal valve and none of true positives.

3 FP Reduction with MTANNs

Suzuki et al. [46, 47] used a mixture of expert MTANNs to remove various types of FPs in a CADe scheme for detection of polyps in CTC. Suzuki et al. [48, 49] improved the efficiency of the MTANN approach by incorporating the principal component analysis-based and Laplacian eigenmap-based dimension reduction techniques. Xu and Suzuki [50] showed that other nonlinear regression models such as support vector and nonlinear Gaussian process regression models instead of the ANN regression model could be used as the core model in the MTANN framework.

3.1 CTC Database

CTC examinations were performed on 73 patients at The University of Chicago Medical Center. The patients' colons were prepared by standard pre-colonoscopy cleansing with administration of cathartics following a water diet or low-fiber diet, and they were insufflated with room air or carbon dioxide. Each patient was scanned in both supine and prone positions. The database thus contained 146 CTC datasets. The CT scans were performed with either a single- or a multi-detector-row CT scanner (HiSpeed CTi or LightSpeed QX/i, GE Medical Systems, Milwaukee, WI). The CT scanning parameters included collimations between 2.5 and 5.0 mm, reconstruction intervals of 1.0-5.0 mm, and tube currents of 60-120 mA with 120 kVp. Each reconstructed CT section had a matrix size of 512 x 512 pixels, with an in-plane pixel size of 0.5-0.7 mm. All patients underwent "reference-standard" optical colonoscopy. Radiologists established the locations of polyps in the CTC datasets by use of the colonoscopy and pathology reports, as well as multiplanar reformatted views of the CTC on a viewing workstation. In this study, we used 5 mm as the threshold for clinically significant polyps [48]. Fifteen patients had 28 polyps, 15 of which were 5-9 mm in diameter, and 13 were 10-25 mm.

3.2 Evaluation

Suzuki et al. applied a previously reported CADe scheme [42, 49] to the 73 CTC cases. The scheme included centerline-based extraction of the colon [50], shape-based detection of polyps [8, 10], and initial reduction of FPs by use of a Bayesian ANN based on geometric and texture features [18, 42]. They evaluated supine and prone CTC volumes independently. This CADe scheme achieved a 96.4% (27/28 polyps) by-polyp sensitivity with an average of 3.1 (224/73) FPs per patient. Forty-eight true-positive polyp detections in both supine and prone CTC volumes represented 27 polyps. They combined their previously reported CADe scheme with the mixture of expert 3D MTANNs for further reduction of FPs.

To distinguish between polyps and FPs, they merged the scores from the four individual expert 3D MTANNs with a mixing ANN. They evaluated the overall performance of the mixture of expert 3D MTANNs for FP reduction by use of free-response receiver-operating-characteristic (FROC) analysis. The FROC curve was obtained by a change in the threshold value for the output of the mixing ANN. This FROC curve indicates that the mixture of expert 3D MTANNs was able to eliminate 63% (142/224) of non-polyps (FPs) without removal of any of the 27 polyps, i.e., a 96.4% (27/28) overall by-polyp sensitivity was achieved at an FP rate of 1.1 (82/73) per patient.

4 Conclusion

FP reduction is a crucial step in CADe schemes for detection of polyps in CTC. There are three classes of FP reduction techniques: feature-based classifiers, pixel-based machine learning, and non-machine-learning-based methods.

Acknowledgments. This work was supported by Grant Number NIH/NCI R01CA 120549 and partially by NIH S10 RR021039 and P30 CA14599.

References

1. Jemal, A., Murray, T., Ward, E., Samuels, A., Tiwari, R.C., Ghafoor, A., Feuer, E.J., Thun, M.J.: Cancer statistics. CA. Cancer J. Clin. 30, 10–30 (2005)
2. Winawer, S.J., Fletcher, R.H., Miller, L., Godlee, F., Stolar, M.H., Mulrow, C.D., Woolf, S.H., Glick, S.N., Ganiats, T.G., Bond, J.H., Rosen, L., Zapka, J.G., Olsen, S.J., Giardiello, F.M., Sisk, J.E., Van Antwerp, R., Brown-Davis, C., Marciniak, D.A., Mayer, R.J.: Colorectal cancer screening: clinical guidelines and rationale. Gastroenterology 112, 594–642 (1997)
3. Dachman, A.H.: Atlas of Virtual Colonoscopy. Springer, New York (2003)
4. Macari, M., Bini, E.J.: CT colonography: where have we been and where are we going? Radiology 237, 819–833 (2005)
5. Fletcher, J.G., Booya, F., Johnson, C.D., Ahlquist, D.: CT colonography: unraveling the twists and turns. Curr. Opin. Gastroenterol 21, 90–98 (2005)
6. Yoshida, H., Dachman, A.H.: Computer-aided diagnosis for CT colonography. Semin Ultrasound CT MR 25, 419–431 (2004)
7. Yoshida, H., Dachman, A.H.: CAD techniques, challenges, and controversies in computed tomographic colonography. Abdom Imaging 30, 26–41 (2005)
8. Yoshida, H., Masutani, Y., MacEneaney, P., Rubin, D.T., Dachman, A.H.: Computerized detection of colonic polyps at CT colonography on the basis of volumetric features: pilot study. Radiology 222, 327–336 (2002)
9. Yoshida, H., Näppi, J., MacEneaney, P., Rubin, D.T., Dachman, A.H.: Computer-aided diagnosis scheme for detection of polyps at CT colonography. Radiographics 22, 963–979 (2002)
10. Yoshida, H., Näppi, J.: Three-dimensional computer-aided diagnosis scheme for detection of colonic polyps. IEEE Trans. Med. Imaging 20, 1261–1274 (2001)
11. Summers, R.M., Johnson, C.D., Pusanik, L.M., Malley, J.D., Youssef, A.M., Reed, J.E.: Automated polyp detection at CT colonography: feasibility assessment in a human population. Radiology 219, 51–59 (2001)
12. Paik, D.S., Beaulieu, C.F., Rubin, G.D., Acar, B., Jeffrey, R.B., Yee Jr, J., Dey, J., Napel, S.: Surface normal overlap: a computer-aided detection algorithm with application to colonic polyps and lung nodules in helical CT. IEEE Trans. Med. Imaging 23, 661–675 (2004)
13. Kiss, G., Van Cleynenbreugel, J., Thomeer, M., Suetens, P., Marchal, G.: Computer-aided diagnosis in virtual colonography via combination of surface normal and sphere fitting methods. Eur. Radiol. 12, 77–81 (2002)
14. Summers, R.M., Yao, J., Pickhardt, P.J., Franaszek, M., Bitter, I., Brickman, D., Krishna, V., Choi, J.R.: Computed tomographic virtual colonoscopy computer-aided polyp detection in a screening population. Gastroenterology 129, 1832–1844 (2005)
15. Fukunaga, K.: Introduction to Statistical Pattern Recognition. Academic Press, San Diego (1990)
16. Rumelhart, D.E., Hinton, G.E., Williams, R.J.: Learning representations by back-propagating errors. Nature 323, 533–536 (1986)
17. Vapnik, V.N.: The Nature of Statistical Learning Theory. Springer, Berlin (1995)

18. Nappi, J., Yoshida, H.: Automated detection of polyps with CT colonography: evaluation of volumetric features for reduction of false-positive findings. Acad. Radiol. 9, 386–397 (2002)
19. Gokturk, S.B., Tomasi, C., Acar, B., Beaulieu, C.F., Paik, D.S., Jeffrey, R.B., Yee Jr, J., Napel, S.: A statistical 3-D pattern processing method for computer-aided detection of polyps in CT colonography. IEEE Transactions on Medical Imaging 20, 1251–1260 (2001)
20. Acar, B., Beaulieu, C.F., Gokturk, S.B., Tomasi, C., Paik, D.S., Jeffrey, R.B., Yee Jr, J., Napel, S.: Edge displacement field-based classification for improved detection of polyps in CT colonography. IEEE Transactions on Medical Imaging 21, 1461–1467 (2002)
21. Jerebko, A.K., Summers, R.M., Malley, J.D., Franaszek, M., Johnson, C.D.: Computer-assisted detection of colonic polyps with CT colonography using neural networks and binary classification trees. Medical Physics 30, 52–60 (2003)
22. Jerebko, A.K., Malley, J.D., Franaszek, M., Summers, R.M.: Multiple neural network classification scheme for detection of colonic polyps in CT colonography data sets. Academic Radiology 10, 154–160 (2003)
23. Jerebko, A.K., Malley, J.D., Franaszek, M., Summers, R.M.: Support vector machines committee classification method for computer-aided polyp detection in CT colonography. Academic Radiology 12, 479–486 (2005)
24. Wang, Z., Liang, Z., Li, L., Li, X., Li, B., Anderson, J., Harrington, D.: Reduction of false positives by internal features for polyp detection in CT-based virtual colonoscopy. Med. Phys. 32, 3602–3616 (2005)
25. Li, J., Van Uitert, R., Yao, J., Petrick, N., Franaszek, M., Huang, A., Summers, R.M.: Wavelet method for CT colonography computer-aided polyp detection. Med. Phys. 35, 3527–3538 (2008)
26. Wang, S., Yao, J., Summers, R.M.: Improved classifier for computer-aided polyp detection in CT colonography by nonlinear dimensionality reduction. Med. Phys. 35, 1377–1386 (2008)
27. Yao, J., Li, J., Summers, R.M.: Employing Topographical Height Map In Colonic Polyp Measurement And False Positive Reduction. Pattern Recognit. 42, 1029–1040 (2009)
28. Hongbin, Z., Zhengrong, L., Perry, J.P., Matthew, A.B., Jiangsheng, Y., Yi, F., Hongbing, L., Erica, J.P., Robert, J.R., Harris, L.C.: Increasing computer-aided detection specificity by projection features for CT colonography. Medical Physics 37, 1468–1481 (2010)
29. Suzuki, K., Horiba, I., Sugie, N.: Efficient approximation of neural filters for removing quantum noise from images. IEEE Trans. Signal Process. 50, 1787–1799 (2002)
30. Suzuki, K., Horiba, I., Sugie, N.: Neural edge enhancer for supervised edge enhancement from noisy images. IEEE Trans. Pattern Anal. Mach. Intell. 25, 1582–1596 (2003)
31. Suzuki, K., Horiba, I., Sugie, N., Nanki, M.: Neural filter with selection of input features and its application to image quality improvement of medical image sequences. IEICE Trans. Inf. Syst. E85-D, 1710–1718 (2002)
32. Suzuki, K., Horiba, I., Sugie, N., Nanki, M.: Extraction of left ventricular contours from left ventriculograms by means of a neural edge detector. IEEE Trans. Med. Imaging 23, 330–339 (2004)
33. Suzuki, K., Armato, S.G., Li, F., Sone, S., Doi, K.: Massive training artificial neural network (MTANN) for reduction of false positives in computerized detection of lung nodules in low-dose CT. Med. Phys. 30, 1602–1617 (2003)
34. Suzuki, K., Doi, K.: How can a massive training artificial neural network (MTANN) be trained with a small number of cases in the distinction between nodules and vessels in thoracic CT? Acad. Radiol. 12, 1333–1341 (2005)
35. Arimura, H., Katsuragawa, S., Suzuki, K., Li, F., Shiraishi, J., Sone, S., Doi, K.: Computerized scheme for automated detection of lung nodules in low-dose computed tomography images for lung cancer screening. Acad. Radiol. 11, 617–629 (2004)

36. Suzuki, K., Shiraishi, J., Abe, H., MacMahon, H., Doi, K.: False-positive reduction in computer-aided diagnostic scheme for detecting nodules in chest radiographs by means of massive training artificial neural network. Acad. Radiol. 12, 191–201 (2005)
37. Oda, S., Awai, K., Suzuki, K., Yanaga, Y., Funama, Y., MacMahon, H., Yamashita, Y.: Performance of radiologists in detection of small pulmonary nodules on chest radiographs: effect of rib suppression with a massive-training artificial neural network. AJR. Am. J. Roentgenol. 193, W397–W402 (2009)
38. Suzuki, K., Li, F., Sone, S., Doi, K.: Computer-aided diagnostic scheme for distinction between benign and malignant nodules in thoracic low-dose CT by use of massive training artificial neural network. IEEE Trans. Med. Imaging 24, 1138–1150 (2005)
39. Suzuki, K., Abe, H., MacMahon, H., Doi, K.: Image-processing technique for suppressing ribs in chest radiographs by means of massive training artificial neural network (MTANN). IEEE Trans. Med. Imaging 25, 406–416 (2006)
40. Suzuki, K.: A supervised 'lesion-enhancement' filter by use of a massive-training artificial neural network (MTANN) in computer-aided diagnosis (CAD). Phys. Med. Biol. 54, S31–S45 (2009)
41. Nappi, J., Okamura, A., Frimmel, H., Dachman, A., Yoshida, H.: Region-based supine-prone correspondence for the reduction of false-positive CAD polyp candidates in CT colonography. Acad. Radiol. 12, 695–707 (2005)
42. Nappi, J., Yoshida, H.: Feature-guided analysis for reduction of false positives in CAD of polyps for computed tomographic colonography. Med. Phys. 30, 1592–1601 (2003)
43. Suzuki, K., Yoshida, H., Nappi, J., Dachman, A.H.: Massive-training artificial neural network (MTANN) for reduction of false positives in computer-aided detection of polyps: Suppression of rectal tubes. Med. Phys. 33, 3814–3824 (2006)
44. Iordanescu, G., Summers, R.M.: Reduction of false positives on the rectal tube in computer-aided detection for CT colonography. Medical Physics 31, 2855–2862 (2004)
45. Summers, R.M., Yao, J., Johnson, C.D.: CT colonography with computer-aided detection: automated recognition of ileocecal valve to reduce number of false-positive detections. Radiology 233, 266–272 (2004)
46. Suzuki, K., Rockey, D.C., Dachman, A.H.: CT colonography: Advanced computer-aided detection scheme utilizing MTANNs for detection of "missed" polyps in a multicenter clinical trial. Med. Phys. 30, 2–21 (2010)
47. Suzuki, K., Yoshida, H., Nappi, J., Armato 3rd, S.G., Dachman, A.H.: Mixture of expert 3D massive-training ANNs for reduction of multiple types of false positives in CAD for detection of polyps in CT colonography. Med. Phys. 35, 694–703 (2008)
48. Suzuki, K., Zhang, J., Xu, J.: Massive-training artificial neural network coupled with Laplacian-eigenfunction-based dimensionality reduction for computer-aided detection of polyps in CT colonography. IEEE Trans. Med. Imaging 29, 1907–1917 (2010)
49. Suzuki, K., Xu, J., Zhang, J., Sheu, I.: Principal-Component Massive-Training Machine-Learning Regression for False-Positive Reduction in Computer-Aided Detection of Polyps in CT Colonography. In: Wang, F., Yan, P., Suzuki, K., Shen, D. (eds.) MLMI 2010. LNCS, vol. 6357, pp. 182–189. Springer, Heidelberg (2010)
50. Xu, J., Suzuki, K.: Massive-training support vector regression and Gaussian process for false-positive reduction in computer-aided detection of polyps in CT colonography. Med. Phys. 38, 1888–1902 (2011)
51. Johnson, C.D., Dachman, A.H.: CT colonography: the next colon screening examination? Radiology 216, 331–341 (2000)
52. Yoshida, H., Nappi, J.: Three-dimensional computer-aided diagnosis scheme for detection of colonic polyps. IEEE Trans. Med. Imaging 20, 1261–1274 (2001)
53. Frimmel, H., Nappi, J., Yoshida, H.: Fast and robust computation of colon centerline in CT colonography. Med. Phys. 31, 3046–3056 (2004)

A Bayesian Approach for False Positive Reduction in CTC CAD

Xujiong Ye, Gareth Beddoe, and Greg Slabaugh

Medicsight PLC, London, UK

Abstract. This paper presents an automated detection method for identifying colonic polyps and reducing false positives (FPs) in CT images. It formulates the problem of polyp detection as a probability calculation through a unified Bayesian statistical model. The polyp likelihood is modeled with a combination of shape and intensity features. A second principal curvature PDE provides a shape model; and the partial volume effect is considered in modeling of the polyp intensity distribution. The performance of the method was evaluated on a large multi-center dataset of colonic CT scans. Both qualitative and quantitative experimental results demonstrate the potential of the proposed method.

Keywords: colon CAD, colonic polyp detection, Bayesian framework.

1 Introduction

Typical approaches to computed tomography (CT) colonography (CTC) CAD can be classified as shape-based. Shape-based methods typically rely on various shape features derived from either first-order differential geometric quantities [1] or from second-order quantities computed by use of Hessian matrices [2-4]. The shape features take advantage of the fact that polyps tend to have rounded shapes or at least contain local spherical elements, whereas colonic folds have elongated shapes. However, in practice, polyps are often abnormal growths that exhibit varying morphology, and shape-based methods may fail to detect polyps with sufficient reliability. Therefore, in addition to shape-based features, other features such as those based on appearance can also be used to improve detection performance. Appearance-based features include image intensity either directly or indirectly through intensity related features, which take advantage of the fact that polyps typically exhibit a slightly elevated intensity and inhomogeneous texture relative to the surrounding mucosal tissue.

Our goal in this paper is to incorporate shape features with appearance features in a unified Bayesian framework to reduce false positives (FPs) in colon CAD. For each voxel within the candidate region, our method estimates the probability that the voxel is contained within a polyp. The advantages of a Bayesian technique are as follows. First, statistical techniques are ideally suited to modeling the large uncertainty inherent in detection problems in medical imaging. Second, there often is useful medical knowledge (such as lesion density, size, shape, etc.) that can be utilized to

H. Yoshida et al. (Eds.): Virtual Colonoscopy and Abdominal Imaging 2010, LNCS 6668, pp. 40–46, 2011.

constrain the solution of detection problems. This prior medical knowledge can be easily encoded into a Bayesian model. Finally, a Bayesian technique provides a unified framework for incorporating various features *F* into one statistical model.

Mendonca *et al.* [5] formed a probability distribution function for each *voxel* in the image based on simplified geometric models (ellipsoidal polyps, spherical colon wall, etc.), which preclude a specific training step. However, these parametric models have limited capability to model the complexity of actual polyps in the human anatomy. Our approach uses a more expressive shape model that has been shown to model the variation in polyp shapes. Also, the proposed framework includes prior medical knowledge through explicit learning based on labeled examples. To our knowledge, this is the first time such a learning-based Bayesian approach for modeling the likelihood of polyp voxels has been proposed in a CTC CAD system.

The proposed method has been applied to the candidate regions found by our previous CAD algorithm [6]. Quantitative evaluation on a large multi-center clinical dataset of colonic CT scans shows the excellent performance of the method, which reduces the FPs by an average 16%, while keeping the same sensitivity.

2 Method

We are given a set of voxels $X = \{x_i, i = 1,..., N\}$ in a 3D image, a set of features $F = \{F_j,\ \mathrm{j} = 1, ..., \mathrm{M}\}$ associated with each voxel x_i, and a set of labels $\Lambda = \{l_0 ... l_{K-1}\}$. Here, we use K=2, where, l_0 is a non-polyp label, whereas l_1 is a polyp label. This paper focuses on assigning one of the labels to individual image voxels within a candidate region based on a probability calculation through a unified Bayesian framework. Two features are considered: the intensity *I* and shape *S*; namely, $F_1 = I$, $F_2 = S$. Whereas we focus on these two features, the framework is extensible to other features as well.

Assuming that each feature F_j is conditionally independent, the probability of a polyp label at each pixel can be calculated based on Bayes' law:

$$P(X|F) = \frac{P(F|X) \cdot P(X)}{P(F)} = \frac{P(F_1|X) \cdot P(F_2|X) \cdot P(X)}{P(F_1) \cdot P(F_2)} \tag{1}$$

The posterior, likelihood, and prior terms are $P(X|F)$, $P(F|X)$ and $P(X)$. In this paper, a uniform prior is used.

The goal is to use Eq. 1 to model the probability of a polyp label existing at each voxel within each candidate region. A block diagram of the proposed method is illustrated in Fig. 1. Below each stage is described in detail.

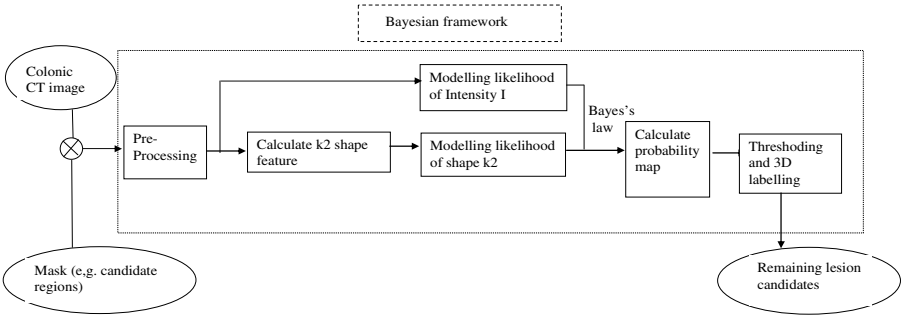

Fig. 1. Block diagram of the proposed Bayesian method for FP reduction

2.1 Modeling the Likelihood Term

In the Bayesian framework, the likelihood term indicates the joint density distribution of all features for class l_1. It is noted that, to calculate each feature accurately, during the pre-processing step, a Gaussian filter is applied to remove noise.

2.1.1 Intensity Model

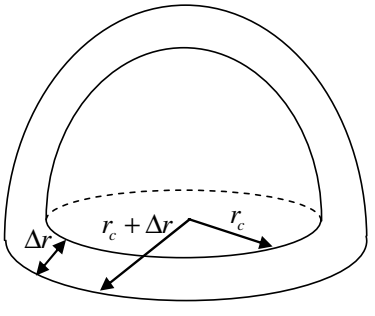

Fig. 2. A schematic diagram of colonic polyp

It is well known that CT images exhibit a partial volume effect (PVE) due to the limitations in scanning resolution. For tissues like polyps near air, the boundary of the polyp may appear darker than that of its central region as a result of the PVE. Assume that a polyp has a hemispherical shape and contains two parts: a core part (r_c) with mean intensity μ_{Ic} and a PVE part (Δr) with the mean intensity μ_{Ip}. Fig. 2 is a schematic diagram of the polyp.

For the purpose of false-positive reduction, the candidate region's size can be incorporated into the intensity model to address the PVE. For each candidate region, a sub-image is extracted. The polyp intensity model varies for each polyp region and can be given by a Gaussian function:

$$P(F_1|X) = \exp\left(-\frac{(F_1-\mu_I)^2}{\delta_I^2}\right) = \exp\left(-\frac{(I-\mu_I)^2}{\delta_I^2}\right) \quad (2)$$

where μ_I can be defined as a function of potential polyp size (e.g., radius *r*), namely, $\mu_I = f(r)$. Given the whole polyp radius as $r = r_c + \Delta r$, the mean intensity of a polyp is adaptively determined as:

$$\mu_I = f \cdot \mu_{Ic} + (1 - f) \cdot \mu_{Ip} \tag{3}$$

where *f* is the fraction of the core part's volume compared to the whole polyp's volume, namely, $f = r_c^3 / r^3 = (r - \Delta r)^3 / r^3$.

When a polyp is very small, there might be no core part, namely $r_c = 0$ and $f = 0$, so the mean intensity μ_I depends on the mean intensity of PVE μ_{Ip}. In contrast, when a polyp is very large, e.g., $r \to \infty$, we have $f = 1$, and the mean intensity μ_I depends on the mean intensity of the core part.

2.1.2 Shape Model

The second principal curvature (K2) partial differential equation (PDE, or *flow*) for polyp detection was recently introduced by van Wijk *et al.* [4]. Our aim in this section is to model the K2 flow feature's distribution and combine it into the joint statistical likelihood term of the Bayesian framework.

The vast majority of polyps are raised objects protruding on the colon surface, which means that their first and second principal curvatures have positive values. In contrast, colonic folds are elongated structures, bent only in one direction, and correspondingly exhibit a positive first principal curvature and a close-to-zero second principal curvature. Therefore, for detection of polyps, a flow based on the second principal curvature can be designed that affects only points with a positive second principal curvature in such a way that the second principal curvature decreases. Repeated application of the PDE on an image will gradually deform the image, reducing and then removing surface protrusions.

A PDE flow to remove protruding objects can be defined as

$$\frac{\partial I}{\partial t} = \begin{cases} -k_2(x_i) \cdot |\nabla I| & (k_2(x_i) > 0) \\ 0 & (k_2(x_i) \le 0) \end{cases} \tag{4}$$

where $k_2(x_i)$ is the second principal curvature at image voxel x_i, and $|\nabla I|$ is the gradient magnitude of the input image.

Based on Eq. 4, the image intensities exhibit a small (if any) change for folds, and a large change for protruding objects (such as polyps). During each iteration, only at locations of protruding objects is the image intensity reduced by an amount proportional to the local second derivative k_2. After the PDE reaches a steady state, the difference image *D* between the input and the deformed images indicates the amount of protrusion. By design, it discriminates between polyps and folds and is

robust to different polyp morphologies and sizes. A truncated Gaussian function is used to model the polyp likelihood as a function of the intensity difference $F_2^{k2} = D$. The truncated Gaussian function allows a larger range of voxels with high K2 flow have high probability of being polyp labels.

$$P(F_2^{k2}|X) = \exp\left(-\frac{(F_2^{k2}-\mu_{k2})^2}{\delta_{k2}^2}\right), \text{ when } F_2^{k2} > \mu_{k2}, P(F_2^{k2}|X) = 1 \quad (5)$$

where μ_{k2} and δ_{k2} are the mean and standard deviation (*std*), respectively, determined through a training dataset.

We compared this K2 flow to other second-order shape features such as the shape index [2]. Fig.3 shows a comparison applied to two polyps (a) (with one polyp attached to the colonic wall, whereas the other polyp is attached to the colonic fold). It can be seen that both the intensity likelihood map (b) and the shape likelihood map (c and e) are highlighting the polyps. However, compared to the shape likelihood map calculated based on the shape index (c), the proposed K2 difference map (e) shows a superior performance with very few false regions in the entire sub-image. Fig. 3(f) is the final polyp probability map from the intensity and K2 flow likelihoods (Eq.1). It is noted that, by use of the proposed Bayesian method with the K2 flow shape model, both polyps can be detected and properly segmented from the surrounding tissues.

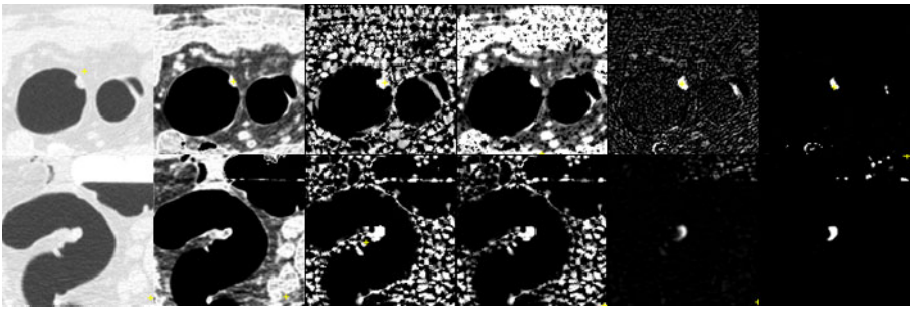

(a) (b) (c) (d) (e) (f)

Fig. 3. Results of the Bayesian method comparing two different shape features on two polyps (a) CT sub-image; (b) intensity probability; (c) shape index probability; (d) joint (Bayesian) probability based on intensity and shape index probability; (e) K2 flow difference image; (f) joint (Bayesian) probability based on intensity and K2 probability

3 Experimental Results and Discussion

The proposed Bayesian method has been trained and evaluated on CT colon images. The entire dataset is divided into a training set and an independent testing set. There are 68 scans containing 70 polyps in the training set. The training set is used to

optimize model parameters. In this paper, each feature likelihood term in Eq. 1 is associated with one rule for polyp detection. The parameters for each model that provide good cut-off in a ROC curve are chosen.

In our previous work, we have developed an entire automatic CT colonic polyp detection algorithm [6]. The aim of this experiment is to use the proposed Bayesian method for further removal of false regions. For each candidate region, a polyp probability map based on a Bayesian framework (Eq.1) is calculated, where, the intensity model is based on Eq.2 and the K2 feature is used for the shape model. Hysteresis thresholding and 3D labeling are then applied on each probability map. If a candidate region contains a set of 3D connected voxels with high probabilities of "polypness", the region is kept as a potential polyp region. Otherwise, the region is considered to be a non-polyp region and is removed from the polyp candidates.

For a quantitative evaluation of the performance, the method has been tested on our latest independent dataset of 59 patients (118 CT volumes) of prone and supine volumes collected from 4 institutions, with a total of 75 polyps. Fig. 4 shows FROC curves based on our previous CAD algorithm only and the further FP reduction based on the proposed Bayesian method. It can be seen that, with the same sensitivity, the Bayesian method reduces the FPs by an average of 16%. For example, with a sensitivity of 93.3%, the FP rate can be decreased from 6.2 per volume to 5.2 per volume after applying the Bayesian method. As we keep the same sensitivity for the proposed method, the improved curve looks a shift compared to the previous curve. This demonstrates the effectiveness of the proposed algorithm in the false-positive reduction. (It is noted that, in this experiment, the sensitivity is measured per polyp, that is, if a polyp is detected on either or both volumes, it is considered a true positive, and false positives are measured per volume, as is the convention in CTC).

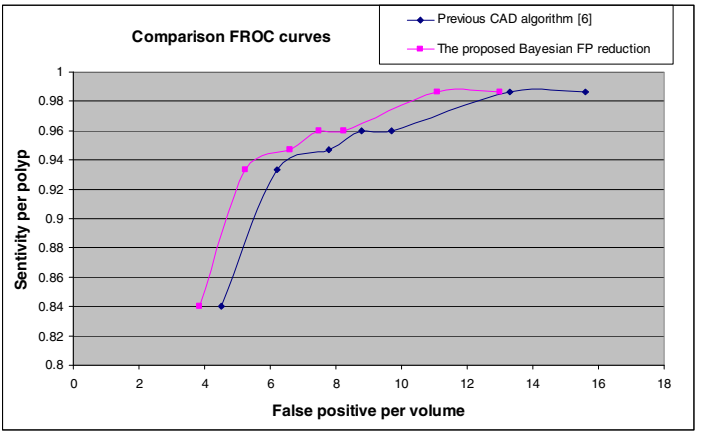

Fig. 4. FROC curves demonstrating the improvement of the Bayesian approach compared to our previous CAD algorithm

4 Conclusion

We have presented a Bayesian approach to the reduction of false positives in CTC CAD. For each candidate region, the polyp likelihood is modeled by use of a combination of shape and intensity features. The second principal curvature flow is used as a shape model, while PVE is considered into modeling of the polyp intensity distribution. The proposed method has been applied on the candidate regions obtained from our previous CAD algorithm [6] on a multi-center dataset of colonic CT, and it shows an average 16% reduction of FPs while keeping the same sensitivity. The method provides a robust and consistent performance.

The Bayesian framework is general and can be flexibly extended to incorporate other features, Indeed, one could imagine incorporating other image features (location, texture) as well as patient informatics (age, family history of colorectal disease) for robust detection. The algorithm can also be easily adapted to candidate generation step of CAD system.

References

1. Paik, D.S., Beaulieu, C.F., Rubin, G.D., Acar, B., Jeffrey, R.B., Yee, J., Dey, J., Napel, S.: Surface normal overlap: A computer-aided detection algorithm with application to colonic polyps and lung nodules in helical CT. IEEE Trans. Medical Imaging 23(6) (2004)
2. Yoshida, H., Nappi, J.: Three-dimensional computer-aided diagnosis scheme for detection of colonic polyps. IEEE Trans. Medical Imaging 20, 1261–1274 (2001)
3. Summers, R., Yao, J., Pickhardt, P., Franaszek, M., Bitter, I., Brickman, D., Choi, J.R.: Computed tomographic virtual colonoscopy computer-aided polyp detection in a screening population. Gastroenterology 129, 1832–1844 (2005)
4. van Wijk, C., van Ravesteijn, V.F., Vos, F.M., van Vliet, L.J.: Detection and segmentation of colonic polyps on implicit isosurfaces by second principal curvature flow. IEEE Trans. Medical Imaging 29(3), 688–698 (2010)
5. Mendonca, P.R.S., Bhotika, R., Zhao, F., Melonakos, J., Sirohey, S.: Detection of polyps via shape and appearance modeling. In: Proc MICCAI 2008 Workshop: Computational and Visualization Challenges in the New Era of Virtual Colonoscopy (2008)
6. Slabaugh, G., Yang, X., Ye, X., Boyes, R., Beddoe, G.: A Robust and Fast System for CTC Computer-Aided Detection of Colorectal Lesions. Algorithms (2010)

False-Positive Reduction in Computer-Aided Detection of Polyps in CT Colonography: A Massive-Training Support Vector Regression Approach

Jian-Wu Xu and Kenji Suzuki

Department of Radiology, The University of Chicago,
5841 South Maryland Avenue, Chicago, IL 60637
{jwxu,suzuki}@uchicago.edu

Abstract. A massive-training artificial neural network (MTANN) has been investigated for reduction of false positives (FPs) in computer-aided detection (CADe) of polyps in CT colonography (CTC). A major limitation of the MTANN is a long training time. To address this issue, we investigated the feasibility of a support vector regression (SVR) in the massive-training framework and developed a massive-training SVR (MTSVR). To test the proposed MTSVR, we compared it with the original MTANN in FP reduction in CADe of polyps in CTC. With MTSVR, we reduced the training time by a factor of 190, while achieving a performance (by-polyp sensitivity of 94.7% with 2.5 FPs/patient) comparable to that of the original MTANN (which has the same sensitivity with 2.6 FPs/patient).

Keywords: colorectal cancer, computer-aided detection, false-positive reduction, pixel-based machine learning, support vector regression.

1 Introduction

One of the major challenges in current computer-aided detection (CADe) of polyps in CT colonography (CTC) is to improve the specificity without sacrificing the sensitivity. If a large number of false-positive (FP) detections is produced by a CADe scheme, radiologists might lose their confidence in CADe. A CADe scheme [1] generally employs a classifier based on features extracted from each segmented candidate to distinguish between polyps and non-polyps. In order to reduce FPs produced by the feature-based classifier, Suzuki *et al.* developed a massive-training artificial neural network (MTANN) based on an ANN regression model [2]. The MTANN is a volume-processing technique that is trained directly with a massive number of subvolumes extracted from input CTC images together with "teaching" voxels to distinguish polyps from non-polyps; hence the term "massive training".

Because of the large number of subvolumes and the high dimensionality of voxels in each input subvolume, the training of an MTANN has been very time-consuming, i.e., 30-40 hours. Our purpose in this study was to investigate the feasibility of a support vector machine regression model (SVR) in the massive-training

H. Yoshida et al. (Eds.): Virtual Colonoscopy and Abdominal Imaging 2010, LNCS 6668, pp. 47–52, 2011.

volume-processing framework. Unlike an ANN that uses the back-propagation algorithm to minimize the mean-square error between outputs and teaching images, an SVR is a large margin regression model that minimizes the hinge loss based on quadratic programming. Therefore, an SVR might offer less computational complexity in the massive-training framework while maintaining a comparable performance.

2 Massive-Training Support Vector Regression (MTSVR)

2.1 Architecture and Training of MTSVR

The architecture and training of a 3D MTSVR are illustrated in Fig. 1. An MTSVR consists of an SVR model whose inputs are voxel values extracted from CTC images directly. The output of the MTSVR is a continuous scalar value, which is associated with the center voxel in the sub-volume, V_S, and is defined as

$$O(x, y, z) = SVR\left\{I(x - p, y - q, z - r) \mid (p, q, r) \in V_S\right\}, \tag{1}$$

where $SVR\{\cdot\}$ is the output of the SVR, and $I(x,y,z)$ is a voxel value in a sub-volume that is extracted from an input volume.

For enhancement of polyps and suppression of non-polyps in CTC volumes, the teaching volume contains a 3D Gaussian distribution with standard deviation σ_T. This distribution represents the "likelihood of being a polyp" for a polyp and zero for a non-polyp:

$$T(x, y, z) = \begin{cases} \dfrac{1}{\sqrt{2\pi}\sigma_T} \exp\left\{-\dfrac{x^2 + y^2 + z^2}{2\sigma_T^{\,2}}\right\} & \text{for a polyp,} \\ 0 & \text{for non-polyps.} \end{cases} \tag{2}$$

A training sub-volume is extracted from a quasi-spherical region from the input CTC volumes. The center voxel from the corresponding teaching sub-volume is also extracted as the teaching value. The 3D MTSVR is massively trained by use of each of a large number of input sub-volumes together with each of the corresponding teaching single voxels; hence the term "massive-training SVR." After training, the 3D MTSVR is expected to output a higher value for a polyp and a lower value for a non-polyp.

In order to combine the output voxels from the trained 3D MTSVR, we developed a 3D scoring method that translates the output volume into a single scalar value. A score for a given polyp candidate from the 3D MTSVR is defined as

$$S = \sum_{(x,y,z) \in V_E} f_G(\sigma; x, y, z) \times O(x, y, z), \tag{3}$$

where $f_G()$ is a 3D Gaussian weighting function with standard deviation σ, and V_E is a volume for evaluation. The purpose of weighting of the output volume with the 3D

Gaussian function is to combine the individual voxel values into a single score. The score is a weighted summation of the output voxel values. Because the 3D Gaussian weighting function is centered at zero, the higher the score value is, the more likely it is that the candidate is a polyp. Classification between polyps and non-polyps is made by thresholding of the scores.

2.2 Support Vector Regression (SVR)

The SVR model is rooted in a support vector machine (SVM) classifier that is based on the method of structural risk minimization [3, 4]. Unlike the conventional square loss function that is sensitive to the presence of outliers, the SVR model employs an ε-insensitive loss function that is robust to outliers. The ε-insensitive error measure ignores any errors of size less than ε. It is defined as

$$V_\varepsilon(e) = \begin{cases} 0 & \text{if } |e| < \varepsilon, \\ |e| - \varepsilon, & \text{otherwise.} \end{cases} \tag{4}$$

Therefore, any error falling into the ε-band is not counted towards loss. This is analogous to the SVM classifier with which data samples on the correct side of the decision boundary and far away from it are ignored in optimization.

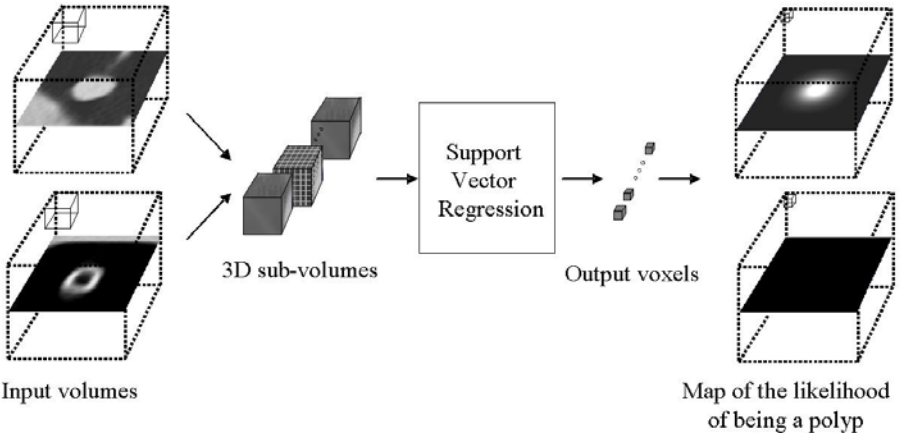

Fig. 1. Architecture and training of a 3D MTSVR. The input CTC volumes including a polyp or a non-polyp are divided voxel by voxel into a large number of overlapping 3D subvolumes.

Given a set of training data $\{(\mathbf{u}_i, d_i)\}_{i=1}^N$, where $(\mathbf{u}_i, d_i)$ are the sample values of the input vector $\mathbf{u}$ and model output d, a SVR aims at estimating the dependence of d on $\mathbf{u}$. The dependence, denoted as g, is represented as

$$g = \sum_{j=0}^{L} w_j \varphi_j(\mathbf{u}) = \mathbf{w}^{\mathrm{T}} \Psi(\mathbf{u}), \tag{5}$$

where $\Psi(\mathbf{u}) = [\varphi_0(\mathbf{u}), \varphi_1(\mathbf{u}), \ldots, \varphi_L(\mathbf{u})]^{\mathrm{T}}$ is the nonlinear functions associated with the reproducing kernel Hilbert space (RKHS), L is the dimension of the RKHS, which might be infinite, and $\mathbf{w} = [w_0, w_1, \ldots, w_L]^{\mathrm{T}}$ is the weights we aim to estimate. The SVR achieves this goal by minimizing the following empirical risk:

$$\min_{\mathbf{w}} \quad \sum_{i=1}^{N} V_{\varepsilon}(d_i - g_i) + \frac{\lambda}{2}\|\mathbf{w}\|^2, \tag{6}$$

where $V_\varepsilon(\bullet)$ is the *ε-insensitive* error function defined in Eq. (**4**), and λ is the regularization parameter. The optimal solution can be obtained through quadratic programming as

$$g(\mathbf{u}) = \sum_{i=1}^{N} (\alpha_i - \alpha_i') K(\mathbf{u}_i, \mathbf{u}), \tag{7}$$

where α_i and α_i' are positive Lagrange multipliers from the quadratic optimization, and $K(\mathbf{u}_i, \mathbf{u}_j)$ is a symmetric nonnegative inner-product kernel function defined in the RKHS as $K(\mathbf{u}_i, \mathbf{u}_j) = \Psi(\mathbf{u}_i)^{\mathrm{T}} \Psi(\mathbf{u}_j)$. We used the Gaussian kernel function for $K(\mathbf{u}_i, \mathbf{u}_j)$ in our experiment.

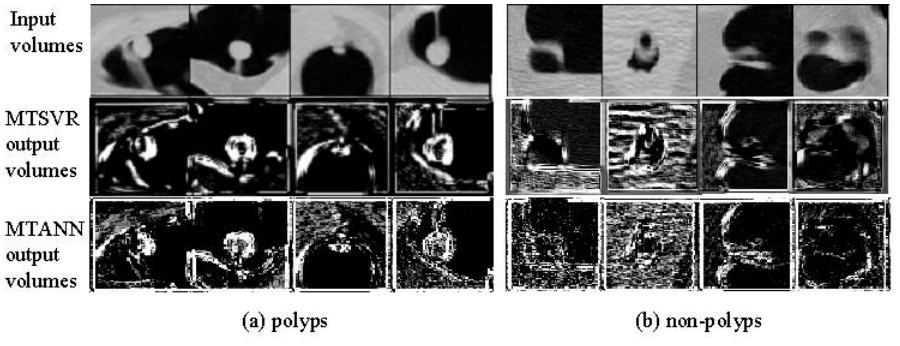

Fig. 2. Illustrations of the performance of the trained 3D MTSVR and MTANN with representative polyps and non-polyps, and the corresponding output volumes. The central axial slices of the 3D volumes are shown.

2.3 CTC Database and Evaluation

The database used in this study was acquired at the University of Chicago Medical Center. It consisted of 246 CTC datasets obtained from 123 patients. Each patient followed the standard CTC procedure with pre-colonoscopy cleansing and colon insufflation with room air or carbon dioxide. Both supine and prone positions were scanned. Each reconstructed CT section had a matrix size of 512×512 pixels, with an in-plane pixel size of 0.5-0.7 mm. Seventeen patients had 29 colonoscopy-confirmed polyps, 15 of which were 5-9 mm and 14 were 10-25 mm in size. The database was

divided into a training set and a testing set. The training set consisted of 30 patients, 10 of whom had 10 polyps. These 10 polyps and 10 non-polyps were used for training of the MTSVR. The testing set contained 93 patients, including 19 polyps in seven patients, and 86 negative patients. An initial CADe scheme for detection of polyps in CTC [5] was applied to the database. The CADe scheme is composed of 1) colon segmentation based on centerline tracing, 2) detection of polyp candidates based on the shape index and curvedness of the segmented colon, 3) calculation of 3D pattern features of the polyp candidates, and 4) classification of the polyp candidates as polyps or non-polyps based on quadratic discriminant analysis. The initial CADe scheme yielded a 94.7% (18/19) by-polyp sensitivity with 5.1 (474/93) FPs per patient for the testing set. The major sources of FPs included rectal tubes, stool, haustral folds, colonic walls, and the ileocecal valve. We used all 474 FPs produced by the initial CADe scheme and 37 true-positive polyp volumes as the testing data for MTSVR and MTANN.

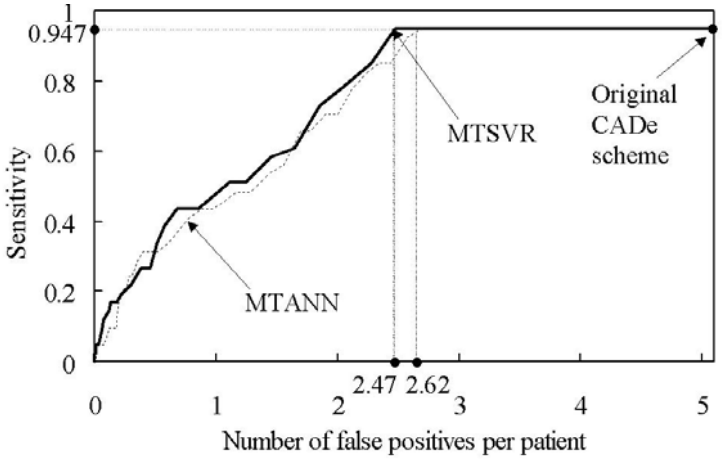

Fig. 3. FROC curves indicating the performance of the MTSVR and MTANN

To compare the proposed MTSVR with the original MTANN, we used the same training set to train both the models and the testing set for performance comparison. We used receiver-operating-characteristic (ROC) analysis [6] to assess the performance of the proposed MTSVR and the original MTANN in the task of distinguishing polyps from non-polyps. The area under the maximum-likelihood-estimated binormal ROC curve (AUC) was used as an index of performance. For the evaluation of the overall performance of a CADe scheme with the MTSVR and the original MTANN, free-response ROC (FROC) analysis was used.

3 Results

We selected four representative testing polyps and non-polyps to show different output volumes from MTSVR and MTANN in Fig. 2. Both trained models were able

to enhance the testing polyps and suppress the non-polyps. The ability of both methods to enhance small polyps can be demonstrated in the third image from the left in Fig. 2 (a). In the first and third images from the left in Fig. 2 (b), the testing non-polyps become dark in the output volumes of the MTSVR. However, the non-polyps can still be seen in the output volumes of theMTANN.

The AUC values obtained by the MTSVR and the MTANN were 0.79 and 0.77, respectively. However, the difference is not statistically significant (two-sided p-value = 0.75). Figure 3 shows FROC curves indicating the performance of the MTSVR and the original MTANN for FP reduction. The proposed MTSVR was able to eliminate 51.5% (244/474) of FPs without removal of any true-positives, i.e., it achieved a 94.7% (18/19) by-polyp sensitivity with an FP rate of 2.47 (230/93) per patient, whereas the MTANN eliminated 47.2% (230/474) of the FPs, which resulted in the same sensitivity with 2.62 (244/93) FPs per patient.

The training of the original MTANN took 38 hours on a workstation (Intel, Xeon, 2.7GHz), whereas that of the MTSVR took 12 minutes. With the SVR approach, the computational complexity was reduced by a factor of 190.

4 Conclusion

We have developed an MTSVR to reduce FPs in a CADe scheme for the detection of polyps in CTC. With the MTSVR, the training time was reduced substantially from 38 to 0.2 hours, while a performance comparable to that of the original MTANN (i.e., reduction of one half of FPs without removal of any true positive) was maintained. Therefore, both MTSVR and MTANN would be useful for improving the specificity of a CADe scheme, but MTSVR is substantially more efficient in training.

Acknowledgments. This work was supported by Grant Number R01CA120549 from the NCI/NIH and partially by NIH S10 RR021039 and P30 CA14599.

References

1. Summers, R.M., Handwerker, L.R., Pickhardt, P.J., Van Uitert, R.L., Deshpande, K.K., Yeshwant, S., Yao, J., Franaszek, M.: Performance of a previously validated CT colonography computer-aided detection system in a new patient population. AJR. Am. J. Roentgenol 191, 168–174 (2008)
2. Suzuki, K., Yoshida, H., Nappi, J., Dachman, A.H.: Massive-training artificial neural network (MTANN) for reduction of false positives in computer-aided detection of polyps: Suppression of rectal tubes. Med. Phys. 33, 3814–3824 (2006)
3. Vapnik, V.N.: The Nature of Statistical Learning Theory. Springer, Heidelberg (1998)
4. Smola, A.J., Schölkopf, B.: A tutorial on support vector regression. Statistics and Computing 14, 199–222 (2004)
5. Yoshida, H., Nappi, J.: Three-dimensional computer-aided diagnosis scheme for detection of colonic polyps. IEEE Trans. Med. Imaging 20, 1261–1274 (2001)
6. Metz, C.E.: ROC methodology in radiologic imaging. Investigative Radiology 21, 720–733 (1986)

Learning to Detect 3D Rectal Tubes in CT Colonography Using a Global Shape Model

Xiaoyun Yang, Gareth Beddoe, and Greg Slabaugh

Medicsight PLC, Kensington Centre,
66 Hammersmith Road, London, UK
xiaoyun.yang@medicsight.com

Abstract. The rectal tube (RT) is a common source of false positives (FPs) in computer-aided detection (CAD) systems for CT colonography. In this paper, we present a novel and robust bottom-up approach to detect the RT. Probabilistic models, trained using kernel density estimation (KDE) on simple low-level features, are employed to rank and select the most likely RT tube candidate on each axial slice. Then, a shape model, robustly estimated using Random Sample Consensus (RANSAC), infers the global RT path from the selected local detections. Our method is validated using a diverse database, including data from five hospitals. The experiments demonstrate a high detection rate of the RT path, and when tested in a CAD system, reduce 20.3% of the FPs with no loss of CAD sensitivity.

Keywords: rectal tube, RANSAC, CAD, CT colonography.

1 Introduction

The RT has a (potentially bent) cylindrical shape and includes a bulbous tip that often has a polyp-mimicking appearance. As such, the rectal tube is a common source of false positives generated by the CAD for CT Colonography (CTC) [1–4]. To improve the overall CAD performance, it is therefore desirable to have a robust and efficient way to identify the RT and remove its resulting FPs from the CAD marks presented to the reader. Some research has been proposed [2–4] to address this problem. Iordanescu et al. [2] developed an image segmentation based method that detects, via template matching, the air inside the RT in the first nine CT slices, tracks the tube, and performs segmentation using morphological operations. Suzuki et al. [3] employed a Massive Training Artificial Neural Network (MTANN) to distinguish between polyps and FPs due to the RT. Barbu et al. [4] detected part of the RT using Probabilistic Boosting Tree (PBT) and then applied dynamic programming to find the best RT segmentation from the detected parts. Both MTANN and PBT are supervised training discriminative techniques, however, their training heavily relies on the features of individual samples at each slice. None of the previous methods make use of a global shape model of the RT.

H. Yoshida et al. (Eds.): Virtual Colonoscopy and Abdominal Imaging 2010, LNCS 6668, pp. 53–59, 2011.

In this paper, we propose a novel and robust approach for the detection of the RT. We have two major contributions: (i) a probabilistic model trained on simple low-level features to detect 2D potential locations of the RT; (ii) a global 3D shape model estimated using RANSAC [5] that robustly infers the path of RT from local (and potentially outlier) detections. To our best knowledge, this is the first approach to combine simple low level detections with a global shape model for the robust detection of the RT. The method is computationally inexpensive and reliable. The results demonstrate a high detection rate using a diverse dataset, and in a CAD system, achieve a 20.3% reduction of false positives without any loss of sensitivity.

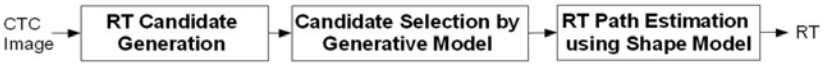

Fig. 1. Rectal Tube Detection Scheme

2 Method

2.1 Overview

We present a learning framework to combine probabilistic models for low level detection of air in the rectal tube with a global shape model of the RT path. The overview of the system is presented in Figure 1. We start with simple image processing, applied to each 2D axial slice, to detect air regions (RT candidates) within the body in the most caudad slices, starting at the anal verge and moving up the abdomen towards the lungs. For each RT candidate, three simple low level features are computed: the normalized spatial position x and y of the centroid and the size h of the region. A probabilistic model using kernel density estimation is trained for prone and supine data respectively and then used to rank the RT candidates. In each slice, the most probable tube candidate is selected and the others are discarded. From these 2D detections, RANSAC fits a global 3D global shape model representing the RT path. RANSAC is a robust statistical technique that can infer the real RT path even in the presence of strong outliers resulting from incorrect KDE predictions. We have two assumptions in this paper. First, the spatial distribution of RT within the body can be approximately described by a probabilistic model built from training data, which can be intuitively explained as the candidate can be more likely selected if its position is close to the mean position of training samples. Second, the RT is a possibly bent cylindrical structure placed on the bottom of body. With this knowledge, by seeking a quadratic path supported by maximum number of candidates, we can differentiate good candidates and bad ones selected by the probabilistic model. We can estimate RT path from good candidates. The details are discussed in the following subsections.

2.2 Probabilistic Models for 2D Candidate Detection of RT Regions

In this section we demonstrate how we generate local 2D RT candidates, and train a probabilistic model from simple low-level features. The generated model is then employed for selection of the most probable candidate on a given slice.

The air region in the RT can be identified on an axial image slice using standard image processing techniques. First, we apply simple thresholding using a threshold value of -750 HU. All the air pixels then belong to the background and all the remaining pixels are assigned to the foreground pixels; the largest foreground region will be the body. The air regions within the body region are then extracted using morphological operations. A 3D bounding box *rect* can be uniquely determined by enclosing all the extracted air regions.

Each candidate is represented by its centroid (C_x^i, C_y^i, C_z^i). Three low level features, (V_x^i, V_y^i, V_s^i), for each candidate are computed: the normalized spatial position (V_x^i) and (V_y^i) in the x and y direction, and the region size (V_s^i). The normalized spatial positions are determined as $V_x^i = (C_x^i - rect_{left}) / rect_{width}$, $V_y^i = (C_y^i - rect_{bottom}) / rect_{height}$, where $rect_{width}$ and $rect_{height}$ define the width and height of the bounding box, $rect_{left}$ and $rect_{bottom}$ represent the minimum bounding box coordinate in x and y, respectively.

In the training stage, each candidate is sorted by the distance from its centroid (C_x^i, C_y^i, C_z^i) to the annotated RT center point in the same slice. The candidate with the smallest distance is selected as training data to build a probabilistic model if the distance value is less than 6mm and the size is between 0.5 and 130mm2. If the size is too large, the candidate may correspond to or be combined with non-tube air regions. The selected feature data (V_x^i, V_y^i, V_s^i) is then used to build a probabilistic model with KDE. From the constructed KDE, the probability of a given feature vector can be estimated as

$$P(T|(V_x, V_y, V_s)) = \begin{cases} \frac{1}{C} \sum_{i=1}^{n} e^{-\frac{(V_x - V_x^i)^2}{2h_x^2}} \sum_{i=1}^{n} e^{-\frac{(V_y - V_y^i)^2}{2h_y^2}} & \text{if } V_s \in [0.5, 130]\text{mm}^2 \\ 0 & \text{otherwise} \end{cases} \quad (1)$$

where (V_x, V_y, V_s) is a given feature vector, (V_x^i, V_y^i, V_s^i) (i =1, .., N) is the ith example used for training. If V_s is too big or too small, a penalty is given and the probability is zero, and *C* is a normalization factor. The KDE model is generated from prone and supine data separately using Gaussian kernels with bandwidth 0.25 both in x and y direction.

In the testing stage, we apply the appropriate (prone or supine) probabilistic model to the candidate's feature vector. A probability can then be estimated for each RT candidate. The candidates are ranked by the estimated probability and only the one with the maximum value in each slice will be selected. Figure 2 (a) shows an example CT image, (b) the candidate regions and (c) most likely candidate selected by the KDE model.

The length of the RT within the body may vary depending upon how deeply the RT is inserted. We use the most 120mm caudad of CT slices as our processing range which are enough to cover the RT in our experimental data. The majority of RTs are located in the most 90mm caudad CT slices. Examples of RT detections are shown for two CT scans in Figure 3 for 120 consecutive slices in which the depth resolution is 1mm. In the figure, the red circles (inliers, usually corresponding to the RT) and blue dots (outliers, typically not corresponding to the RT) illustrate the selected candidate centroids, plotted separately, i.e., in the *xz* and *yz* planes. The tube is present in the patient for the most caudad slices with lower z value. Ideally, the KDE would predict all the air regions of the RT; however, KDE can wrongly pick up the candidates from other structures. Numerous outliers are shown in the figure, particularly near or past the end of the tube (approximately on slice $z = 60$ for the examples in the figure). In other cases the RT air regions may connect with colon air and the centroid can deviate away from true locations.

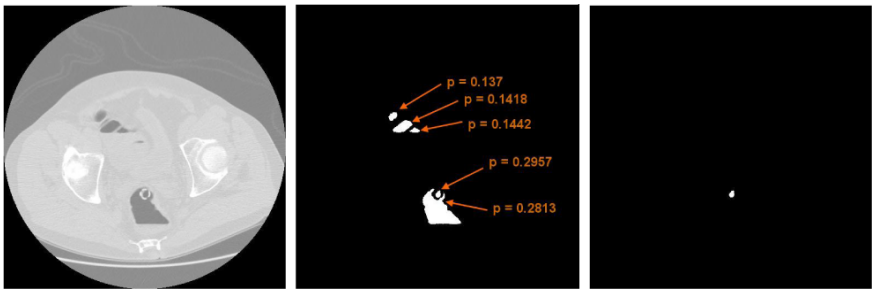

(a) (b) (c)

Fig. 2. Examples of the candidate selected by KDE. (a) the CT image, (b) the candidate regions, and (c) the region selected by KDE. This region corresponds to the air in the RT.

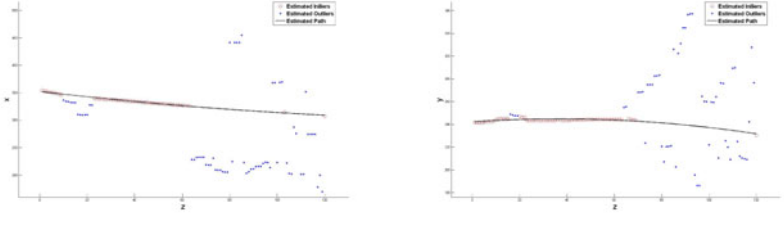

(a) (b)

Fig. 3. Examples of RANSAC fitting of two scans in the xz and yz planes

2.3 RT Path Estimation Using a Global Shape Model

In this section we describe how the underlying RT path is inferred from the RT candidate centroids selected in the previous step.

The RT is a cylindrical tube placed in the patient's colon, and once the colon is insufflated with room air and there is no force to twist the RT. The path of the RT can be approximated as a quadratic curve (which includes a straight line as a special case). While there may occasionally be some other air-filled structure or noise giving a quadratic path, the RT is easily identified as the longest path along a smooth and continuous quadratic curve starting at the bottom of the patient. To estimate the correct RT path, one must differentiate the outliers from the inliers that represent the true locations of the RT. From the inliers, we can infer the other 2D RT locations missed by KDE. With the prior model of the global shape information that the RT path is a quadratic curve and continuously appears in the most caudad slices, we use that as a criteria to seek a maximum set of inlier points that can fit the quadratic curve which can be resolved by RANSAC [5], as shown in Equation 2:

$$\hat{\theta} = \arg\max_{\theta} \sum_{i=1}^{N} f(e_i^2|\theta) \tag{2}$$

where

$$f(e_i^2|\theta) = \begin{cases} 1 & e_i^2 < \delta^2 \\ 0 & \text{otherwise} \end{cases} \tag{3}$$

where θ is the quadratic model to be estimated. e_i is the error or the distance between the data V_i and the estimated curve. δ is a threshold under the hypothesis that the error is generated by a true inlier contaminated with a Gaussian noise $P[e_i \leq \delta]$, where we expect the value of P is 0.95. A 3D space curve quadratic in z models the path as $[C_x(z), C_y(z), z]^T = [\theta_{0x} + \theta_{1x}z + \theta_{2x}z^2, \theta_{0y} + \theta_{1y}z + \theta_{2y}z^2, z]^T$, where the estimation of $[\theta_{0x}, \theta_{1x}, \theta_{2x}]$ and $[\theta_{0y}, \theta_{1y}, \theta_{2y}]$ is performed separately in the xz and yz planes respectively using RANSAC. In Figure 3, the blue dots represent the candidate locations classified as outliers (non-RT locations) and red circles represent the candidate locations classified as inliers (RT locations). The black line illustrates the inferred RT path from the inliers. Even in the presence of large outliers (non-RT locations) generated by KDE, the estimated RT path is quite reliable. After RANSAC fitting, given a slice number, we can predict the RT path location. RANSAC can be viewed as a method to achieve a robust regression to fit the global shape model to data containing significant outliers.

3 Results

Our experiment evaluates the RT tube detection for suppression of FPs in CAD. In this experiment, we built the probabilistic model from 40 CT scans data which are randomly selected and tested on 398 CT scans data set from 199 patients of prone and supine series. The data are collected from 5 institutions. CT images were generated using scanners from all the major manufacturers, including Siemens, GE, Philips, and Toshiba, with 4, 8, 16, 32, and 64 multi-slice configurations, KVp ranged from

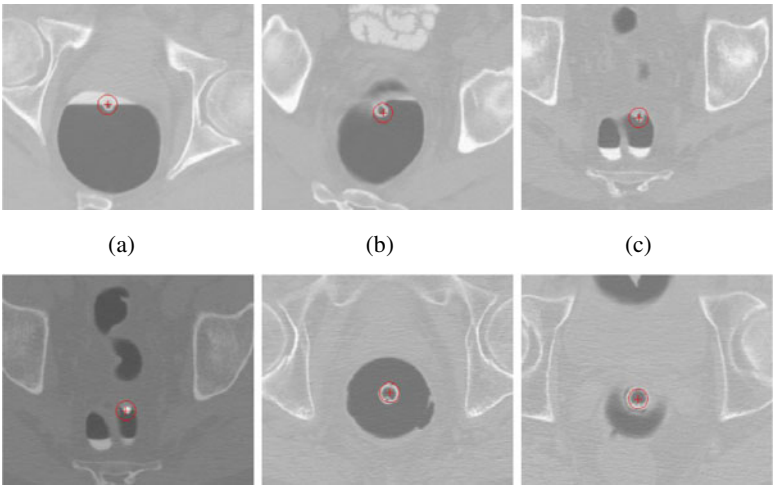

Fig. 4. Examples of detected RTs scanned from different hospitals

120-140, and exposure ranged from 29-500 mAs. All subjects were scanned within the last 10 years (1999 -2008) and roughly 80% were administered fluid and fecal tagging.

Any detection by CAD is removed as a FP if the in-plane distance between the center of the detected region and the center of the detected RT is less than 6mm. We did a one-dimensional grid search by varying the radius from 5mm10mm and 6mm can give us a maximum number of false positive reductions without losing any true positive CAD marks. The CAD produced 2186 false positive detections, of which 444 were removed by RT detection, from 5.49 to 4.37 per scan. Overall, this improved the CAD with a significant 20.3% FP reduction. None of the true positives detected by the CAD were missed due to RT detection, therefore CAD sensitivity was unaffected.

4 Discussion and Conclusion

In this paper, we presented a novel and robust learning approach for RT detection and removal of its resulting FPs in CAD. The approach starts from simple image processing operations and simple low-level 2D feature extraction for locally detected objects, which are then probabilistically ranked using KDE. Then, RANSAC robustly estimates the RT path from the most likely 2D candidates by fitting a 3D global shape model. Our RT detection method has shown a high performance for detecting the RT path and removing FPs in CAD. In future work, we plan to investigate robust approaches to detect the RT tip along the estimated path and its radius to help remove FPs more reliably.

References

1. Slabaugh, G., Yang, X., Ye, X., Boyes, R., Beddoe, G.: A Robust and Fast System for CTC Computer-Aided Detection of Colorectal Lesions. Algorithms 3(1), 21–43 (2010)
2. Iordanescu, G., Summers, R.M.: Reduction of false positives on the rectal tube in computer-aided detection for ct colonography. Medical Physics 31(10), 2855–2862 (2004)
3. Suzuki, K., Yoshida, H., Nppi, J., Dachman, A.: Massive-training artificial neural network (MTANN) for reduction of false positives in computer-aided detection of polyps: Suppression of rectal tubes. Medical Physics 33(10), 3821–3824 (2006)
4. Barbu, A., Bogoni, L., Comaniciu, D.: Hierarchical Part-Based Detection of 3D Flexible Tubes: Application to CT Colonoscopy. In: Larsen, R., Nielsen, M., Sporring, J. (eds.) MICCAI 2006, Part II. LNCS, vol. 4191, pp. 462–470. Springer, Heidelberg (2006)
5. Fischler, M.A., Bolles, R.C.: Random sample consensus: a paradigm for model fitting with applications to image analysis and automated cartography. Commun. ACM 24(6), 381–395 (1981)

Estimation of Necrosis Volumes in Focal Liver Lesions Based on Multi-phase Hepatic CT Images

June-Goo Lee[1,2], Wenli Cai[1], Anand Singh[1], and Hiroyuki Yoshida[1]

[1] Department of Radiology,
Massachusetts General Hospital and Harvard Medical School Boston,
Massachusetts 02114, USA
[2] Interdisciplinary Program in Radiation Applied Life Science,
Seoul National University College of Medicine, Seoul, South Korea
{Cai.Wenli,Yoshida.Hiro}@mgh.harvard.edu

Abstract. This study presents a computer-aided volumety (CAV) scheme that estimates the necrosis volumes in the focal liver lesions based on the multi-phase hepatic CT images for estimation of liver tumor burden. We developed a CAV scheme that consisted of the following three major steps: registration of multi-phase series based upon the portal-venous phase images, modeling of the concentration-time curve and thus estimattion of the arterial and portal-venous blood flow, and segmentation of the necrotic and tumorous tissues. Sixteen hepatocellular carcinoma cases were used for the evaluation of the CAV scheme. The total blood volume distribution of the liver tissue, tumor, and necrosis was computed in these datasets. The blood volumes for the liver tissue, tumor, and necrosis had 0.250±0.129, 0.171±0.073, and 0.054±0.045 ml/sec, respectively. The CAV scheme was shown to be potentially useful for efficient and accurate longitudinal measurement of liver tumor burdens in hepatic CT images.

Keywords: liver tumor, computer aided volumetry, multi-phase hepatic CT, dynamic analysis, treatment response measurement.

1 Introduction

Measurement of the volume of liver tumors, called liver tumor volumetry, is indispensable for assessing the growth of tumors and the effect of chemotherapy on the treatment of tumors [1]. However, some chemotherapeutic agents may give rise to an increase in tumor necrosis and thus cause enlargement of the total tumor size on imaging. Therefore, the assessment of only tumor volume has demonstrated the limitation that it may falsely over-estimate the tumor burden in tumors with increased necrosis volume. Thus, the measurements of the volumes of both necrotic and tumorous tissues may provide a more reliable solution to tumor burden assessment.

According to the tumor angiogenesis, the difference between necrotic and active tumorous tissues is the amount of blood supply. Necrotic tissues consiste of dead tumor cells and has very little blood supply, whereas tumorous tissues consist of live

H. Yoshida et al. (Eds.): Virtual Colonoscopy and Abdominal Imaging 2010, LNCS 6668, pp. 60–67, 2011.

cells, have rich vascular structures, and receive significant amount of blood supply. Thus, the differentiation of necrotic from tumorous tissues can be based upon the volume of blood flow, which can be estimated by the analysis of CT perfusion or multi-phase CT images. However, manual segmentation of necrosis includes multiple series and is labor-intensive due to its dynamic nature.

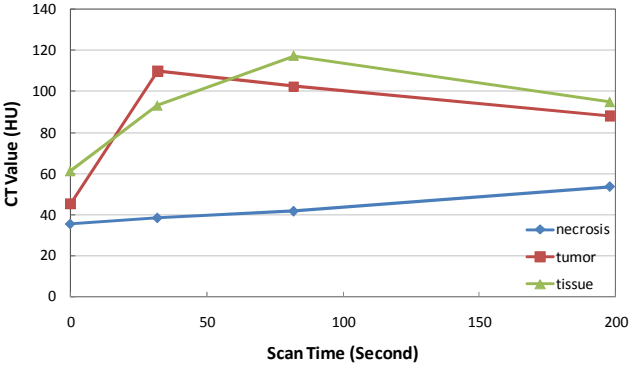

Fig. 1. Concentration-time curves in hepatic CT scans can be applied to identify different types of tissues in the liver

Thus, our purpose in this study was to develop a computer-aided volumety (CAV) scheme that estimates necrosis volume in the focal liver lesions based on the multi-phase hepatic CT images, with the potential use for estimation of liver tumor burden.

2 Methods

The classification of necrotic and tumorous tissue is based upon the blood flow, which can be represented by the concentration-time curve of the iodine contrast agent. A concentration-time curve reflects the change of the contrast flow over time and thus can be used to estimate the blood volume by use of the area under the concentration-time curve [2]. Furthermore, the shape of concentration-time curve is unique for necrotic and tumorous tissues, as illustrated in Fig.1.

Our CAV scheme for necrotic and tumorous tissues has been developed based on the multi-phase hepatic CT images, including plain phase, arterial phase, portal-venous phase, and delayed phase. Plain phase serves as the baseline, and the differences between other phases and the plain phase are used to estimate the blood flow. The CAV scheme consists of the following three major steps:

1) Registration of multi-phase series of hepatic CT images to the reference series, i.e., the portal-venous phase series;
2) Modeling of the concentration-time curve and thus estimation of the arterial and portal-venous blood flow;
3) Segmentation of the necrotic and tumorous tissue.

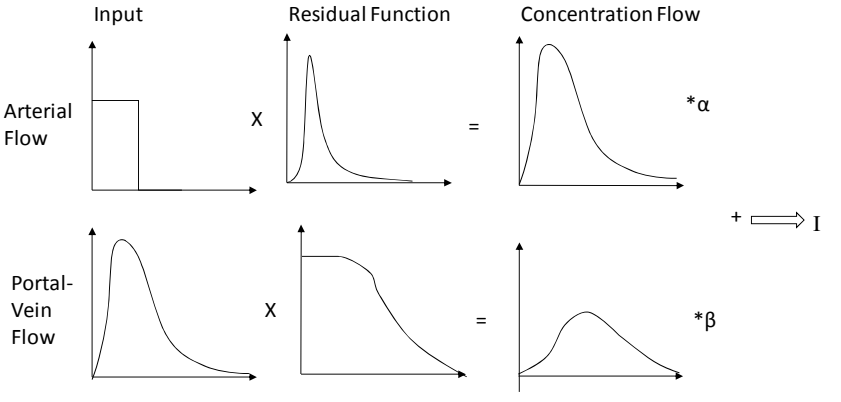

Fig. 2. Concentration-time curve in hepatic CT scans is a linear sum of arterial flow and portal-venous flow

2.1 Registration

Considering the non-rigid nature of the liver, we apply the deformable registration after the initial registration is performed by use of a 3D affine non-rigid transform [3]. Because the healthy liver tissue and the tumor tissue are largely visible in the portal-venous phase, which is often used for liver and liver tumor segmentation, the portal-venous phase was selected as the reference series of images for the registration process.

2.2 Blood-Flow Estimation

It is known that the liver tissue can be modeled as a one-compartmental model with dual inputs: arterial and portal-venous inputs [4]. As illustrated in Fig 2, the concentration flow of contrast at each unit in the liver is essentially composed of a linear sum from the arterial flow and the portal-venous flow:

$$I(t) = \alpha I_A(t) + \beta I_{PV}(t) \ , \tag{1}$$

where I_A and I_{PV} are the arterial flow and portal-vein concentration flow, respectively, and the weighting coefficients are $0 \le \alpha \le 1$, $0 \le \beta \le 1$, and $0 \le \alpha + \beta \le 1$.

The concentration flow of a contrast agent can be represented by an exponential decay function called *residual function*. By convolution of a residual function with an arterial or portal-venous input function, the concentration-time curve can be estimated by

$$I(t) = S(t) \times R(t) \ , \tag{2}$$

where S is the input function of the contrast agent, and R is the residual function.

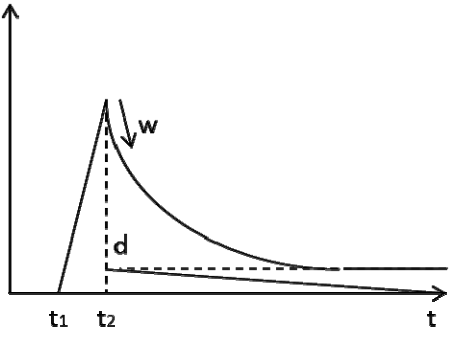

Fig. 3. Residual function formed by 4 parameters

Compared to CT perfusion, multi-phase MDCT has much coarse temporal resolution, i.e., it contents only the following four time points:

T_0 – plain imaging time point that is used as the baseline time point;
T_A – time point for arterial phase imaging;
T_{PV} – time point for portal-venous phase imaging; and
T_D – time point for delay phase imaging.

The concentration-time curve is estimated based on the differences of arterial, portal-venous, and delay phases by use of the plain phase as baseline. The concentration of contrast in the blood flow can be expressed by an exponential-decay function, which is represented by four parameters as illustrated in Figure 3:

t_1 – arriving time;
t_2 – starting time of decay;
w – wash-out rate, governed by e^{-wt};
d – damping term, reducing the concentration with a constant speed.

Thus, the insufficient sampling time-points in the four-phase hepatic CT images causes the uncertainty in the concentration-time curve and the inaccuracy in the blood-flow estimation. In this study, therefore, we developed an optimal curve fitting method to reconstruct a concentration-time curve from four time-point sampling data.

- **Construction of optimal arterial / portal-venous concentration-time curves**

The flow volume is estimated by the area under the concentration-time curve, which is a linear sum of arterial and portal-venous concentration-time curves as shown equation (1). An accurate flow volume relies on a continuous concentration-time curve that approximates the four sampling points with minimal errors.

For this optimization purpose, we construct the optimal arterial and portal-venous concentration-time curve based upon the minimal root mean square error (RMSE) at sampling points between the estimated concentration-time curve and real sampling data. The optimization of a continuous concentration-time curve consists of the following three steps:

(1) Modeling of a group of residual functions based upon a set of four parameters of residual function [5].
(2) Building of a group of concentration-time curves by convolution of each residual function with an input function.
(3) Calculation of the RMSE for each estimated concentration-time curve.

The curve with minimal RMSE is selected as the optimal concentration-time curve.

- **Finding of optimal arterial concentration-time curves**

The arterial concentration-time curve, $I_A(t)$, is constructed by use of sampling points at the aorta. The input function of the aorta, $S_A(t)$, is a pulse function, which can be estimated based on the injection protocol of contrast agent. See the top row in Fig 2.

- **Finding of optimal portal-venous concentration-time curves**

The portal-venous concentration-time curve, $I_{PV}(t)$, is constructed by use of the sampling points at the portal-vein phase. We take arterial flow, $I_A(t)$, as the input function of the portal-vein input function, $S_{PV}(t)$, and construct the optimal portal-venous concentration-time curve. See the bottom row in Fig 2.

- **Estimation of the flow volume at each voxel**

After the construction of continuous arterial and portal-venous concentration-time curves, we estimate the weighting coefficients α and β in equation (1) for the estimation of contributions of the arterial and portal-venous flows at each voxel. This results in two flow volumes: the arterial flow volume, F_A, and the portal-venous flow volume, F_{PV}:

$$F_A = \int_{T_0}^{T_D} \alpha I_A(t)dt,\ F_{PV} = \int_{T_0}^{T_D} \beta I_{PV}(t)dt\ . \tag{3}$$

Thus, we can calculate the hepatic perfusion index (HPI), which is defined as the ratio of hepatic arterial to total liver blood flow, as follows:

$$HPI = F_A\ /\ (F_A + F_{PV})\ . \tag{4}$$

2.3 Segmentation

Liver tumors are firstly segmented in the portal-venous images by use of the dynamic-thresholding level set (DTLS) method [6]. The seed regions in the potential liver tumors in the segmented liver are identified based on CT values and minimum volume mass. In the second step, new seeds are initialized within the above segmented tumor regions by use of the estimated flow volume, and they are evolved in the blood flow map to delineate the boundary of the necrosis by use of the DTLS method. The resulting boundaries are used for calculation of the volume of the necrotic and tumorous tissues.

3 Results

Sixteen hepatocellular carcinoma (HCC) cases were used for the evaluation of our CAV scheme. These cases were obtained by multi-detector CT scanning with the following parameters: 2.5mm collimation, 1.25–2.5-mm reconstruction interval, 175-mA tube current, and 140-kVp tube voltage. All cases were imaged by injection of an intra-venous contrast agent (ISOVUE; GE Healthcare, Milwaukee, WI). All of the HCCs were confirmed by biopsy and identified in the portal venous phase images, and they were subjected to the CAV scheme for measurement of the necrosis and tumor volumes.

Fig. 4 demonstrats an example of an arterial flow image, a portal-venous flow image, and an HPI image, compared to a portal-venous phase image. It is difficult to determine whether the lesion is neurotic based on the portal-venous image in Figure 4(d). On the other hand, the arterial flow and portal-venous flow images clearly show that the regions are nicrotic.

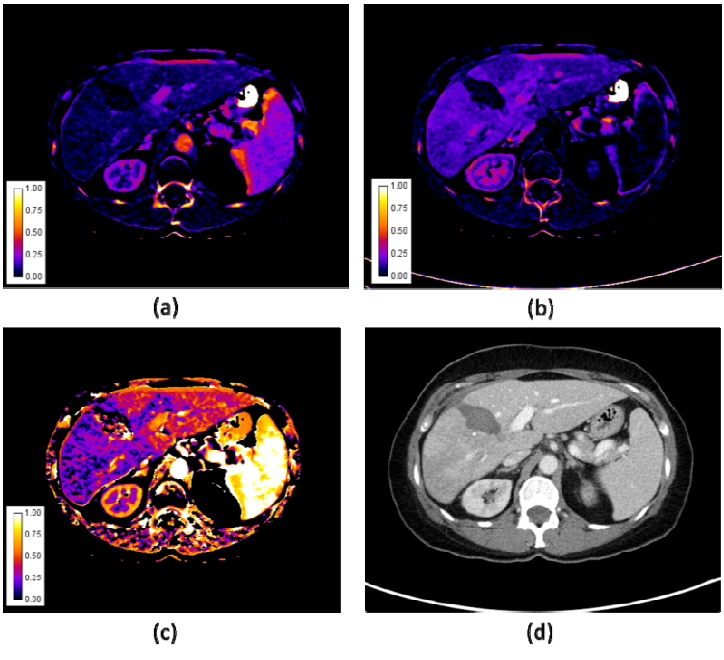

Fig. 4. Example of perfusion parameters calculated by the proposed method. (a) Arterial flow image. (b) Portal venous flow image. (c) HPI image. (d) Portal-venous image.

Fig. 5. The blood volume distribution of liver tissue, tumor, and necrosis

In each case, the most representative slice was chosen, and three regions of interest for liver tissue, tumor, and necrosis were extracted. Fig. 5 shows the blood volume distribution in the three types of tissues. The necrosis had a significantly lower blood flow than the other two tissue types.

Fig. 6 demonstrates an example of tumor and necrotic regions segmented by use of our CAV scheme. One can observe that necrotic and tumor tissues are clearly identified and thus segmented. The ratios of necrosis / tumor volumes were 108.16 / 812.68 (0.13) and 209.69 / 679.46 (0.31) for the lesions in the left and right lobes, respectively.

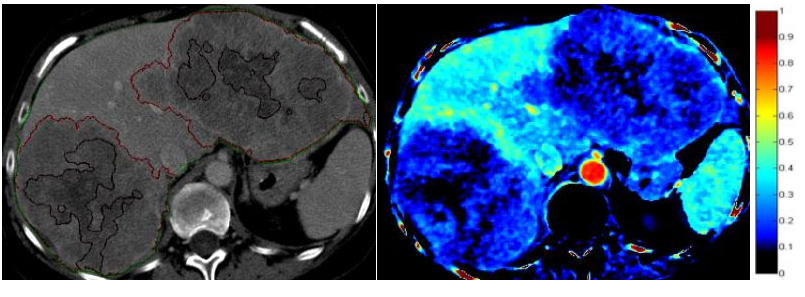

(a) (b)

Fig. 6. (a) Portal-venous phase image of an HCC patient. The red contours delineate the tumor regions, whereas the blue contours delineate the necrotic regions. (b) Color map of the normalized blood flow volume.

4 Conclusion

We have developed a CAV scheme for measurement of necrotic and tumorous tissue voluems in hepatic multi-phase CT images. Our preliminary results showed that our

scheme was effective in estimating the volume of the necrotic and tumorous tissues in the focal liver lesions. Thus, the scheme is potentially useful for efficient and accurate longitudinal measurement of liver tumor burdens in hepatic CT images.

References

1. Vauthey, J.N., Dixon, E., Abdalla, E.K., Helton, W.S., Pawlik, T.M., Taouli, B., Brouquet, A., Adams, R.B.: Pretreatment assessment of hepatocellular carcinoma: expert consensus statement. HPB (Oxford) 12, 289–299 (2010)
2. Pandharipande, P.V., Krinsky, G.A., Rusinek, H., Lee, V.S.: Perfusion imaging of the liver: current challenges and future goals. Radiology 234, 661–673 (2005)
3. Ibanez, Schroeder, Ng, Cates, The ITK Software Guide. Kitware Inc. (2005)
4. Materne, R., Van Beers, B.E., Smith, A.M., Leconte, I., Jamart, J., Dehoux, J.P., Keyeux, A., Horsmans, Y.: Non-invasive quantification of liver perfusion with dynamic computed tomography and a dual-input one-compartmental model. Clin. Sci. (Lond) 99, 517–525 (2000)
5. Axel, L.: Tissue mean transit time from dynamic computed tomography by a simple deconvolution technique. Invest. Radiol. 18, 94–99 (1983)
6. Cai, W., Holalkere, N., Harris, G., Sahani, D., Yoshida, H.: Dynamic-threshold level set method for volumetry of porcine kidney in CT images: in-vivo and ex-vivo assessment of the accuracy of volume measurement. Acad. Radiol. 14, 890–896 (2007)

Detection of the Invasion of Bladder Tumor into Adjacent Wall Based on Textural Features Extracted from MRI Images

Zhide Wu, Zhengxing Shi, Guopeng Zhang, and Hongbing Lu*

Department of Biomedical Engineering,
Fourth Military Medical University, Xi'an,
Shaanxi 710032, China
{luhb,zhanggp}@fmmu.edu.cn,
xiaozhi_wu001@yahoo.com.cn, jsf39@163.com

Abstract. The invasion depth of a bladder tumor is of great importance for tumor staging and treatment planning. Considering that MRI bladder images could provide natural contrast between the urine and bladder wall, some texture features have been extracted from MRI images in our previous study, demonstrating a statistically significant difference between tumor tissues and wall tissues. In this study, a classification and labeling scheme has been proposed for the detection of the invasion depth of bladder tumors, based on these selected features, such as mean, standard deviation, uniformity, covariance, and contrast. Experimental results using patients' MRI datasets show the feasibility of the proposed scheme for labeling of bladder tumors, indicating its potential for noninvasive detection of bladder tumors and their stage.

Keywords: CAD (computer-aided detection), bladder tumor, MR images, texture features, support vector machine.

1 Introduction

Bladder tumor is a severe common tumor that threatens human health all over the world. *Cancer facts & figures 2009* indicates that bladder tumor is the 4th most common malignancy in men and the 8th in women. It accounts for 7% of all malignancies in men and 3% in women in all of America [1]. In China, bladder tumor is the 8th most common malignancy in men, and the incidence is climbing rapidly in some cities [2].

Compared with a basic diagnosis based on patient symptoms and physical examination, optical cystoscopy is currently the gold standard for examination of the entire bladder [3]. Radiological imaging is often performed in conjunction with cystoscopy for the purpose of evaluating malignant invasion into adjacent organs. The radiographic reading and interpretation process depends greatly on the experience of

* Corresponding author.

H. Yoshida et al. (Eds.): Virtual Colonoscopy and Abdominal Imaging 2010, LNCS 6668, pp. 68–75, 2011.

radiologists. This is because the gray values of image pixels inside carcinomatous tissues differ only subtly from those of the surrounding tissues, in addition to the partial volume effect. Therefore, it is quite difficult to acquire essential information such as the depth of invasion (an index for the stage of bladder tumors) directly from radiologic images, which is of great importance for accurate and early diagnosis, as well as for surgical treatment planning.

Some studies have shown a superior accuracy of MRI, especially in the local staging of bladder tumors and in the prediction of wall and perivesical infiltration, because of its high contrast between the bladder wall and the urine. Our previous study has indicated that some textural features extracted from MRI images have statistical differences between bladder tumors and bladder wall tissues [4]. Based on this observation, in this study, a classification and labeling scheme has been proposed for the detection of the invasion depth of bladder tumors, which consists of feature extraction, feature selection, classification, and evaluation.

2 Materials and Method

2.1 Subjects and MRI Datasets

22 patients with confirmed bladder tumors collected from October 2008 to April 2009 in TangDu Hospital were included in this study. All of the patients had urothelial carcinoma confirmed by postoperative pathologic biopsy. Prior to the examination, all patients were required to drink enough water so that the bladders were distended sufficiently. In this study, all MRI examinations were performed with a 3.0 Tesla scanner (MR-Signa EXCITE HD, GE) using a sequence of T2-SSFSE (T2- single-shot fast spin-echo), with scanning parameters of TR/TE: 2117.6/78.0ms, thickness: 3.0mm, and spacing of layers: 0.5mm. The total duration of the examination for each patient was approximately one hour, including the positioning of the patient.

2.2 Overview of the Detection Scheme

The whole scheme mainly consists of three steps: 1) Manual selection of ROIs (region of interest, including carcinomatous tissue and its surrounding bladder wall), 2) gray-level scaling and textural feature extraction from selected ROIs, and 3) classification and labeling with an SVM classifier by use of calculated features. Finally, to evaluate the detection performance, the classification results were compared with pathologic results from postoperative biopsy.

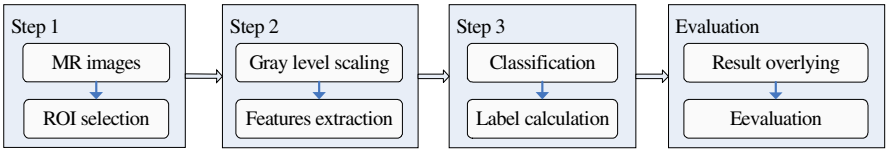

Fig. 1. The scheme proposed for the detection of invasion depth of bladder tumor

2.3 Selection of Textural Features

Due to the complicated structure of bladder tumors and their surrounding tissues, it is quite difficult to segment them out of the whole image automatically. To get a thorough and accurate analysis of textural features of bladder tumors and wall tissues, all ROIs were first selected from the MRI images manually by three experienced radiologists. These ROIs consist of either carcinomatous tissue or normal wall tissue and are referred to basic ROIs (bROIs) in this study, with which the difference on textural features between carcinomatous tissue and wall tissue could be analyzed statistically. Based on these bROIs, textural features with significant difference were filtered out in our previous study, and part of them has been used in this study as the input of the classifier for the detection of invasion depth. In addition, bROIs were used as the gold standard during the evaluation of classification results.

In previous experiments, a total of 42 features were extracted from every bROI. Among them, 33 features showed a significant difference between two groups [4], i.e., bROIs of carcinomatous tissues and those of normal wall tissues. Generally, for texture analysis, a region of a certain size should be required for computing textural features accurately. However, a larger region used for texture calculation would reduce the accuracy of following segmentation and labeling of tumor boundaries in this study. Among the 33 textural features, the extraction of features such as line_likeness, GLCM (gray-level occurrence matrix)-induced and GLGCM (gray-level gradient occurrence matrix)-induced features usually require a larger region for calculation and would be inappropriate for use in this study. Therefore, 6 features, i.e., mean, uniformity, standard deviation, norm of vector (auto-covariance coefficient), coarseness and contrast, were chosen from 33 significant features and referred as the feature vector, as shown in Table 1.

Table 1. Features used for classification

Feature	Computation formula
Mean	$m=\frac{1}{n}\sum_{(x,y)\in R}\left[f(x,y)\right]$
Uniformity	$u=\sum_{i=1}^{k}\left[p(l_i)\right]^2$ (*)
Standard deviation	$s=\sqrt{\frac{1}{n-1}\sum_{i=1}^{n}\left[f_i(x,y)-m)\right]^2}$, $\sigma=\sqrt{\frac{1}{n}\sum_{i=1}^{n}(f_i(x,y)-m)^2}$
Norm of Vector (auto-covariance coefficient)	$A(\Delta m,\Delta n)=\frac{1}{Count_{(\Delta m,\Delta n)}}\cdot\sum_{x=0}^{M-1-\Delta m}\sum_{y=0}^{N-1-\Delta n}[f_{in}(x,y)-\bar{f}_{in}]\times[f_{in}(x+\Delta m,y+\Delta n)-\bar{f}_{in}]$ $\gamma(\Delta m,\Delta n)=\frac{A(\Delta m,\Delta n)}{A(0,0)}$, $\mathrm{NOV}=\sqrt{\sum_{\Delta m=0,\Delta n=0}^{n}\gamma(\Delta m,\Delta n)^2}$ (**)

Table 1. (*Continued*)

Coarseness	$A_k(x,y)=\sum_{i=x-2^{k-1}}^{x+2^{k+1}-1}\sum_{i=y-2^{k-1}}^{y+2^{k+1}-1} f(i,j)/2^{2k}$ k=1, 2,..., n $E_{k,h}(x,y)=\left\|A_k(x+2^{k-1},y)-A_k(x-2^{k-1},y)\right\|$ $E_{k,v}(x,y)=\left\|A_k(x+2^{k-1},x)-A_k(x-2^{k-1},x)\right\|$ $E_k=E_{\max}=\max(E_{1,h},E_{1,v},\cdots,E_{L,h},E_{L,v})$ $S_{best}(x,y)=2^k,\quad Fcrs=\frac{1}{m\times n}\sum_i^m\sum_j^n S_{best}(i,j)$ (***)
Contrast	$\alpha_4=\mu_4/\sigma_4,\quad Fcon=\sigma/(\alpha_4)^n$ (****)

* p is the probability density function of the region gray level. ** indicates the formula used for the computation of the auto-covariance coefficient, *** the formula for coarseness, and **** the formula for contrast.

2.4 Extraction of Textural Features

In order to alleviate the impact of noise and an inhomogeneous magnetic field existing in MRI images, and to calculate the features more accurately, a calculation method for textural features based on 2x2 cells for each ROI was proposed, as shown below:

1. Divide the ROI into sequential 2x2 cells (Fig. 2), with irregular edge cells being filled or rejected.
2. For each cell, extend it into four different vertical/horizontal directions and get four 4x4 square regions, as shown in Fig.2 (a)-(d).
3. Calculate textural features of each 4x4 square region, respectively. Then 4 vectors are acquired for each cell and fed into the classifier.

Each 4x4 region was labeled as 1 if the ROI belonged to the carcinomatous group, or as -1 if the ROI belonged to the bladder wall group. With datasets from 21 patients (one dataset was ignored in this study because of the tiny size of the tumor), a total of 10860 feature vectors for 4x4 square regions were extracted from all bROIs. Among them, 7854 were from carcinomatous tissues (labeled as 1) and 3006 from normal wall tissues (labeled as -1). All of these vectors were used to train and test the SVM classifier.

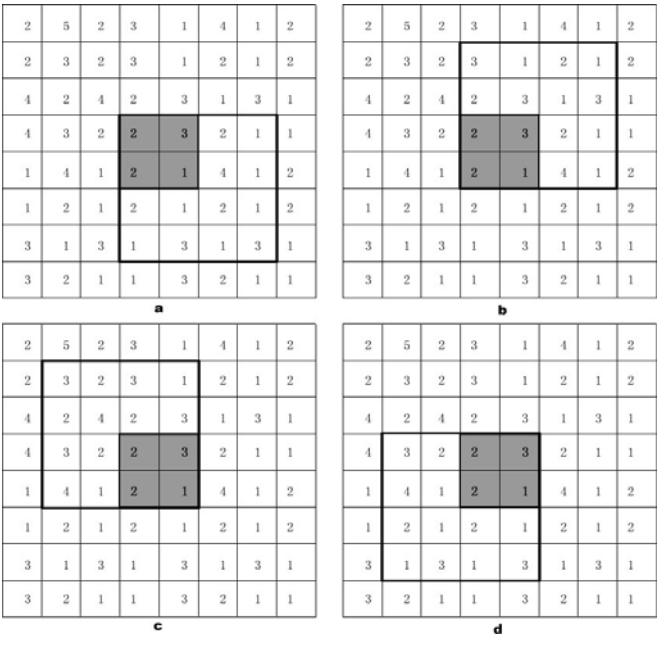

Fig. 2. A 2x2 cell and its four neighboring 4x4 square regions. The shadow region represents the cell, and four neighboring 4x4 square regions are marked with a, b, c and d, respectively.

2.5 Training and Evaluation of the SVM Classifier

In our study, we chose SVM as the classifier because of its better generalization capability. Since the number of feature vectors extracted from each patient was dramatically different (ranging from 35 to 2894 for different patients), vectors from each patient were randomly divided into ten sub-groups, which were marked from 1 to 10. Then all the vectors with the same marker, but from different patients were put into one group, and all 10860 vectors from bROIs were divided into 10 groups. For each test, the classifier was trained by 9 groups and tested by the remaining one. Then the test group was changed, and the process was repeated for 10 times. The performance of the classifier was set as the average of the specificity rate of ten times.

Different kernel functions and cost functions of an SVM classifier may result in different classification results. In this study, the classical radial basis function (RBF) was used as the kernel function. Considering the bias of data (the ratio between the number of tumor vectors-7854- and that of normal vectors-3006- is 2.61), a weighted cost function was used to mitigate this deficiency. One parameter in RBF and 2 parameters in the cost function formed a 3D parameter grid, and the exhaustion method was used to search the optimal parameter combination for the SVM classifier.

2.6 Tissue Labeling for the Detection of Invasion Depth

For evaluating the performance of the proposed scheme, 56 ROIs that include both carcinomatous tissue and surrounding wall tissue were extracted manually from 56 images selected from patients' datasets. Unlike bROIs, which were used to filter out feature vectors and to train the classifier, these 56 ROIs were used to test the classification accuracy and to detect tumor boundaries and therefore are referred as combined ROIs (cROIs). With the outlined cROIs, a total of 13006 feature vectors were extracted and fed into the SVM classifier for tissue labeling and detection of the invasion depth.

With the trained SVM, all of the 13006 vectors were classified into two groups, i.e., carcinomatous tissue or normal tissue. Then each cell in cROIs was labeled with a value according to the labeling rule shown in Table 2, decided upon by the classification results of its four neighboring 4x4 square regions. Because the boundary of each cROI is irregular, the labeled value could be 3, -3, 1, or -1.

To highlight the labeling result, we assigned a pseudo-color for each labeled value, as shown in Fig 3. The larger the labeled value is, the more likely it is that the cell is a carcinomatous tissue, and the brighter the color is. Fig 4 shows some results of tissue labeling on patients' images, which demonstrate the invasion of bladder tumors into the adjacent wall. Considering that the growing direction of a bladder tumor is from the inner to the outer border of the bladder wall and usually is perpendicular to the wall, some single cells near the wall borders that were not perpendicular to the wall were removed for getting a clearer demonstration of the invasion depth.

Table 2. The labeling rule for each cell

Identifier	NO. of tumor square regions	NO. of normal square regions	labeled value	Remark
1	4	0	4	If the labeled value: =0, possibly be the boundary >0, possibly may be a tumor cell <0, possibly be a normal wall cell
2	3	1	2	
3	2	2	0	
4	1	3	-2	
5	0	4	-4	
6	3	0	3	
7	2	1	1	
8	1	2	-1	
9	0	3	-3	
10	2	0	2	
11	1	1	0	
12	0	2	-2	
13	1	0	1	
14	0	1	-1	

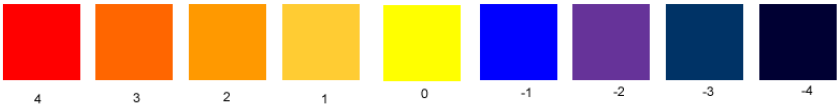

Fig. 3. Relationship between the label value and its assigned pseudo-color

3 Results

The SVM classification with test groups acquired from bROIs demonstrates that the classification accuracy where 6 textural features are used is 75.4%. Pathologically, the bladder wall is composed of 4 layers, which are from inner to outer, the urothelium, connective tissue, muscle tissue, and adipose tissue. In this experiment, the wall is

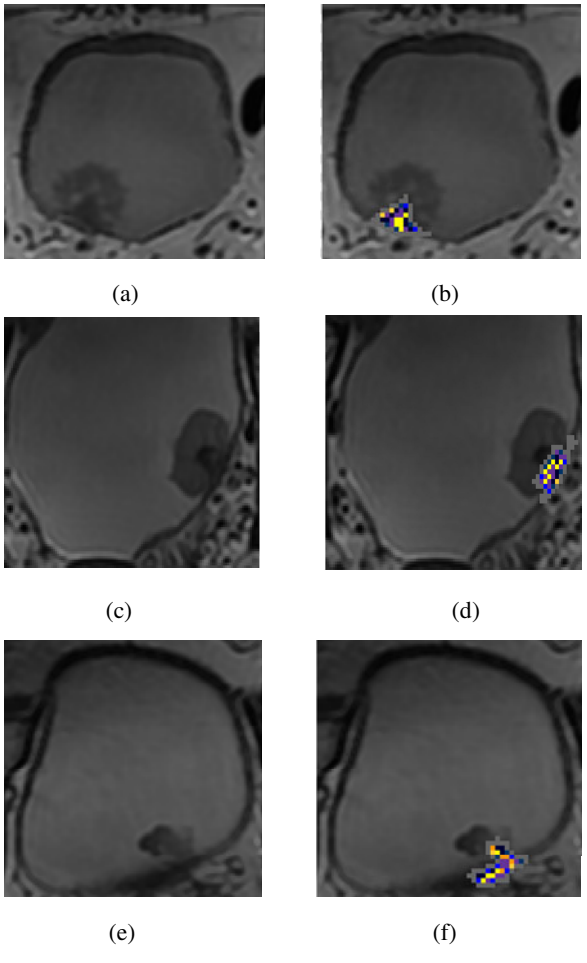

Fig. 4. Some results of tissue labeling. (a), (c) and (e) are MR bladder images acquired from different patients. (b), (d), and (f) are labeling results acquired by the proposed scheme.

simply described as having two parts, i.e., the mucosa layer (contain urothelium and connective tissue) and the muscularis layer (contain muscle tissue and adipose tissue). For diagnosis of bladder tumor, whether the tumor invades the muscularis layer is a very important index for tumor staging. Fig.4 shows the labeling results for three cROIs from different patients after SVM classification and their corresponding pseudo-color visualization.

Fig. 4(a) shows a slice of MR bladder images for a patient with a bladder neoplasm. The labeling result shown in Fig. 4(b) indicates that almost all of the pixels near the boundary are classified as normal wall tissue, suggesting that the tumor has not yet invaded the muscularis layer (T1 stage). Compared with Fig. 4(b), the labeling result shown in Fig. 4(d) indicates that some pixels inside the wall region are classified as possible tumor cells, suggesting that the tumor seems to partly enter into the wall (T2 stage). However, the result shown in Fig.4(f) demonstrates a highlighted chain of tumor cells inside the bladder wall, indicating the invasion of the tumor into the bladder wall and adjacent organs (T3 stage) .

Compared with postoperative biopsy results, 42 out of the 56 images are correct, indicating that the specificity of the proposed detection scheme is about 75%. Although currently the specificity is not high enough, it is most important that the proposed scheme could probably provide a way for the detection of invasion depth, which is difficult to be acquired by standard method, especially before a surgical operation.

4 Conclusions

As the gold standard for the diagnosis of bladder cancer, conventional optical cystoscopy can detect the number, shape, and position of primary tumors, perform biopsy, and remove a cancerous or suspected area. However, it is difficult for it to evaluate malignant invasion of cancer into adjacent organs. Based on textural features of bladder MRI images, this study proposes a detection scheme that can help physicians to get an intuitive view of tumor invasion into the bladder wall. Preliminary results indicate that this might be a novel and promising tool for tumor detection with virtual cystoscopy. However, intensive and extensive investigation should be performed on feature selection, the calculation method for textural features, optimization of the classifier, and the extension of the patient dataset, for further improvement the accuracy of detection.

References

1. American Cancer Society: Cancer Facts and Figures 2009, 4–10. American Cancer Society, Atlanta(GA) (2009)
2. Editorial committee of China urology disease diagnosis and treatment guidelines: China urology disease diagnosis and treatment guidelines, pp. 90–104. Chinese Urological Association (2007)
3. Kocakoc, E., Kiris, A., Orhan, I., et al.: Detection of Bladder Tumors with 3-Dimensional Sonography and Virtual Sonographic Cystoscopy. J. Ultrasound Med. 27, 45–53 (2008)
4. Shi, Z.H.: Computer aided diagnosis for bladder cancer based on MRI, pp. 36–58. The fourth military medical university, Xian, China (2010)

Detecting Bladder Abnormalities Based on Inter-layer Intensity Curve for Virtual Cystoscopy

Fanghua Liu[1], Chaijie Duan[1], Kehong Yuan[1],
Zhengrong Liang[2], and Shanglian Bao[3]

[1] Research Center for Biomedical Engineering of Graduate School at Shenzhen, Tsinghua University, Shenzhen 518055, China
[2] Department of Radiology, State University of New York, Stony Brook, NY 11794, USA
[3] Beijing Key Lab of Medical Physics and Engineering, Peking University, Beijing 100871, China
liufh09@mails.tsinghua.edu.cn,
{duan.chaijie,yuankh}@sz.tsinghua.edu.cn,
jerome@mil.sunysb.edu, bao@pku.edu.cn

Abstract. This paper presents a level set based method for bladder abnormality detection on T1-weighted MR images. First, the bladder wall is segmented by using a coupled level set framework, in which the inner and outer borders of the bladder wall are extracted by two level set functions. Then, the middle layer of the bladder wall is founded and represented by a new level set function. Finally, the new level set function divides the bladder wall into several layers. The inter-layer intensity of all voxels in each layer is sorted in ascending order to generate the inter-layer intensity curve. The results prove the effectiveness of inter-layer intensity curve in indicating the emerging of the bladder abnormalities.

Keywords: bladder wall, abnormalities detection, inter-layer intensity curve.

1 Introduction

According to American Cancer Society, bladder cancer is the fifth leading cause of cancer deaths in the United States. The chance of a man having bladder cancer is about 1 in 27 while for women it is 1 in 85. And the 5-year relative survival rate (The 5-year survival rate refers to the percentage of patients who live at least 5 years after their cancer is found. 5-year *relative* survival rate assumes that patients will die of other causes, too.) of patients whose cancer is found in the third or fourth stage is below 50% [1]. Early diagnosis of bladder abnormalities is crucial for effective treatment of bladder carcinoma. In addition, bladder cancer is reported to have high recurrence rate after resection of the tumors (as high as 80% [2]). Therefore, a method is needed which facilitates early detection of bladder abnormalities and follow up.

Fiberoptic cystoscopy which can accurately evaluate the bladder abnormalities is now the most popular diagnosis method. However, this method is invasive, expensive, time-consuming and brings great pain to the patients as well as with a risk of 5% to

H. Yoshida et al. (Eds.): Virtual Colonoscopy and Abdominal Imaging 2010, LNCS 6668, pp. 76–83, 2011.

10% rate of urinary track infection. Nowadays, the development of the medical imaging technologies provides a potential alternative for the fiberoptic cystoscopy: virtual cystoscopy (VCys). Most VCys is based on computed tomography (CT) technology and magnetic resonance imaging (MRI). Comparing with the CT imaging, the MR imaging is preferred due to its structural, functional and pathological information for diagnosing and staging the tumor growth and the noninvasive operation [3, 4]. Forthermore, the T1-weighted MR images provide better contrast for the bladder wall which is crucial for bladder abnormality detection. According to some reports, at early stages of the bladder carcinoma, flat and/or small tumors less than 5 mm are difficult to detect and, therefore, deserve more attention [5]. Conventional characteristic features on the bladder wall, like curvedness and shape index, vary significantly from voxel to voxel [6]. Some preliminary results show that the bladder wall thickness is a possible choice for the abnormalities detection [7-9].

This paper proposes an inter-layer intensity curve (ILIC) to detect the abnormalities possibly emerging on the bladder wall. This work is based on our prior work [10] which delineates the inner and outer borders of bladder wall by use of a coupled level set framework. The segmented bladder wall is further divided into several layers which are approximately parallel to the bladder wall borders. A preliminary survey shows that the ILIC has potential discriminability for differentiating the layers with bladder abnormalities from the normal ones.

2 Methods

The pipeline of generating the ILIC is shown in Fig. 1, including three steps: bladder wall segmentation, bladder wall layer generation and ILIC generation.

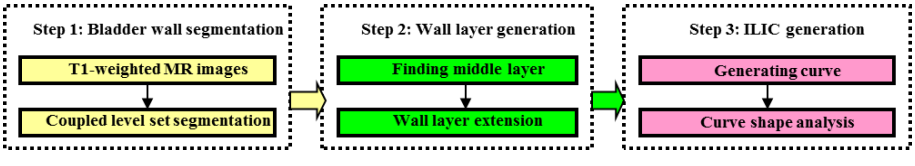

Fig. 1. Pipeline of generating the ILIC

2.1 Bladder Wall Segmentation

A coupled level set framework is used for bladder wall segmentation [10]. The inner and outer borders of the bladder wall in T1-weighted MR images are segmented by two level set functions: inner level set function (ILSF) ϕ_1 and outer level set function (OLSF) ϕ_2 respectively. The inner border is first pre-segmented by modifying the well known Chan-Vese (C-V) LS model [11] which segments an image into piecewise-constant or piecewise-smooth patches. The modified C-V model defines a narrowband of the zero level set surface (ZLSS) instead of the whole image as the region of interest (ROI). Then, OLSF evolves several steps outwards from the

ILSF to estimate the location of the outer border. A regional adaptive clustering algorithm (RACA) is proposed to evolve the ILSF and OLSF iteratively and obtain the final results. The inner and outer borders are represented by the ZLSSs of ILSF and OLSF respectively. Fig. 2 gives an example of the segmentation result.

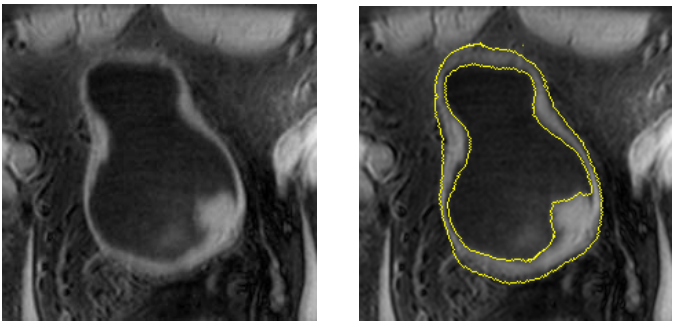

(a) (b)

Fig. 2. (a) A typical T1-weighted MR image slice of a bladder. (b) Segmentation result of the same slice as in (a). Two yellow curves in (b) are the segmented inner and outer borders represented by ZLSSs of ILSF and OLSF.

2.2 Bladder Wall Layer Generation

A middle layer is constructed. This layer is supposed to be inside the bladder wall and consists of all voxels $\mathbf{x}$ which meet the three conditions at the same time

$$\phi_1(\mathbf{x}) < 0, \phi_2(\mathbf{x}) > 0 \text{ and } \left|\phi_1(\mathbf{x})\right| = \left|\phi_2(\mathbf{x})\right| \quad (1)$$

where $\phi_1(\mathbf{x}), \phi_2(\mathbf{x})$ are the ILSF and OLSF respectively. The equations above mean the middle layer is between the inner and outer borders and has the same distance to these two borders. Then with the middle layer as the ZLSS, the middle level set function (MLSF) $\phi_m(\mathbf{x})$ is constructed. $\phi_1(\mathbf{x}), \phi_2(\mathbf{x})$ and $\phi_m(\mathbf{x})$ are represented by the signed distance function which has the form of $\phi(\mathbf{x}) = \pm d$, where d is the nearest distance from $\mathbf{x}$ to the ZLSS. The positive or negative value means that the voxel $\mathbf{x}$ is inside or outside the ZLSS.

2.3 ILIC Generation

This section can be divided into several steps as follows:

Step 1. Definition of the ROI

To eliminate redundant information and reduce computing time, a ROI shall be defined within which the method in this paper is applied. Since the middle layer has been placed by the above steps, $\phi_m(\mathbf{x})$ now roughly divides the voxels x of bladder

wall into two groups with $\phi_m(\mathbf{x}) > 0$ and $\phi_m(\mathbf{x}) \le 0$ respectively. By defining a constant $D > 0$, a ROI is constructed as a band-shaped area around the bladder wall with all voxels $\mathbf{x}$ inside the ROI having $-D < \phi_m(\mathbf{x}) < D$. In this work, we set $D = 10$ which guarantees the ROI has similar shape to and covers the entire region of the bladder wall.

Step 2. Dividing ROI into different layers according to the MLSF

Based on the values of $\phi_m(\mathbf{x})$, 19 layers which are approximately parallel to the bladder wall borders are generated in the ROI. Then the layers are indexed from 1 to 19 according to the order of their corresponding $\phi_m(\mathbf{x})$ values from small to large. Since the segmentation is performed on 3D datasets, all the layers are in fact 3D surfaces in the ROI. An example is shown in Fig. 3. Fig.3 (a) and (b) are images from a volunteer and a patient. The white curves inside the bladder wall are the middle layers in the displayed slices.

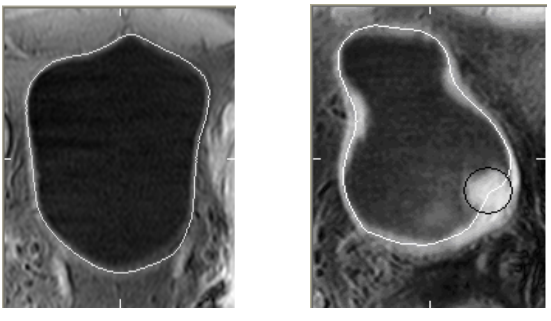

(a) (b)

Fig. 3. An example to compare. (a) the bladder wall image of a volunteer. (b) the bladder wall image of a patient. The white curves are the middle layers in the slices respectively. The black circle in (b) indicates an abnormal protrusion.

Step 3. Generation of the ILIC

After all voxels inside the ROI are assigned to different layers, for each layer, the ILIC is generated by firstly recording the intensity value of voxels belonging to this layer to a one dimensional array, and then sorting the elements in this array in ascending order. The ILIC curve is delineated in the coordinates with array index and array element value as the horizontal axis and the vertical axis.

According to our experiment, the ILIC plotted without sorting presents as disorderly as Fig.4 (a) and offers no useful information for bladder wall differentiating. However, if we first sort the elements then delineate the ILIC, the result curve shows very smooth as Fig.4 (b), and from which features that reflect the intensity distribution of the voxels along the layer are captured. These features will be

used in our following bladder wall differentiating work. For example, the long plateau stage in the middle part of the curve represents that most of the voxels in the specific layer share the same intensity value. The sorted curve is invariant to image geometry transformation such as rotation, and thus makes the bladder walls of different shapes comparable.

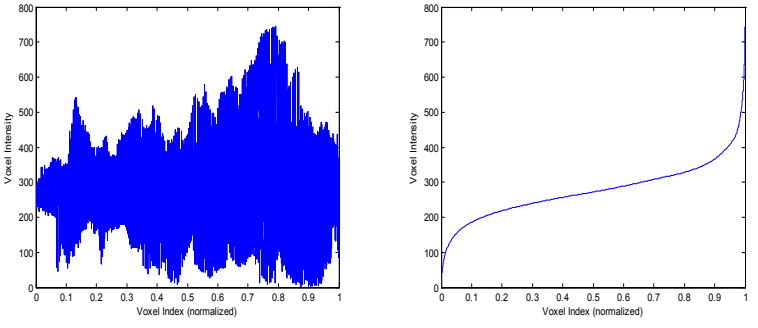

(a) (b)

Fig. 4. A contrast between different ILICs with different methods. (a) The ILIC of the 1st layer in the normal bladder wall plotted without sorting. (b) The ILIC of the same layer with (a) with sorting method.

3 Result and Discussion

Six T1-weighted MR datasets are used to test the above method. A preliminary survey shows that, in normal bladder wall, the voxels in the same layer share a similar intensity since the bladder wall has a relatively uniform intensity distribution. On the other hand, in patient's bladder wall, the intensity distribution of the voxels in the layers which are near the inner border is not so uniform since there usually exists a protuberance in this area. The result shows that ILIC actually expresses the distinction between the layers with bladder abnormalities and the normal ones.

Fig.5 gives an example of normal and abnormal bladder walls and their respective ILIC impressions:

According to Fig.5 (a), which is a slice from the volunteer's data, the intensity of the normal bladder wall has a relative uniform distribution. Correspondingly in Fig.5 (b), the ILIC has the characters as follows: (1) It is basically smooth and fluctuates slightly ignoring the two terminals resulting from the noise and inhomogeneity of the MR images. (2) There is only one plateau (The voxel index approximately ranges from 0.1 to 0.7 in the horizontal coordinates in Figure.5 (b)) on the curve which represents the major intensity range of the bladder wall.

However in Fig.5 (c), which is a slice from the patient's data, since there is an abnormal protrusion in the bladder, in the 17th layer near the inner border, the intensity of the voxels in the abnormality is much higher than that of the other parts. Correspondingly in Fig. 5 (d), the ILIC has following characters: It has two plateau

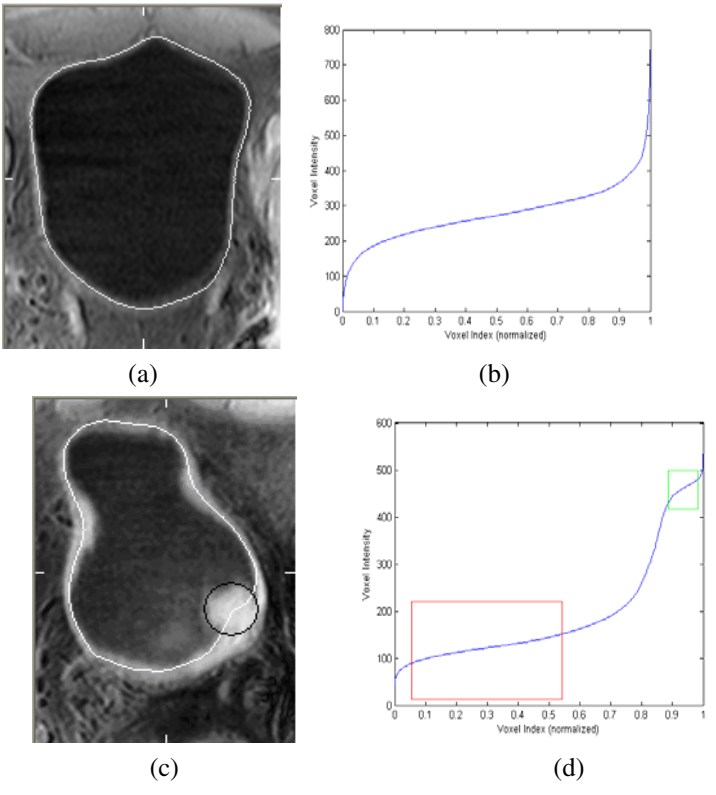

Fig. 5. An example shows the ILICs of the typical layers from volunteer's and patient's bladder images. (a) is the volunteer's bladder image and the white line in the bladder wall marks the middle layer. (b) shows the ILIC of the 17th layer in the bladder wall of (a). (c) is a patient's bladder image in which we can see a protuberance in the wall and the white line in the bladder wall marks the middle layer. (d) shows the ILIC of the 17th layer in the bladder wall of (c). In (b) and (d), since the numbers of sampling voxels are different, we normalize the horizontal axis to make the two ILICs more comparable.

phases: one is the middle part of the curve marked by a red box and the other is at the back end of the curve marked by a green box (The existing reason for the red and green boxes in the figure is to point out the plateau part more clearly for the readers). The first plateau phase represents the intensity range of the lumen which takes up the majority in all and have lower intensity value. The latter one represents the abnormal protrusion which is the minority. And there is an obvious disparity between their lengths.

Thus , we can see from Fig.5 that the distinction between the abnormal bladder wall and normal one can be reflected by their ILICs respectively.

Fig. 6 shows the three typical ILICs shapes. Fig.6 (a) is the ILIC from the layers close to the 1st layer. Since different tissues contribute different intensity value, there is no major plateau phase on this curve. Fig. 6 (b) and (c) are the ILICs of normal

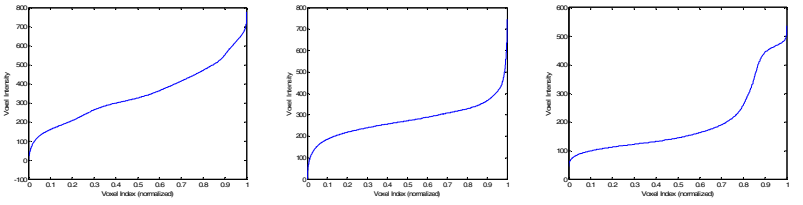

(a) (b) (c)

Fig. 6. The typical ILIC shapes. (a) The typical ILIC with no major plateau phase. (b) The typical ILIC with one major plateau phase. (c) The typical ILIC with two major plateau phases.

bladder wall layer and the layer covering abnormal region which have one and two major plateau phases respectively. We explored all six datasets with three volunteers and three patients. The results show that the two plateau phases ILICs appear and only appear in the patients' datasets while one plateau phase ILICs appear in all datasets.

Based on the truth above, the ILICs have the potential discriminability to differentiate the layers with abnormality from others. Comparing with many other features especially these based on the voxel by voxel geometrical properties, the ILIC gives the intensity information along the bladder wall layer by layer which is immune to local noise and takes the intensity inhomogeneity into account. While the ILICs of layers close to the middle layer have similar curve shape, the ones far from the middle layer (expanding outside the bladder wall) have relative complex expression. The current work only qualitatively analyzes the differences. In our future work, more quantitative features from the ILICs such as the placement of the plateau phases and the smoothness of the plateau phases will be extracted and different classifiers will be designed.

4 Conclusion

In this study, we propose a method based on the ILIC to detect the abnormalities possibly emerging on the bladder wall. In the method, the inner and outer borders of bladder wall can be given based on the bladder wall segmentation results. The segmented bladder wall is further divided into several layers which are approximately parallel to the bladder wall borders. Then the voxels in each layer is sorted in ascending order and the ILIC to the layer is plotted. The performance of the ILIC is not sensitive to the segmentation result. The segmentation result is used to initialize the MLSF, and the ILICs generated from MLSF cover the whole bladder wall. Thus, at least one layer goes through the abnormality whose ILIC gives the clue for abnormality detection. We applied this method to 6 T1-weighted MR datasets including volunteers' and patients', and find that there exist obvious distinctions between the ILIC of the normal layer and that of the layer with abnormalities. All the 6 datasets are from clinical imaging, and evaluated by the doctors.

So far, at least one ILIC has two major plateau phases in each patient's dataset which means the emerging of the abnormality. Based on the primary idea, more sophisticated analysis is under investigation. In the future work, more quantitative

features will be extracted, based on which a series of classifiers can be constructed for the tumor detection. While the two plateau phases can be found in all patients' dataset, the specificity of the ILICs is under investigation. More effort has been devoting to recruit new clinical datasets to evaluate the viability and stability of our potential method.

Acknowledgments. This work was supported by the China Postdoctoral Science Foundation funded project (No.20090460353).

References

1. Overview: Bladder Cancer, from American Cancer Society web site (2010), http://www.cancer.org (retrieved June 8, 2010)
2. Lamm, D.L., Torti, F.M.: Comparing Object Encodings. In: Abadi, M., Ito, T. (eds.): Theoretical Aspects of Computer Software. "Bladder cancer". A Cancer Journal for Clinicians, 46, 93-112 (1996)
3. Liang, Z., Chen, D., Button, T., Li, H., Huang, W.: Feasibility studies on extracting bladder wall from MR images for virtual cystoscopy. Proc. International Society of Magnetic Resonance in Medicine 3, 2204 (1999)
4. Chen, D., Li, B., Huang, W., Liang, Z.: A multi-scan MRI-based virtual cystoscopy. Proc. SPIE Medical Imaging 3978, 146–152 (2000)
5. Lämmle, M., Beer, A., Settles, M., Hannig, C., Schwaibold, H., Drews, C.: Reliability of MR imaging-based virtual cystoscopy in the diagnosis of cancer of the urinary bladder. American Journal of Roentgenology 178, 1483–1488 (2002)
6. Li, L., Wang, Z., Harrington, D., Huang, W., Liang, Z.: A mixture-based computed aided detection system for virtual cystoscopy. In: Proc. International Society of Magnetic Resonance in Medicine, vol. 1, p. 146 (2003)
7. Jaume, S., Ferrant, M., Macq, B., Hoyte, L., Fielding, J.R., Schreyer, A., Kikinis, R., Warfield, S.K.: Tumor detection in the bladder wall with a measurement of abnormal thickness in CT scans. IEEE Transactions on Biomedical Engineering 50(3), 383–390 (2003)
8. Fielding, J.R., Hoyte, L., Okon, S.A., Schreyer, A., Lee, J., Zou, K.H., Warfield, S., Richie, J.P., Loughlin, K.R., O'Leary, M.P., Doyle, C.J., Kikinis, R.: Tumor detection by virtual cystoscopy with color mapping of bladder wall thickness. The Journal of Urology 167, 559–562 (2002)
9. Zhu, H., Duan, C., Jiang, R., Li, L., Fan, Y., Yu, X., Zeng, W., Gu, X., Liang, Z.: Computer-aided detection of bladder tumors based on the thickness mapping of bladder wall in MR images. In: Proc. SPIE Medical Imaging 2010, in CD-ROM (2010)
10. Duan, C., Liang, Z., Bao, S., Zhu, H., Wang, S., Zhang, G., Chen, J.J., Lu, H.: A Coupled Level Set Framework for Bladder Wall Segmentation with Application to MR Cystography. IEEE Trans. on Medical Imaging 29(3), 903–915 (2010)
11. Chan, T., Vese, L.: Active contours without edges. IEEE Transactions on Image Processing 10(2), 266–277 (2001)

Computer-Assisted Diagnosis for Quantitative Image-Based Analysis of Crohn's Disease in CT Enterography

Janne Näppi[1], June-Goo Lee[1], Joel G. Fletcher[2], and Hiroyuki Yoshida[1]

[1] Department of Radiology,
Massachusetts General Hospital and Harvard Medical School,
25 New Chardon Street, Suite 400C, Boston,
Massachusetts 02114, USA
jnappi@partners.org, yoshida.hiro@mgh.harvard.edu
[2] Department of Radiology, Mayo Clinic,
200 First Street SW, Rochester, MN 55905, USA

Abstract. Crohn's disease is an inflammatory disease that can cause a wide variety of symptoms and is increasing in prevalence. We developed a computer-assisted diagnosis (CADx) scheme for quantitative image-based analysis of Crohn's disease in CT enterography (CTE). The CADx scheme extracts regions of interest automatically from CTE data, analyzes the small bowel automatically by use of mural features, and uses a support vector machine to predict the presence of active Crohn's disease. For pilot evaluation, two radiologists diagnosed the CTE data of 54 patients with known or suspected Crohn's disease. An unblinded gastroenterologist established the truth about the patients. The CADx scheme was then trained with the CTE data of 46 patients where the radiologists agreed on their diagnosis, and it was tested with the 8 difficult cases where the radiologists disagreed on their diagnosis. A bootstrapping analysis of the per-patient performance of the CADx scheme in predicting the presence of active Crohn's disease yielded an area under receiver-operating characteristic (ROC) curve of 0.92±0.05. The result indicates that the CADx scheme could provide a useful decision-making tool for CTE.

Keywords: Crohn's disease, CAD, computer-assisted diagnosis, CT enterography.

1 Introduction

Crohn's disease (CDS) is a chronic inflammatory bowel disease that can cause a wide variety of symptoms, such as abdominal pain, diarrhea, vomiting, weight loss, arthritis, skin rash, inflammation of the eye, tiredness, or lack of concentration. CDS affects over half a million individuals in the United States and Canada, and it is increasing in prevalence [1]. The available treatment options can provide symptomatic relief, but these treatments are costly and have potential side-effects.

H. Yoshida et al. (Eds.): Virtual Colonoscopy and Abdominal Imaging 2010, LNCS 6668, pp. 84–90, 2011.

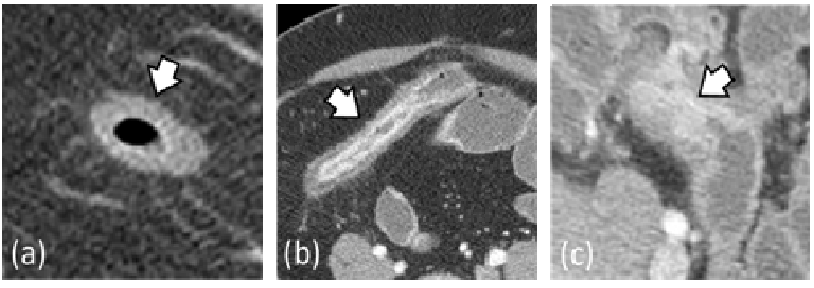

Fig. 1. Examples of regions with Crohn's disease (arrows). (a) The lumen may be filled partially by air. (b) Neutral rather than positive contrast is used for visualizing mural inflammation. (c) Luminal narrowing marked by mural hyper-enhancement.

The development of new treatments and the assessment of therapy response to CDS are limited partially because of the currently adopted measures for characterizing inflammatory activity that are largely subjective [2]. Thus, there is an urgent need for diagnostic tools for providing objective and reproducible measurements of inflammatory activity to stratify Crohn's patients using global and objective markers of disease and to guide therapeutic options.

CT enterography (CTE) is a new imaging technique that has a high accuracy for detecting CDS-related small bowel inflammation and its penetrating complications [3]. However, several critical barriers remain for the use of CTE, such as large inter-observer variability and lack of reproducible measurements. Despite that CDS affects small bowel in up to 80% of patients, there are no validated scoring systems for reflecting the extent and severity of CDS and its associated inflammation in the small bowel.

The purpose of this study was to develop a computer-assisted diagnosis (CADx) scheme for facilitating semi-automated image-based quantitative and reproducible measurements of CDS activity. A pilot evaluation was performed to assess the performance of the CADx scheme in the differentiation of Crohn's and normal patients in CTE.

2 Method

2.1 Clinical CT Enterography Cases

A total of 54 patients with known or suspected CDS were included in the study. The patients were prepared with a large volume of ingested neutral enteric contrast and intravenous contrast for enhancing the bowel wall, and they were imaged by use of high-resolution multi-detector CT scanners. Two gastrointestinal radiologists diagnosed the CTE images for radiological signs and for the presence of active CDS. Figure 1 shows three examples of regions with active Crohn's disease.

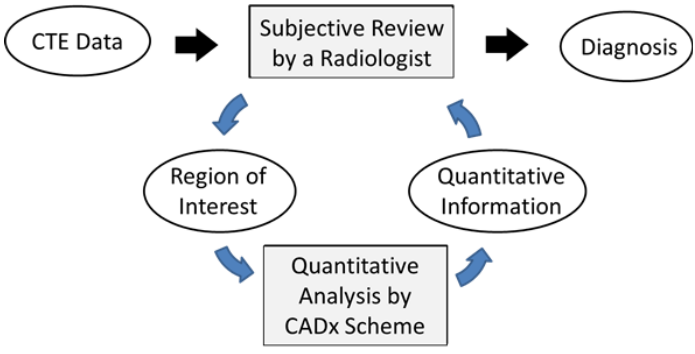

Fig. 2. Overview of the semi-automated reading scheme for diagnosing Crohn's disease

To provide a reference standard, an unblinded gastroenterologist who did not otherwise participate in the study established the truth regarding the presence of Crohn's disease by use of the CTE data, ileocolonoscopy, MR enteroscopy data, C-reactive protein, and Crohn's disease activity index of the patients.

2.2 CADx Scheme

The CADx scheme that was developed for this study is designed to be used as a semi-automated reading tool for assessing regions of interest in CTE data for the presence of active CDS (Figure 2). After a radiologist has indicated a region of interest by use of a graphical user interface by clicking of a region with a mouse or multi-touch interface, the CADx scheme identifies the region of small bowel within the region automatically, calculates image-based mural features from the extracted region automatically, and displays quantitative information and a summary index that predicts the likelihood of active bowel inflammation in the region. Figure 3 shows an overview of the design of the CADx scheme.

2.2.1 Extraction of Small Bowel Lumen and Surface Regions

The input CTE data are interpolated into isotropic resolution by use of axial interpolation. Image noise is reduced by use of Gaussian smoothing. After a user has identified a region of interest, the bowel surface is extracted automatically as the surface of the region of bowel lumen. To identify the bowel lumen, an adaptive region-growing method is used. First, seed points are identified in the bowel lumen as voxels x_s that satisfy the primary seed test of $\mu_C - \sigma_C < x_s < \mu_C + \sigma_C$ or $x_s < \mu_A$ with $\|\nabla x_s\| < t_A$, where μ_C and σ_C^2 are the expected mean intensity and variance of the orally administered enteric lumen contrast agent, and μ_A and t_A are the expected mean intensity of lumen air and the expected maximum value of the magnitude of three-dimensional gradient of the bowel lumen, respectively.

However, because of the wide variety of cases (Figure 1), the primary seed test may fail to establish a suitable number of seeds for some cases. If this happens, the

seed points are recomputed by use of the secondary seed test of $\mu_C - \sigma_C < x_s < \mu_C + \sigma_C$ or $x_s < \mu_A$. The secondary test identifies cases with noisy images. If the secondary test also fails to establish a suitable number of seeds, the seed points are recomputed by use of the tertiary seed test of $x_0 < x_s < \max\{\mu_C + \sigma_C, x_0 + \sigma_C\}$ or $x_s < \mu_A$, where x_0 is the center point of the region of interest. This test identifies cases with uncommon intensity distribution.

After the seed points have been determined, region-growing is performed to extract the region of bowel lumen, R. The surface of R defines the outer surface of the small bowel wall.

2.2.2 Extraction of Mural Features

To calculate mural features, the wall region of the small bowel is sampled by calculation of the 3D normals of the bowel surface at each surface point x' of R, by $\nabla x'$. Next, a sample line is projected through the wall into the direction of the normal (Figure 4a,b). Because of the limited nominal CT image resolution, the resolution of the sample line is enhanced by fitting of a polynomial $f(s) = c_1 + c_2 s + c_3 s^2 + c_4 s^3$ to the line sample ((Figure 4c). Given the observed samples $\{(s_i, v_i)\}_{i=1}^{N}$ along the sample line, where s_i is the relative position of a sample point and v_i the observed intensity at that point, the coefficients of the polynomial can be computed by solving the linear system [4]:

$$\left(\sum_{k=1}^{N} s_k^6\right) c_4 + \left(\sum_{k=1}^{N} s_k^5\right) c_3 + \left(\sum_{k=1}^{N} s_k^4\right) c_2 + \left(\sum_{k=1}^{N} s_k^3\right) c_1 = \sum_{k=1}^{N} v_k\, s_k^3,$$

$$\left(\sum_{k=1}^{N} s_k^5\right) c_4 + \left(\sum_{k=1}^{N} s_k^4\right) c_3 + \left(\sum_{k=1}^{N} s_k^3\right) c_2 + \left(\sum_{k=1}^{N} s_k^2\right) c_1 = \sum_{k=1}^{N} v_k\, s_k^2,$$

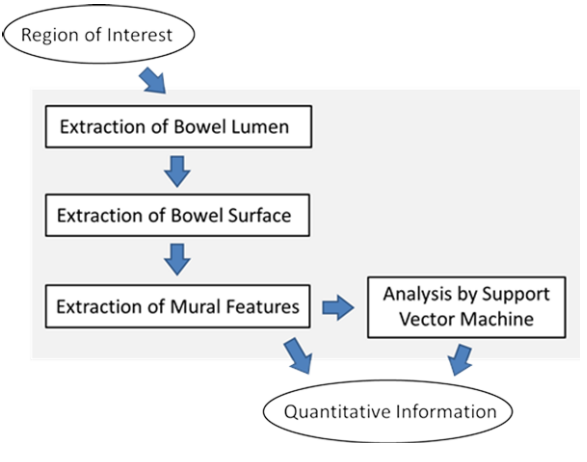

Fig. 3. Overview of the CADx methods

$$\left(\sum_{k=1}^{N} s_k^4\right)c_4 + \left(\sum_{k=1}^{N} s_k^3\right)c_3 + \left(\sum_{k=1}^{N} s_k^2\right)c_2 + \left(\sum_{k=1}^{N} s_k\right)c_1 = \sum_{k=1}^{N} v_k s_k,$$

$$\left(\sum_{k=1}^{N} s_k^3\right)c_4 + \left(\sum_{k=1}^{N} s_k^2\right)c_3 + \left(\sum_{k=1}^{N} s_k\right)c_2 + Nc_1 = \sum_{k=1}^{N} v_k.$$

Three mural features are calculated from the enhanced line samples. The peak enhancement feature, f_{max}, is the highest intensity along the line sample. The wall-thickness feature is calculated as $F_W = f_e - f_b$, where $f_b = \max\{\xi\,;\, \xi < \xi_{max}, f(\xi) < \mu_C\}$ and $f_e = min\{\xi\,;\, \xi > \xi_{max}, f(\xi) < \mu_C\}$, and ξ_{max} is the location of f_{max} within the sample. The hyper-enhancement feature is calculated by $F_H = 100\% \times (f_{max} - max\{f_b, f_e\})/f_{max}$.

To characterize the distribution of these features in a region of interest, the mean, standard deviation, skewness, kurtosis, and maximum statistics are calculated over all line samples for each feature.

2.2.3 Analysis by Support Vector Machine

A support vector machine (SVM) is used to predict the presence of Crohn's disease based upon the calculated features. An SVM separates different categories of data by use of a hyper-plane $\langle w, \Phi(x)\rangle + b = 0$. The hyperplane corresponds to a decision function $d(x) = sign(\langle w, \Phi(x)\rangle + b)$, where Φ is an implicit mapping of the input data to a high-dimensional feature space defined by a kernel function, i.e., a function returning the inner product $\langle \Phi(x), \Phi(x')\rangle$ between the images of two data points x and x' in the feature space [5]. The learning of the data takes place in the feature space, and the data points only appear inside dot products with other points [6].

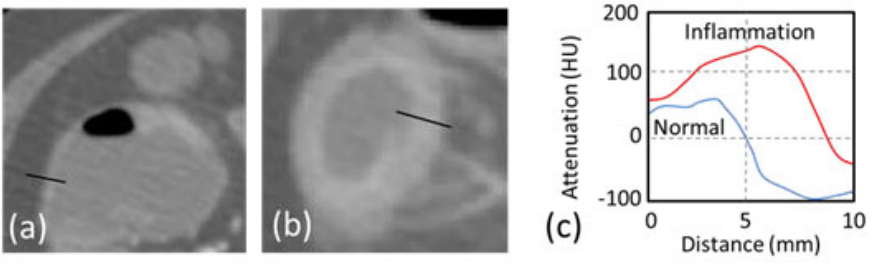

Fig. 4. (a) Visualization of one of the line samples (black line) through normal bowel wall. The samples are calculated in 3-D. (b) Visualization of a sample through mural inflammation. (c) Polynomial fits of the line samples.

2.3 Evaluation Methodology

The per-patient performance of the CADx scheme was characterized in terms of the area under receiver operating characteristic curve (A_z) [7]. The A_z values range from 0 to 1, where a high A_z value indicates high classification performance in differentiating active Crohn's patients and normal patients, whereas an A_z value of 0.50 (or lower) indicates low classification performance.

Based upon the training data, four least correlated features were chosen for the training of the SVM. The internal parameters of the SVM were optimized with the training data by use of leave-one-out evaluation, after which the performance of the SVM was tested with separate testing data. The variance of training performance was estimated by use of bootstrapping.

3 Results

The radiologists agreed on their diagnosis of the presence of Crohn's disease in 46 CTE cases. According to the reference standard, these cases included 21 normal patients and 25 patients with active Crohn's disease. Bootstrapping analysis of the per-patient performance of the CADx scheme in predicting Crohn's disease with these cases yielded an A_z value of 0.78±0.09.

The radiologists disagreed on their diagnosis in 8 CTE cases. According to the reference standard, there were 2 normal patients and 6 patients with active Crohn's disease in these cases. To test the performance of the CADx scheme with these difficult cases, the CADx scheme was trained with the CTE data of the 46 patients where the radiologists had agreed. When the CADx scheme was tested with the 8 difficult CTE cases, the A_z value of the per-patient performance for predicting the presence of Crohn's disease was 0.92±0.05.

We also compared the quantitative measurements of individual features that were made from the regions of interest with the CADx scheme. The measurements indicate that the average value of the wall-thickness feature is significantly higher with Crohn's disease (4.0±0.9 mm) than with normal patients (2.9z±0.9 mm). Also the values of the hyper-enhancement feature tend to be higher with Crohn's patients (3.9%±0.9%) than with normal patients (3.3%±0.8%). However, the values of the peak enhancement feature did not differ significantly between the patients.

4 Conclusion

Our preliminary results of this pilot study indicate that the CADx scheme that was developed in this study can yield high performance in the differentiation of active Crohn's patients from normal patients. The CADx scheme can also provide other clinically meaningful diagnostic information about the small bowel. Therefore, the CADx scheme can provide a useful tool for a more objective diagnosis of Crohn's patients than current subjective indices.

References

1. Loftus, E.J.: Clinical epidemiology of inflammatory bowel disease: incidence, prevalence, and environmental influences. Gastroenterology 126, 1504–1517 (2004)
2. D' Haens, G.R., Fedorak, R., Lemann, M., et al.: Endpoints for clinical trials evaluating disease modification and structural damage in adults with Crohn's disease. Inflamm. Bowel. Dis. 15, 1599–1604 (2009)
3. Bodily, K.D., Fletcher, J.G., Solem, C.A., et al.: Crohn disease: mural attenuation and thickness at contrast-enhanced CT enterography - correlation with endoscopic and histologic findings of inflammation. Radiology 238, 505–516 (2006)
4. Dyer, S.A., He, X.: Least-squares fitting of data by polynomials. IEEE Instrumentation & Measurement Magazine 4, 46–51 (2001)
5. Pontil, M., Verri, A.: Object recognition with support vector machines. IEEE Trans. Pattern Anal. Machine. Intell. 20, 637–646 (1998)
6. Schölkopf, B., Smola, A.: Learning with kernels. MIT Press (2002)
7. Metz, C.: Basic principles of ROC analysis. Semin. Nucl. Med. 8, 283–298 (1978)

Computer-Aided Detection of Small Bowel Strictures for Emergency Radiology in CT Enterography

Nisha I. Sainani, Janne Näppi, Dushyant V. Sahani, and Hiroyuki Yoshida

Department of Radiology,
Massachusetts General Hospital and Harvard Medical School,
25 New Chardon Street, Suite 400C,
Boston, Massachusetts 20114, USA
jnappi@partners.org, yoshida.hiro@mgh.harvard.edu

Abstract. Computer-aided detection (CAD) of small bowel strictures can have significant impact in improving the workflow of CT enterography in an emergency setting where even non-expert radiologists could use it to rapidly detect sites of obstruction. A CAD scheme was developed to detect strictures from abdominal CT enterography data by use of multi-scale template matching and a blob detector. A pilot study was performed on 15 patients with 22 surgically confirmed strictures to study the effect of the CAD scheme on observer performance. The 77% sensitivity of an inexperienced radiologist assisted by the CAD scheme was comparable with the 81% sensitivity of an unaided expert radiologist ($p=0.07$). The use of CAD significantly reduced the reading time to identify strictures ($p<0.0001$). Most of the false-positive CAD detections were caused by collapsed bowel loops, approximated bowel wall, muscles or vessels, and they were easy to dismiss. The results indicate that CAD can provide radiologists with rapid and accurate interpretations of strictures to improve workflow in an emergency setting.

Keywords: CT enterography, template matching, strictures, small bowel, emergency radiology.

1 Introduction

Small bowel obstruction (SBO) accounts for 12 – 16% of emergency surgical admissions for patients with abdominal pain [1]. Multi-detector CT (MDCT) has been acknowledged as the preferred diagnostic modality to identify SBO and its causes, as well as the life-threatening complications of SBO such as closed-loop obstruction, bowel ischemia/necrosis, or bowel perforation [1].

The potential of CT enterography (CTE) using neutral oral contrast to elucidate intraluminal and mural pathologies is being increasingly utilized for the evaluation of small bowel diseases [2]. However, identifying the transition zone in SBO among obstructed and dilated bowel loops can be time-consuming and challenging even for an experienced radiologist [3]. In particular, the analysis of CTE data from emergency admissions faces unique technical challenges that are different from those of

H. Yoshida et al. (Eds.): Virtual Colonoscopy and Abdominal Imaging 2010, LNCS 6668, pp. 91–97, 2011.

conventional CTE examinations. Because of the obstructions, orally administered contrast agent is either not used or the lumen is enhanced only partially. Also, the slice thickness of CT images can be much larger (5.0 mm or higher) than the in-plane resolution of the images. Therefore, three-dimensional (3-D) image analysis algorithms that assume isotropic image resolution are not necessarily applicable to the analysis of CT data from emergency admissions.

Because accurate and rapid diagnosis of partial or complete SBO is crucial for successful treatment, there has been interest in computer-assisted diagnosis of SBO. In a study where a Bayesian scheme was used to predict the character of SBO based upon a large number of symptoms and medical data [4], significantly less time was needed to make the diagnosis than with contrast radiography alone. More recently, a visualization scheme was developed to highlight regions of longitudinal ulcers in a positive-contrast enhanced small bowel [5].

We hypothesized that computer-assisted detection (CAD) could be used to identify CT image patterns of strictures directly from CT image data for assisting radiologists in locating possible sites of obstruction and for speeding up the evaluation of CTE scans. Based on this hypothesis, we developed a CAD scheme that detects strictures automatically from CTE images. To assess the impact of the CAD scheme in improving workflow, we evaluated its effect on radiologists' performance in the detection of SBO.

2 Method

2.1 CAD Scheme

We designed a CAD algorithm to detect image patterns characteristic of strictures based on the observation that most small bowel strictures tend to be indicated by two types of image patterns: (1) thread-like linear patterns of tight strictures or (2) luminal effacement patterns (Figure 1).

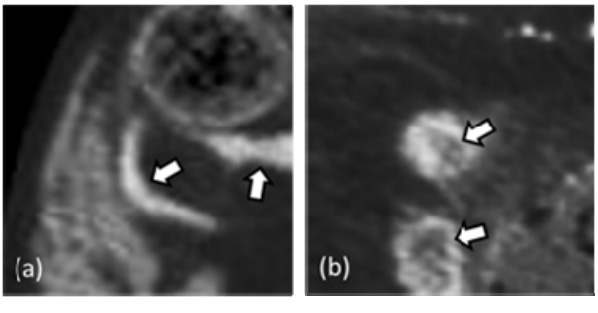

Fig. 1. Image patterns of strictures (arrows). (a) Thread-like strictures. (b) Luminal effacement patterns.

Figure 2 shows an overview of the algorithm. Because normal anatomy can imitate image patterns of SBO, thereby causing false-positive (FP) detections, it is first necessary to extract the approximate region of small bowel to determine a search region where the detection algorithms are applied. First, the region of air around abdomen (A) is identified by thresholding voxels with intensity values < -500 HU and by performing region-growing of the thresholded region starting from the corners of the CT volume (V). The external oblique muscle layer (M) below the skin line that can imitate SBO is excluded by adaptive morphologic dilation of A.

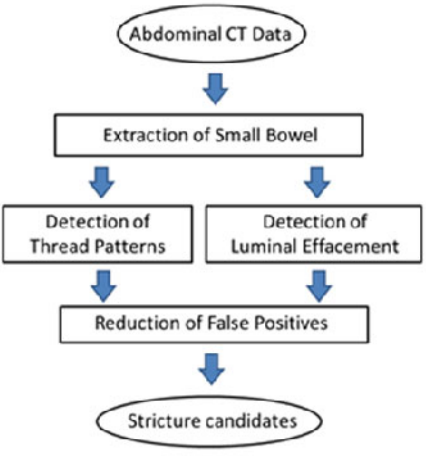

Fig. 2. Overview of the CAD algorithm

Next, because small bowel is contained anatomically below stomach in the middle and bottom regions of the CT scan volume, the top region of the abdomen (V_T) is subtracted by first determining the region of liver as the largest connected component that has enhanced intensity values at the top region of the CT volume, and by excluding the CT images containing the liver and above. Also large hyper-enhanced vessels (L) can imitate thread-like patterns of SBO: these are subtracted by region-growing of the voxels with elevated intensity values originating from the region of liver. Next, because small bowel is located inside the rib cage, the rib cage is identified by thresholding of high intensity values and by excluding the rib cage and its exterior region (B). These computation steps are implemented by combinations of the image processing operations of thresholding, binary morphology, region growing, and connected components analysis, and by an analysis of the spatial extent of the extracted regions. Thus, the final search region to detect SBOs is defined by the region of $V \setminus (A \cup M \cup V_T \cup L \cup B)$.

To detect thread-like strictures, these strictures can be modeled as thick curvilinear image patterns that have a higher intensity than their local background. The orientation and thickness of such patterns can be determined by application of a multi-scale template matching method. First, a rectangular template with orientation d_i ($i = 1,..,D$) and thickness t_j ($j = 1,..,T$) is placed to an operating point (Figure 3a).

After calculating the average intensity of the voxels covered by the template region ($F(d_i,\ t_j)$) and the average intensity of its surrounding region ($R(d_i,\ t_j)$) (Figure 3b), the accuracy of the match is calculated as $S(d_i, t_i) = F\big(d_i, t_j\big) - R(d_i, t_j)$ [6]. The calculations are repeated for the different thicknesses t_j of the template Figure 3c). Next, the template is rotated to the next orientation d_i (Figure 3d), and the calculations are repeated for this new orientation. The actual orientation and scale of the underlying linear pattern is indicated by the orientation d_{max} and thickness t_{max} for which $S(d_{\max}, t_{max}) \geq S\big(d_i, t_j\big), i = 1,..,D; j = 1,..,T$ (Figure 3e).

Because the template is defined everywhere in the image data and not all linear patterns represent strictures, we placed additional constraints to voxels that may be considered as stricture candidates by the multi-scale template method. First, the average intensity of the voxels within the template region should be higher than those at either side of the template in the background region: this minimizes detections due to edges of large objects. Second, the thickness of the template should be typical of strictures; that is, the accuracy of the final match, $S(d_{\max}, t_{max})$, should not be too low. Third, voxels that satisfy the above two conditions should define 3-D regions that are not too small or too large for a stricture. Figure 3f shows some of the stricture candidates detected in this manner.

Luminal effacement patterns can be modeled as small pockets of low density within bowel lumen that are surrounded by the higher density of the thick enhancing wall of a stricture. To detect such image patterns, we defined a blob detector kernel

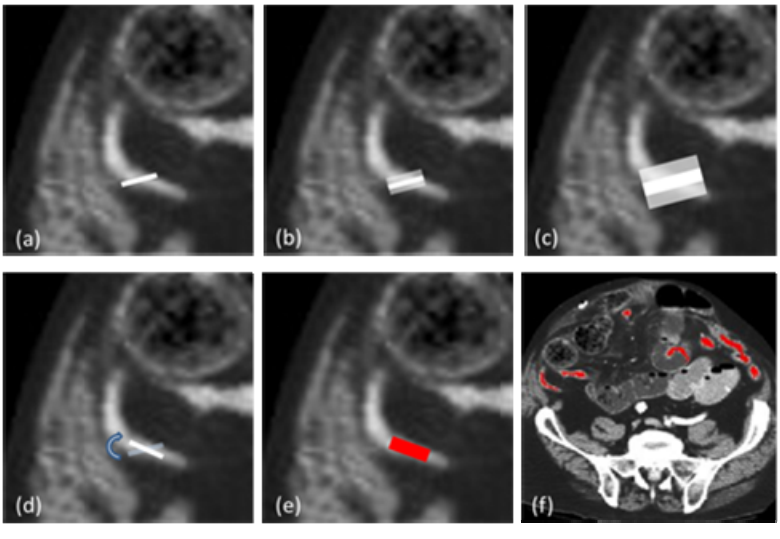

Fig. 3. Detection of strictures by the multi-scale template method. (a) A template (white region). (b) The grey regions on either side of the template local background. (c) A higher-scale template. (d) The template is rotated around the operating point. (e) The best-matching template defines the orientation and scale of the underlying linear pattern (red box). (f) Examples of detected stricture candidates (red regions).

based on the Wald distribution $f(x;\mu,\lambda) = \left[\frac{\lambda}{2\pi x^3}\right]^{1/2} exp\frac{-\lambda(x-\mu)^2}{2\mu^2 x}$, where $\mu > 0$ is the mean and $\lambda > 0$ is a scaling parameter. To detect luminal effacement, the image function g is convoluted with a two-dimensional kernel as $(f * g)(n) = \sum_m f(n-m)g(m)$. To reduce FP detections, any detected candidate regions smaller than 5 mm^2 or larger than 10 mm^2 are excluded.

To reduce FP stricture candidates due to image patterns attributable to image noise or normal anatomy, the detected regions from individual 2-D images are merged into 3-D components. Any stricture candidates smaller than 100 mm^3 (too small) or larger than 1000 mm^3 (too large) are excluded. Also, any stricture candidates detected by the multi-scale template method with CT values lower than 50 HU (non-enhanced) or higher than 150 HU (excessive enhancement) are excluded, and any stricture candidates detected by the blob detector with CT values higher than 50 HU (not likely to represent a luminal effacement pattern) are excluded. The remaining stricture candidates are considered as the final detected strictures.

2.2 Clinical CT Enterography Cases

We performed a retrospective review of the hospital radiology database from the period of July 2008 through February 2009, and identified a pilot cohort of 15 patients (7 women and 8 men; 17– 83 years, mean age 46.5 years). All these patients had a diagnosis of SBO due to strictures confirmed by surgery and histopathology. Before the surgery, the patients had been subjected to CTE on a 16-slice MDCT scanner (Light-Speed, GE Medical Systems, Milwaukee, WI). Depending on the patient's clinical status and tolerance, 900 to 1350 mL of neutral oral contrast material (VoLumen 0.1% w/w, 0.1% w/v barium sulfate, Bracco Diagnostics Inc., NJ) had been consumed over 40 – 60 minutes prior to the scan. A contrast-enhanced scan had been acquired from the xiphoid to pubic symphysis during the portal venous phase 60 – 70 seconds after intravenous injection of 100–120 mL of non-ionic contrast (Isovue 300 – 370 mg I/ml, Bracco Diagnostics, Princeton, NJ) with a power injector at the rate of 2.5 – 3.0 mL/sec. The MDCT parameters used were: tube voltage of 120 – 140kVp, current determined by automated tube-current modulation, detector collimation of 0.625 mm, table speed of 18.75 mm/sec, tube rotation of 0.5 seconds, and pitch of 0.938–1.375.

An independent unblended reader reviewed the surgical records and operative details of the patients from the electronic hospital database. The number and site of strictures were used as a reference standard for the study.

3 Results

There were a total of 22 surgically confirmed strictures in the 15 patients, of which 9 were in mid ileum, 2 in the distal ileum, 8 in the terminal ileum, 1 in the neo-terminal ileum, and 2 at ileostomy sites. Seven patients had 2 strictures, while the others (8 patients) had 1 stricture each. Two patients with 1 stricture each in the mid and distal ileum were diagnosed with carcinoid tumor. The other patients were inflammatory strictures due to Crohn's disease.

3.1 Image Analysis by an Experienced Radiologist without CAD

The images were reviewed by an experienced radiologist with training in abdominal radiology and with 13 years of experience in interpreting abdominal CT studies. The radiologist correctly diagnosed 18/22 strictures with per-stricture and per-patient sensitivities of 82% and 100%, respectively. Two FP detections (collapsed segments of bowel) and 4 false-negative (FN) detections were rendered. The time taken by the experienced radiologist to view the axial and coronal images and locate the strictures per patient ranged from 140 to 186 seconds (mean 159 seconds).

3.2 Image Analysis by an Inexperienced Radiologist Assisted by CAD

First, the CAD scheme was used to detect strictures automatically from the cases. A 15-degree angular resolution and 6-mm and 12-mm template thicknesses were used. For each patient, CAD generated 3–10 stricture candidates (average, 5 per patient). Thus, a total of 88 stricture candidates were identified.

The radiologist could easily dismiss the FP images of CAD stricture candidates that were due to bowel folds or approximated wall of small bowel loops (31/88), collapsed bowel loops (12/88), muscles (19/88), and vessels (4/88). In cases with long strictures (n=5), CAD could identify different points on the same stricture as multiple strictures (2 technical FPs in each case). After exclusion of these false positives, 17 stricture candidates were labeled as true strictures. In 4 patients with 2 confirmed strictures each, CAD detected only one stricture in each case because it could not separate multiple strictures in close proximity. In one patient, a small segment of stricture was not identified by CAD, resulting in a total of 5 FNs.

The per-stricture and per-patient sensitivity of the radiologist with CAD was 77% and 93%, respectively. The per-patient time taken by the radiologist to browse through the stricture candidates to dismiss anatomical structures that simulated strictures, and to set apart true strictures, ranged from 35 to 58 seconds (mean: 46 seconds).

3.3 Comparison of Readers' Results with and without CAD

There was no statistically significant difference in the detection sensitivity of strictures by the experienced radiologist alone and by the inexperienced radiologist with CAD (McNemar's test; per-stricture $p = 0.07$; per-patient $p = 1.00$). However, with CAD, the time to identify strictures was significantly less than that taken by the radiologist to detect strictures on CTE (Student's t-test: $p<0.0001$).

4 Conclusion

The application of CAD to localize image-based sites of obstruction due to strictures appears to be feasible in CTE. The accuracy of the diagnosis with CAD was comparable to that made by an experienced radiologist on CT images alone.

Therefore, CAD can serve as a second reader to focus radiologist's attention rapidly to potential areas of interest in cases where CTE findings can suggest obstruction. The use of CAD can empower the radiologist to render a more rapid interpretation of small bowel obstructions caused by strictures, thereby improving workflow.

References

1. Maglinte, D.D., Heitmap, D.E., Howard, T.J., Kelvin, F.M., Lappas, J.C.: Current concepts in imaging of small bowel obstructions. Radiol Clin. North Am. 41, 263–283 (2003)
2. Young, B.M., Fletcher, J.G., Booya, F., et al.: Head-to-head comparison of oral contrast agents for cross-sectional enterography: small bowel distention, timing, and side effects. J. Comput. Assist. Tomogr. 32, 32–38 (2008)
3. Shah, Z.K., Uppot, R.N., Wargo, J.A., Hahn, P.F., Sahani, D.V.: Small bowel obstruction: the value of coronal reformatted images from 16-multidetector computed tomography - a clinicoradiological perspective. J. Comput. Assist. Tomogr. 32, 23–31 (2008)
4. Bogusevicius, A., Maleckas, A., Pundzius, J., Skaudickas, D.: Prospective randomised trial of computer-aided diagnosis and contrast radiography in acute small bowel obstruction. Eur. J. Surg. 168, 78–83 (2002)
5. Oda, M., Furukawa, K., Kitasaka, T., et al.: Development of computer-aided diagnosis system for Crohn's disease using virtual unfolded views. Int. J. Cars 5, 79–79 (2010)
6. Zwiggelaar, R., Parr, T.C., Taylor, C.J.: Finding orientated line patterns in digital mammography images. In: Proc. 7th Br. Machine Vision Conf., pp. 715–724 (1996)

Teniae Coli Extraction in Human Colon for Computed Tomographic Colonography Images

Zhuoshi Wei, Jianhua Yao, Shijun Wang, and Ronald M. Summers

Imaging Biomarkers and Computer-Aided Diagnosis Laboratory,
Radiology and Imaging Sciences, National Institutes of Health Clinical Center,
Bethesda, MD, 20892, USA
{zhuoshi.wei,rms}@nih.gov,
{jyao,wangshi}@cc.nih.gov

Abstract. Teniae coli are three bands of longitudinal smooth muscle on the surface of the colon, serving as anatomically meaningful landmarks for guiding virtual colonoscopic navigation and registration. This paper presents a novel method for teniae coli extraction for CT colonography. Because teniae coli are muscles running between haustral folds, they can be extracted by analysis of fold information. In our method, the 3D colon surface is first preprocessed into a 2D flattened colon. Then a 2D Gabor filter is employed to extract the feature of haustral folds, following by a Sobel operator to enhance the fold edge. The fold center is then detected by thresholding. A path of the fold can be obtained by connecting the fold center. Teniae coli are then extracted as lines in the middle of a pair of fold paths. Experiments were carried out on 5 cases, and the normalized RMSE was 5.01% with a 4.13% standard deviation.

Keywords: CT colonography, teniae coli, Gabor filter.

1 Introduction

Computed tomographic colonography (CTC) is an emerging minimally invasive technique for colonic polyps and cancer screening [1]. Computer-aided diagnosis (CAD) systems enable radiologists to identify colon polyps more easily and accurately. Teniae coli are three bands of longitudinal smooth muscle on the colon surface. They are parallel, equally distributed on the colon wall, and form a triple helix structure from the appendix to the sigmoid colon. Fig.1 illustrates a human colon and the configuration of teniae coli. Because of their characteristics, teniae coli are important, meaningful anatomic landmarks on the human colon, serving as ideal reference for guiding virtual navigation and polyp registration.

Teniae coli are extractable landmarks. Existing methods for extracting teniae coli can be grouped into two categories, manual and automatic. Huang et al. [2] manually extracted teniae omentalis (TO), the most visible tenia coli on a well-distended colon. Then the shortest path through the TO points was derived on the surface. Another, similar method proposed by Huang et al. [3] detected haustral folds by using a curvature-based filter and assigned color to aid the identification of the teniae coli.

H. Yoshida et al. (Eds.): Virtual Colonoscopy and Abdominal Imaging 2010, LNCS 6668, pp. 98–104, 2011.

Lamy and Summers [4] used a curvature filter with a refinement process to detect haustral folds. The extremities of the folds were computed and clustered, forming the segments of the teniae coli. Chowdhury et al. [5] used heat diffusion and fuzzy C-means clustering to detect haustral folds. They used a histogram to analyze the extremities of the fold, serving as landmarks for detecting teniae. Umemoto et al. [6] also used curvature information to extract haustral folds. The gravity centers of the folds were obtained and connected to extract the running directions of folds. The teniae coli can be located as lines running between the fold centers.

In this paper, we propose a novel method for teniae coli detection on CT colonography. The 3D colon surface is first preprocessed into a 2D flattened colon. The image-processing is done on the 2D flattened image. The proposed method makes used of 2D Gabor filters to extract the features of haustral folds. Then a Sobel operator is performed on the filtering results to acquire the edge of the folds. Thresholding is applied to identify the fold centers. By connecting of the fold centers, a path of the fold can be obtained. Teniae coli are then extracted as lines running between fold paths.

The remainder of this paper is organized as follows: section 2 briefly describes the image preprocessing of colon unfolding; section 3 presents the proposed method, including fold detection and the extraction of teniae coli; section 4 describes the experiments and presents the results, section 5 concludes the paper.

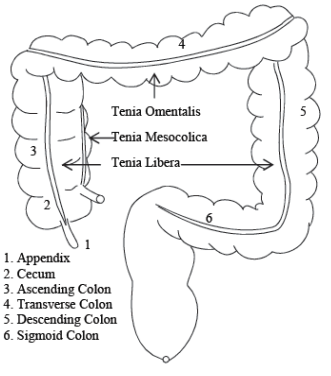

Fig. 1. Colon and teniae coli configuration (from Ref. [3].)

2 Colon Unfolding

The main steps in our method are done on the 2D flattened colon instead of 3D to simplify the procedure. Therefore, we first need to unfold the 3D images into the 2D flattened colon. In the colon-unfolding procedure, we make use of advanced algorithms including rotation-minimizing frames, recursive ring sets, mesh skinning, and cylindrical projection [7]. Fig.2(a) shows a 3D colon surface, and Fig.2(b) shows its unfolded view. The unfolded colon is mapped to a rectangular region (shown in Fig.2(c)) for the purpose of 2D image processing.

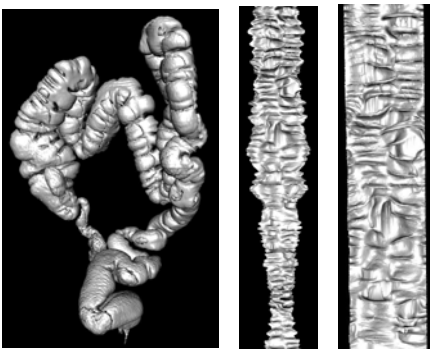

(a) (b) (c)

Fig. 2. (a) 3D CTC. (b) Unfolded colon. (c) Unfolded colon mapped to a rectangular region.

3 Teniae Coli Extraction for CT Colonography Images

3.1 Gabor Filter for Fold Feature Extraction

Two-dimensional Gabor filters can simulate the receptive field of the human visual cortex[8]. With various scales and orientations, 2D Gabor filters can achieve an optimal description in the spatial and frequency domain. A Gabor filter is obtained by modulating of a complex sinusoid with a Gaussian:

$$\begin{aligned} h(x, y, \theta, \phi) &= g(x, y) \cdot \cos(2\pi\theta(x\cos\phi + y\sin\phi)) \\ &\quad + ig(x, y) \cdot \sin(2\pi\theta(x\cos\phi + y\sin\phi)) \ , \end{aligned} \tag{1}$$

where θ denotes the frequency and ϕ denotes the orientation of the Gabor function. $g(x, y)$ is an isotropic Gaussian function: $g(x, y) = \frac{1}{2\pi\sigma^2}\exp(-\frac{x^2 + y^2}{2\sigma^2})$.

The real part of Eq.1 corresponds to the even Gabor function, and the imaginary part corresponds to the odd Gabor function. Fig.3(a) and (b) show the spatial response profile of the even and odd Gabor function, respectively. Fig.3(c) and (d) show their intensity plots with orientation $\phi = \pi/2$. The response of the Gabor filter to an image can be acquired by 2D convolution: $G(x, y, \theta, \phi) = \int\int I(p, q)h(x - p, y - q, \theta, \phi)\ dp\ dq$, where $I(x, y)$ denotes the image, and $G(x, y, \theta, \phi)$ denotes the filtering response with frequency θ and orientation ϕ.

Haustral folds are structures perpendicular to the centerline of the colon. For the 2D flattened colon, haustral folds are present as horizontal textures on the colon wall (see Fig.2(c)). Generally speaking, there are three sets of haustral folds lying side by side along the colon wall, separated by and perpendicular to the three teniae coli. Therefore, we select a Gabor filter with orientation $\phi = \pi/2$ to detect haustral folds. The side lobes of this specific filter are parallel in the horizontal direction, as shown in Fig.3(c) and (d), which can well extract the feature of the folds. Malik and Perona [9] showed that texture segregation is mainly based on even symmetric mechanisms. In this paper, we applied an even Gabor filter to extract haustral fold features.

By convolving of the Gabor filter with the colon image, the response image $G(x,y,\theta,\phi)$ can be obtained to highlight the region of the haustral fold, as shown in Fig.4(b). Then we use a Sobel operator to enhance the response image and meanwhile obtain a sharper edge of the folds. We used a horizontal Sobel operator in our experiment, since the folds were mostly running in the horizontal direction. The resulting edge image $E(x,y)$ can be obtained by convolving Sobel operator S with the Gabor filtering response: $E(x,y)=S*G(x,y,\theta,\phi)$. Fig.4(c) shows the gradient image $E(x,y)$.

3.2 Identifying Center of Haustral Folds by Use of Thresholding

Identifying the haustral fold center is treated as a thresholding problem. This is done on the gradient image $E(x,y)$. This process can be divided into two steps. Since the folds are thin and elongated structures, our first step is to locate the vertical coordinates of the folds. This can be done by accumulating the pixel intensity in the horizontal direction $f_y = \int_x E(x,y)dx$, and labeling the local maxima $f_{y\max}$ of the vector that is larger than a threshold: $f_y > th_y, f_y^{'}=0, \& f_y^{''}<0$. The second step is to locate their horizontal coordinates. As each fold approximately occupies one third of the colon circumference, we compute the cumulating intensity of a region about the same height as that of a fold, with its vertical coordinate near each $f_{y\max}$, describing as: $f_x = \int_{f_{y\max}-\varepsilon}^{f_{y\max}+\varepsilon} E(x,y)dy$. Again we locate the local maxima $f_{x\max}$ of the patch intensity to obtain a horizontal coordinate by using a similar approach. All of the points with coordinates $(f_{x\max}, f_{y\max})$ serve as the fold centers. Fig.4(d) shows the haustral fold centers obtained in the experiments.

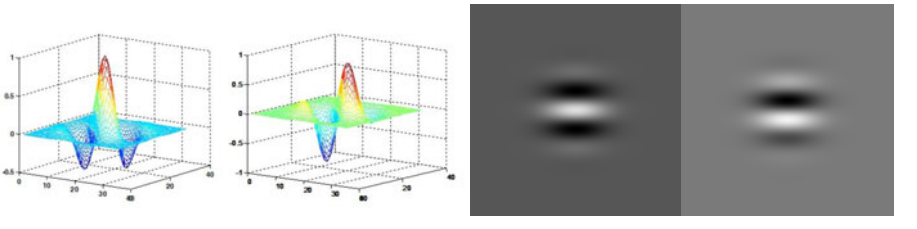

(a) (b) (c) (d)

Fig. 3. (a) Even Gabor spatial response. (b) Odd Gabor spatial response. (c) Intensity plots of amplitude of even Gabor filter. (d) Intensity plots of amplitude of odd Gabor filter.

3.3 Extraction of Teniae Coli

Teniae coli are located where the haustral folds meet. Connecting the fold centers yields a path of the folds running direction, and each tenia coli is in the middle of a

pair of fold paths. The slope of the line between two connecting fold centers should be within a threshold to ensure that two folds in different paths are not connected. Fig.4(e) shows an example of a pair of paths of haustral fold centers. Fig.4(f) highlights a tenia in bold between the fold center paths. Fig.4(g) presents one tenia coli on the colon surface.

Using the above method, one of the teniae coli can be obtained using information on every two fold paths. Since the unfolded colon is cut open from the tube structure, the vertical borders of the flattened colon are actually connected. To locate the other teniae coli, the borders of the image are spliced to form a periodic structure. With a similar approach, more teniae coli can be extracted from the unfolded image.

4 Experimental Results

Experiments were carried out on 5 cases of images with different resolution. The window sizes for the Gaussian function in Eq.1 are chosen based on the image resolution, e.g., for an $n \times n$ 2D Gaussian function, n is selected as: $n = 0.05 \times W_{colon}$, where W_{colon} denotes the width of the 2D flattened colon. The orientation of the Gabor filter is chosen as $\phi = \pi/2$ as mentioned in Section 3.1. Since the resolution of the image is varying, we used different scales for Gabor filters with the radial frequency selected as $\sqrt{2}$, $2\sqrt{2}$, $4\sqrt{2}$, and $8\sqrt{2}$. The thresholds used to identify the fold center are selected empirically based on the average intensity of the fold region. A normalization term is also applied when the threshold is chosen, considering that the resolution of the images is different. The angle of the line for connecting two fold centers is restricted within $\pi/4$, to avoid folds in different paths connect together.

Teniae coli detection results are given in Fig.5. The images are from different patients. We manually labeled the teniae coli as the reference standard (blue line in Fig.5) to evaluate the detection results (red line in Fig.5). The root mean square error (*RMSE*) of the detection result is *5.01%*, which is normalized by the circumference of the colon. The standard deviation is *4.13%*.

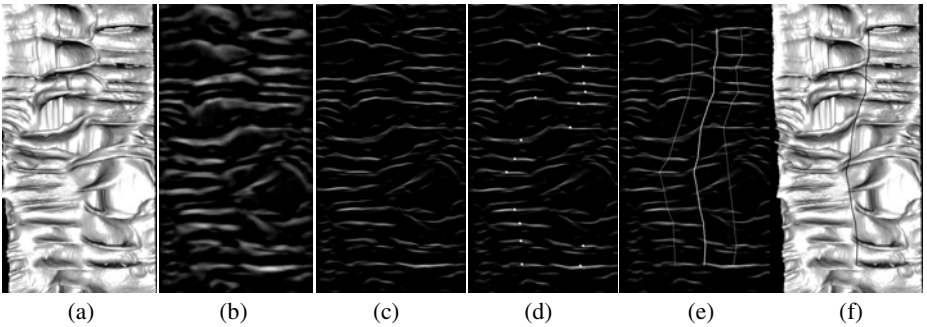

Fig. 4. (a) An example of 2D flattened colon. (b) The response 2D Gabor filter to image (a). (c) Sobel operator applied to image (b). (d) The detected fold center. (e) Fold centers and tenia coli (the bold line running between two fold center path). (f) Tenia coli shown on colon wall.

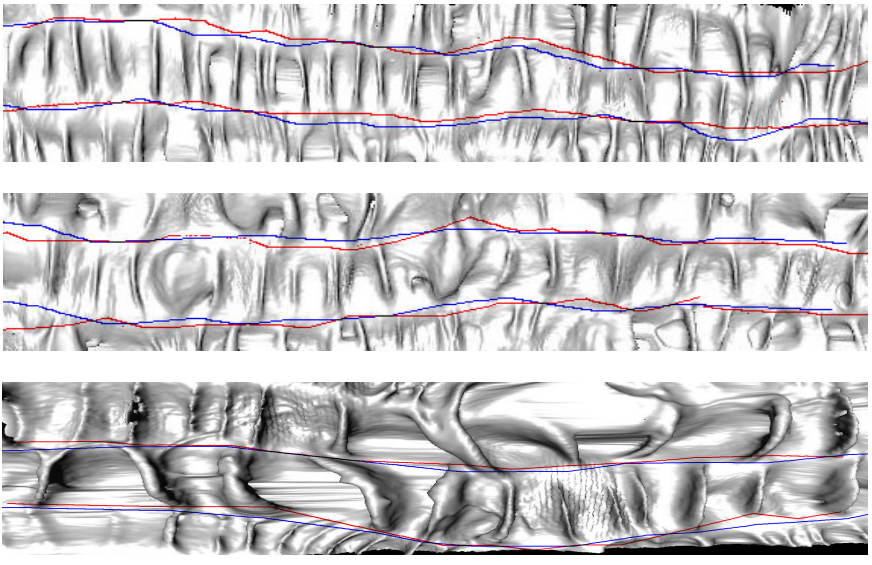

Fig. 5. Teniae coli extraction results for 3 different patients: blue lines indicate the reference standard; red lines indicate the detection results

5 Conclusion and Future Work

In this paper, we have proposed a novel teniae coli extraction method for CT colonography. We first unfold the colon surface into a 2D flattened colon. Two-dimensional Gabor filters are applied to extract fold features. A Sobel operator is used to extract the edge of the folds. The centers of the folds are then identified by thresholding. A path of the folds can be derived by connecting the fold centers. The teniae coli are finally extracted as the medial lines running between fold paths.

In the future, more work can be done to improve the current results. 1) As teniae coli are parallel and equally distributed on the human colon, if one tenia is detected, its information can be used to locate other teniae coli. However, since the teniae line would have deformation on the colon surface in most cases, further optimization should be done to refine the locating results with this method. 2) Further study should be carried out to define and evaluate the performance, and how it would benefit clinical research.

References

1. Summers, R.M., Yao, J., Pickhardt, P.J., Franaszek, M., Bitter, I., Brickman, D., Krishna, V., Choi, J.R.: Computed Tomographic Virtual Colonscopy Computer-Aided Polyp Detection. A Screening Population, Gastroenterology 129, 1832–1844 (2005)
2. Huang, A., Roy, D.A., Summers, R.M., Franaszek, M., Petrick, N., Chol, J.R., Pickhardt, P.J.: Teniae Coli-based Circumferential Localization System for CT Colonography: Feasibility Study. Radiology 243(2), 551–560 (2007)

3. Huang, A., Roy, D.A., Franaszek, M., Summers, R.M.: Teniae Coli Guided Navigation and Registration for Virtual Colonoscopy. In: Proc. IEEE Visualization, pp. 279–285 (2005)
4. Lamy, J., Summers, R.M.: Teniæ Coli Detection from Colon Surface: Extraction of Anatomical Markers for Virtual Colonoscopy. In: Bebis, G., Boyle, R., Parvin, B., Koracin, D., Paragios, N., Tanveer, S.-M., Ju, T., Liu, Z., Coquillart, S., Cruz-Neira, C., Müller, T., Malzbender, T. (eds.) ISVC 2007, Part I. LNCS, vol. 4841, pp. 199–207. Springer, Heidelberg (2007)
5. Chowdhury, A.S., Yao, J., VanUitert, R.L., Linguraru, M.G., Summers, R.M.: Detection of Anatomical Landmarks in Human Colon from Computed Tomographic Colonography Images. In: Proc. ICPR (2008)
6. Umemoto, Y., Oda, M., Kitasaka, T., Mori, K., Hayashi, Y., Suenaga, Y., Takayama, T., Natori, H.: Extraction of Teniae Coli from CT Volumes for Assisting Virtual Colonoscopy. Proc. SPIE, vol. 6916, 69160D-1-10 (2008)
7. Yao, J., Chowdhury, A.S., Aman, J., Summers, R.M.: Reversible Projection Technique for Colon Unfolding. IEEE Transactions on Biomedical Engineering (in press)
8. Daugman, J.: Two-dimensional Spectral Analysis of Cortical Receptive Field Profiles. Vision Research 20(5), 847–856 (1980)
9. Malik, J., Perona, P.: Preattentive Texture Discrimination with Early Vision Mechanisms. Journal of Optical Society of America A 7, 923–932 (1990)

Extraction of Landmarks and Features from Virtual Colon Models

Krishna Chaitanya Gurijala, Arie Kaufman, Wei Zeng, and Xianfeng Gu

Computer Science Department,
Stony Brook University, Stony Brook, NY 17794-4400, USA
{gkrishna,ari,zengwei,gu}@cs.sunysb.edu

Abstract. The colon is a very complicated structure with a large number of distortions and bends. Landmarks and features serve as tools to guide colon flattening and to assist in the study of the colon surface segment by segment. Identification of feature points and landmarks is also useful for the registration of colon surfaces. In this paper, we present methods for identifying the locations of the taeniae coli and the four major flexures which form the prominent anatomic landmarks on the colon surface. The colon surface is cut open along these landmarks, and the segments obtained can be used for study of the surface of the colon. We define new feature points on the flattened colon surfaces and use well-established graph-based algorithms for their detection. We demonstrate the results showing the extracted landmarks and the detected features.

Keywords: virtual colonoscopy, haustral folds, taeniae coli, flexures, graph-cut, max-flow min-cut.

1 Introduction

Virtual colonoscopy (VC) has been developed as a non-invasive, safe, accurate, and low cost alternative to conventional optical colonoscopy for the early detection of colorectal cancer. In VC, CT scans are typically acquired with the patient in both supine and prone positions to improve the detection rate. However, the colon is flexible and changes easily with the change in position of the patient. Thus, to understand the surface of the colon and to help the physician identify the current position in the colon during navigation, landmarks and feature points are necessary. These landmarks and features can be used for applications in the VC system such as virtual navigation, virtual dissection, colon surface registration, polyp matching, and polyp bookmarking. The landmarks and feature points also help one to toggle between the supine and prone positions to confirm a polyp location.

Taeniae coli are the significant anatomic landmarks stretching along the entire length of the colon. We extend previous ideas on extracting the taeniae coli on the colon surface. In addition, there are four major flexures which also serve as good anatomic landmarks. We present a method to identify the locations of the four major flexures, which are the prominent flexures in the colon, by using CT colon data. The

H. Yoshida et al. (Eds.): Virtual Colonoscopy and Abdominal Imaging 2010, LNCS 6668, pp. 105–112, 2011.

colon surface is cut and unfolded along a taenia coli and the flexures to obtain precisely five flat colon segments. These segments are used for segment wise comparison of supine and prone colon surfaces, to know about the haustral folds and to understand the intricacies of the surface of the colon. We define feature points on these flattened colon surfaces and use well-established graph-based algorithms for their detection.

2 Extraction of Anatomic Landmarks

Taeniae coli and flexures are important anatomic landmarks of the colon. These anatomic landmarks in both the supine and prone colon are automatically extracted in a robust manner and are used to cut the colon into its anatomic segments and to slice the colon open for flattening, thereby aiding in virtual colon dissection.

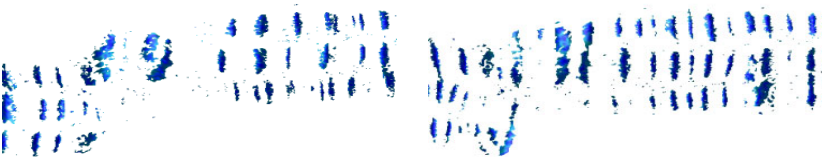

Fig. 1. Haustral folds (blue) on the prone and supine colon surfaces, respectively

Taeniae coli are three bands of longitudinal muscle on the surface of the colon. They form a triple helix structure from the appendix to the sigmoid colon. They are ideal references for virtual navigation in VC. The taeniae coli are named taenia omentalis, taenia mesolica, and taenia libera according to their position on the transverse colon. Taeniae coli are essentially located where the haustral folds meet and hence can be regarded as ridge breakers for the haustral folds. The taenia omentalis is the easiest to spot because it is clearly visible on the transverse colon. Essentially, the taeniae coli detection is based on the detection of haustral folds [1, 2]. By use of the haustral folds, the taenia omentalis is initially extracted, and from which the taenia mesolica and taenia libera are later extracted as straight lines approximated at one third and two thirds of the circumference of the colon.

The sense of direction along the colon surface is defined by use of the centerline of the colon. The hasutral folds are detected by use of the characteristic hyperbolic curvature of the folds. By use of heat diffusion, a curvature-based filter [7], and connected components, the haustral folds are detected. The curvature filter helps to obtain a rough set of all points which form potential candidates for the folds, and these folds are assigned a different color to identify the taeniae coli quickly. These points are obtained with use of an experimentally determined threshold value. The threshold values to obtain the points belonging to the haustral folds, for the datasets we used, lie in the range -4.5 to -0.5. Finally, by finding the connected components and performing a certain amount of geometric processing, we obtain the haustral folds. Fig. 1 shows the haustral folds detected in prone and supine colons. With use of

these haustral folds, the taeniae coli are extracted by iterative use of the fuzzy C-means clustering algorithm [3]. Fig. 2 shows the extracted taenia coli on the colon surface. The detected taeniae coli are used in colon flattening. In some datasets, where automatic extraction of taeniae coli is not possible, manually placed markers could be used to improve the reliability. Out of the 9 datasets on which we tested the algorithm, manual markers were needed on two datasets. The taenia coli is extracted to be used as a guide for virtually cutting open the colon so that it can later be used for detection of feature points. Considering this requirement, detection of the taeniae coli by use of our algorithm is reliable and very accurate. The haustral fold detection and the taeniae coli detection are performed on the original colon surface directly.

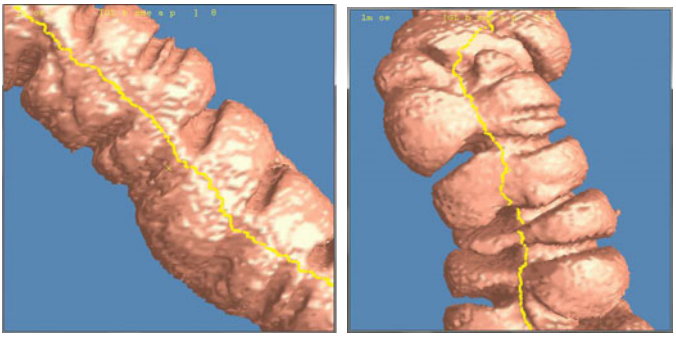

Fig. 2. Taenia coli (yellow) shown in the transverse (left) and the ascending (right) colon segments

We also present a method to identify the locations of the four major flexures in the colon. These flexures serve as further anatomic landmarks which help in virtual navigation. Moreover, the flexures can be used for supine-prone alignment and cutting. The first major flexure occurs between the ascending colon and the transverse colon (A-T flexure). This is the flexure close to the liver and is called the hepatic flexure. The second major flexure occurs between the transverse colon and the descending colon (T-D flexure). This flexure is close to the spleen and is named the splenic flexure. The third flexure occurs between the descending colon and the sigmoid (D-S flexure) and the final flexure is between the sigmoid and the rectum (S-R flexure).

In our experience, all of these four flexures form very sharp bends and are distinguishable from other, smaller bends. Theoretically, the A-T flexure forms the topmost point of the ascending colon, and the T-D flexure forms the topmost point of the descending colon. Our method uses the centerline of the colon for the detection of these flexures. By use of reported approaches [4, 5], the colon centerline is initially computed. This centerline is projected onto a 2D coordinate system in the positive $z-x$ and positive $y-z$ planes. The centerline is projected onto two separate axes in order to remove any chance of ambiguities caused by the flexible shape of the centerline. In both planes, the bends in the centerline are identified by iteratively evaluating the slopes along the projected curves. Because not all of the bends are important, all small bends are discarded based on an experimental threshold value and

only the major bends are retained, which are relatively sharper. In our case, we chose the normalized threshold value to be between 0.85 and 1. All of these detected bends are sorted based on their z-coordinate (up direction). The T-D flexure (hepatic) is identified as the bend with the highest z-coordinate, and the A-T flexure (splenic) is identified as the bend with the second highest z-coordinate. The S-R flexure is the bend with the lowest z-coordinate. The D-S flexure is identified as the next bend in the sorted order after the T-D flexure which has a y-coordinate comparable to that of the T-D flexure. Once the flexure coordinates are obtained on the 2D axes, the four positions are mapped back to the 3D coordinate system, and thus the corresponding 3D coordinates of the centerline are obtained.

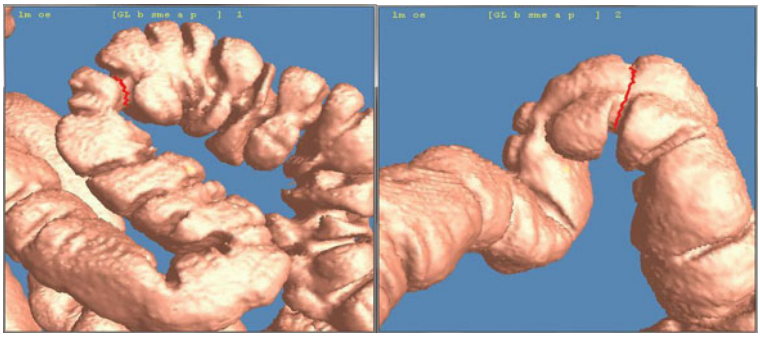

Fig. 3. Hepatic (left) and splenic (right) flexures (marked in red band) on the colon surface

For each of these points, a plane is defined passing through the point perpendicular to the centerline and tangential to that point. The intersection of the plane with the mesh surface is computed and a polyline is marked by joining the intersection points using Dijkstra's algorithm. Thus, the four major flexures are extracted on the colon's surface. Fig. 3 shows the hepatic and the splenic flexures marked on the colon surface.

3 Detection of Features

The colon surface is opened up along the taenia coli and cut along the flexures to yield five flat anatomic segments. We now focus on obtaining more feature points on these flat colon surfaces which are used to toggle between corresponding positions in the supine and prone colon surfaces.

For each of the flat segments obtained, we color encode the mean curvature to generate the color images. These color encoded flat colon segments are used for the feature point detection. Fig. 4 shows the color encoded mean curvatures on the flat supine and prone colon segments. The only tangible regions of interest on these flattened supine and prone colon surfaces are the folds which have already been detected previously. As one can see in Fig. 4, the folds are color-encoded in blue, and the surface has been encoded in green and red. We need to separate these folds from

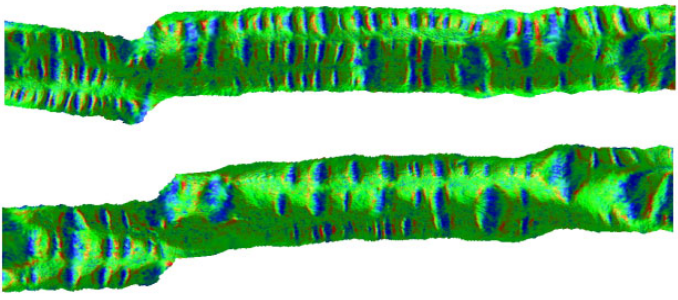

Fig. 4. The color encoded mean curvatures on the flat supine and prone colon segments

the rest of the surface in order to detect the feature points. For this, we use the well-known graph-cut algorithm from computer vision, which is very simple and quick. A graph is constructed initially by use of the pixels of the image as the nodes. With assumption of a virtual sink and source, edges are constructed with appropriate weights assigned. Finally, solving the energy minimization problem by using the max-flow min-cut method [6], all of the pixels belonging to the folds are obtained. Efficient detection of the folds is guided by the choice of weights for the edges. Thus, appropriate assignment of weights will ensure good results. In this step, we are not using the graph-cut algorithm to detect the folds; rather, we are using it to separate the previously detected folds from the rest of the surface.

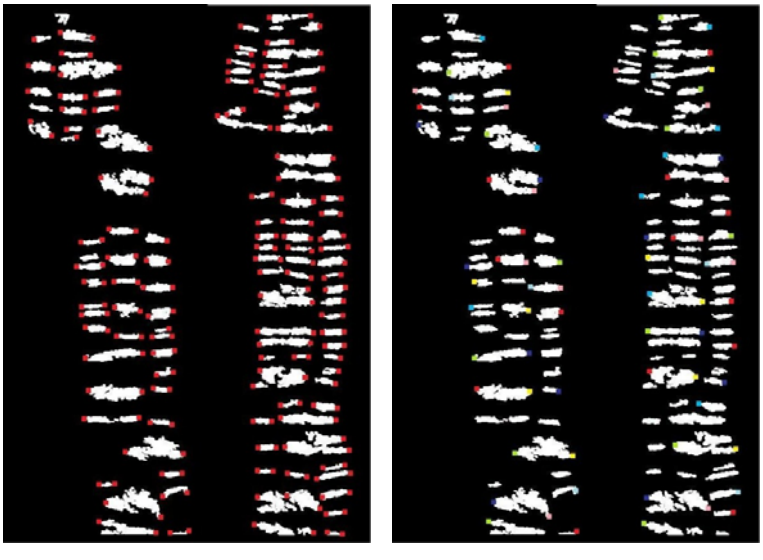

(a) (b)

Fig. 5. (a) The set of all feature pairs in prone and supine colon segments; (b) feature correspondences shown in prone and supine colon segments

However, due to the drastic change in position of the patient in supine and prone, the colon tends to stretch and move, resulting in distortion of the folds. Moreover, there might be some areas with more folds, whereas there might be other areas with fewer folds. In order to overcome the ambiguities caused by these problems, only significant folds have to be selected which have a relatively lesser degree of distortion. Therefore, all of the folds whose length and size are below a certain experimental threshold value are discarded, and only the prominent folds are retained. Hence, based on this requirement, we can decide on the number of folds by varying the threshold value. This threshold value is finalized by inspection of the visual output. In our experience, for the datasets we used, this value varied between 45 and 250 (constant per dataset).

These folds can be approximated by ellipses, and the axial points of these folds form a good set of feature points for subsequent applications. Thus, these axial points are extracted to yield a feature point set. We now perform feature matching to find a correspondence between the extracted feature points in the supine and prone positions. It is again formulated as an energy minimization problem by defining an objective function. The objective function is defined by considering two energy terms. The first term considers the geometric distance between the feature points inside a neighborhood, and the second term takes into account the effect of the unmatched or wrongly matched features. This function is minimized by use of the dual decomposition technique, thus yielding the feature correspondences. Suppose P_1 and P_2 are the feature point sets on supine and prone flattened surfaces, respectively, and Φ: $P_1 \rightarrow P_2$ is the matching, then the objective function is defined as

$$E(\phi) = \lambda \sum_{p \in P_1} |p - \phi(p)|^2 + (1 - \lambda) \sum_{q \in P_2 - \phi(P_1)} |q|^2,$$

where λ is determined experimentally.

The folding patterns of supine and prone surfaces are highly inconsistent due to the large deformations. Therefore, finding a correspondence for all the feature points on supine and prone is impossible. In our experience, the feature points near the taenia coli (which was used for virtually slicing the colon segment open) are more reliable than those in the middle. Hence, considering only the border feature points will help to overcome the possibility of any incorrectly matched, unwanted features. Thus, our algorithm uses the feature points near the borders rather than those in the middle. Based on the application, any subset of these feature correspondences can be used. Fig. 5(a) shows all of the detected feature points in prone and supine colon segments, and Fig. 5(b) shows the corresponding feature matching in supine and prone colon segments with use of only the border feature points. Table 1 shows the number of correctly and incorrectly matched feature points in different segments of supine and prone colons. Our method is theoretically sound, and we have tested it so far on two colon datasets with good results.

Table 1. Number of feature correspondences in supine and prone colon segments

Colon	Segment	Number of border feature points	Number of feature points correctly matched	Number of feature points incorrectly matched
Prone	Whole	125	114	11
	Ascending	29	28	1
	Transverse	37	34	3
	Descending	27	25	2
	Sigmoid	17	13	4
	Rectum	15	14	1
Supine	Whole	134	114	20
	Ascending	30	28	2
	Transverse	42	34	8
	Descending	31	25	6
	Sigmoid	16	13	3
	Rectum	15	14	1

4 Conclusion

In this paper, we have discussed techniques for the extraction of anatomic landmarks and the detection of feature points on flattened colon segments. Anatomic landmarks, namely, the taeniae coli and the flexures, are automatically located on the supine and prone colon surfaces. These are used for colon flattening and partitioning. The feature points are automatically extracted from the flattened colon surface by use of graph-cut segmentation. Using the graph-matching algorithm, correspondences are obtained between the feature points of supine and prone flattened images. These landmarks and feature points have many uses for a VC system, such as the registration of colon surfaces, virtual navigation, colon flattening, colon partitioning, and polyp bookmarking. In future work, we want to detect more landmarks and feature points on the colon surface for further applications.

Acknowledgments. This work has been supported by NIH grant R01EB7530 and NSF grants IIS0916235 and CCF0702699. The datasets have been provided through the NIH, courtesy of Dr. Richard Choi, Walter Reed Army Medical Center.

References

1. Chowdhury, A.S., Yao, J., Vanuitert, R., Linguraru, M., Summers, R.M.: Detection of Anatomical Landmarks in Human Colon from Computed Tomographic Colonography Images. In: 19th International Conference on Pattern Recognition (ICPR), pp. 1–4 (2008)
2. Lamy, J., Summers, R.M.: Tenia Coli Detection from Colon Surface: Extraction of Anatomical Markers for Virtual Colonoscopy. In: Proc. of the Third Annual Symposium on Visual Computing, pp. 199–207 (2007)

3. Huang, A., Roy, D., Franaszek, M., Summers, R.M.: Teniae Coli Guided Navigation and Registration for Virtual Colonoscopy. In: Proc. of IEEE Visualization, pp. 279–285 (2005)
4. Bitter, I., Kaufman, A.E., Sate, M.: Penalized-Distance Volumetric Skeleton Algorithm. IEEE Trans. on Visualization and Computer Graphics 7(3), 195–206 (2001)
5. Jiang, G., Gu, L.: An Automatic and Fast Centerline Extraction Algorithm for Virtual Colonoscopy. In: Proc. of IEEE Engineering in Medicine and Biology Society (EMBS), pp. 5149–5152 (2005)
6. Boykov, Y., Kolmogorov, V.: An Experimental Comparison of Min-cut/Max-flow Algorithms for Energy Minimization in Vision. IEEE Transactions on Pattern Analysis and Machine Intelligence 26(9), 1124–1137 (2004)
7. Huang, A., Summers, R., Hara, A.: Surface Curvature Estimation for Automatic Colonic Polyp Detection. In: Proceedings of SPIE, pp. 393–402 (2005)

Conformal Geometry Based Supine and Prone Colon Registration

Wei Zeng, Joseph Marino, Xianfeng Gu, and Arie Kaufman

Computer Science Department, Stony Brook University,
Stony Brook, NY 11794, USA
{zengwei,jmarino,gu,ari}@cs.sunysb.edu

Abstract. In virtual colonoscopy, CT scans are typically acquired with the patient in both supine and prone positions. The registration of these two scans is desirable so that the physician can clarify situations or confirm polyp findings at a location in one scan with the same location in the other, thereby improving polyp detection rates and reducing false positives. However, this supine-prone registration is challenging because of the substantial distortions in the colon shape due to the patient's position shifting. We present an efficient algorithm and framework for performing this registration through the use of conformal geometry to guarantee the registration is a diffeomorphism. The colon surface is conformally flattened to a rectangle using holomorphic differentials. The flattened domains of supine and prone are aligned by the harmonic map with feature correspondence constraints. We demonstrate the efficiency and efficacy of our method by measuring the distance between features on the registered colons.

Keywords: virtual colonoscopy, supine-prone registration, conformal geometry.

1 Introduction

Virtual colonoscopy (VC) techniques have been developed as viable non-invasive alternatives to optical colonoscopy (OC) for screening purposes [7, 11]. For a VC procedure, computed tomography (CT) scans of the abdomen are commonly acquired with the patient in both the supine (facing up) and prone (facing down) positions. From these scans, the colon wall can be extracted as in Fig. 1 (a-b) and presented to the VC reader in various ways, including as a volume rendered endoluminal view, mimicking the endoscopic view of an OC, from both supine and prone data.

The use of computer-aided detection (CAD) of colonic polyps [9, 15] can help to reduce the necessary reading and interpretation time of the user and can act as a second reader to improve detection rates of VC. Though various CAD methods can achieve different accuracies, a common problem among them is the presence of false positives. A reduction of these false positives would help the user to focus on true suspicious areas and not waste time on unimportant regions. Throughout the development of VC, the registration of the supine and prone scans has remained a constant and challenging problem [1, 3, 13]. Being able to register these two scans is useful for both a routine VC system and for a CAD system. In the case of a VC

H. Yoshida et al. (Eds.): Virtual Colonoscopy and Abdominal Imaging 2010, LNCS 6668, pp. 113–119, 2011.

system, providing the user the ability to jump from one area in one scan to the same area in the other scan would allow for the easy comparison of these areas when something might be unclear in one of the scans, or for confirming a finding. For a CAD system, a proper registration could help achieve greater accuracy while at the same time reducing false positive results.

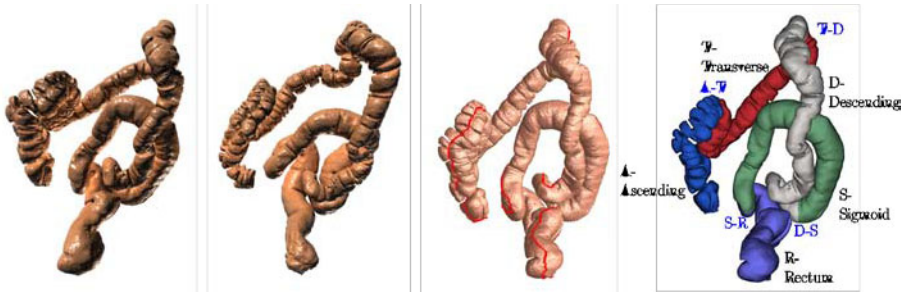

(a) supine (b) prone (c) taenia coli (d) flexures

Fig. 1. Feature extraction of supine-prone colons

In this paper, we present a method of supine-prone registration based on conformal geometry. Conformal colon flattening has been introduced as an enhancement for VC navigation [8] and utilized successfully for CAD [9]. According to conformal geometry theory, there exists an angle preserving map which flattens the colon surface onto a planar rectangle. This mapping minimizes the total stretching energy. Because of the local shape preserving property, it offers an effective way to visualize the entire colon surface, and exposes all of the geometric structures hidden in the original shape embedded in 3D.

The non-rigid elastic deformation between supine and prone colons poses a great challenge for shape registration. In this work, we locate and match the anatomical feature curves (flexures) and internal feature points on the conformally flattened supine and prone surfaces, and compute a harmonic map with these feature constraints. Then, we obtain a diffeomorphism between the supine and prone colons. Our registration method performs better than other existing centerline methods. To the best of our knowledge, it is the first work to apply geometric mapping for supine-prone colon registration by converting the 3D registration problem to a 2D image matching problem.

2 Algorithm Overview

The computational details include the following steps:

1. **Conformal mapping:** A flat rectangular conformal mapping is computed for the colon segments of the supine and prone surfaces using holomorphic differentials (see Fig. 2 (a-b)). As the preprocessing step, we extract the anatomical landmarks (taenia coli and flexures) and use them to decompose the colon surfaces to segments and slice them open, as shown in Fig. 1 (c-d).

2. **Registration:** The supine-prone colon registration is performed using a harmonic map with the feature correspondence constraints. The registration process and results are illustrated in Fig. 2. We extract the internal features and computed the constraints on the conformal mapping images with color encoded mean curvature, using the well-known graph cut segmentation and the graph matching method [2].

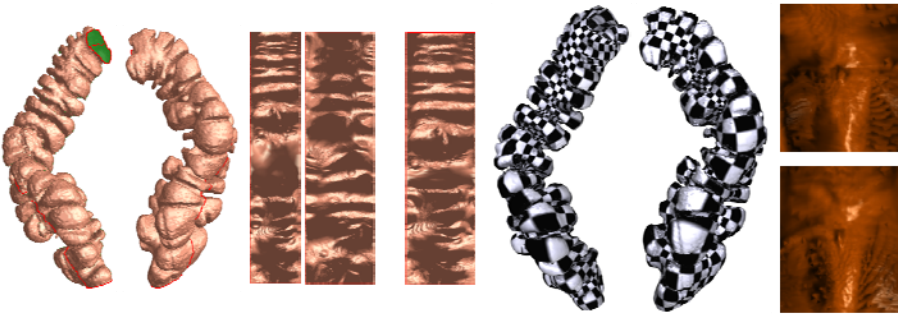

(a) segments A (b) conformal maps (c) registration (d) texture maps (e) polyp views

Fig. 2. Registration for segments *A* of supine (left) and prone (right) colons. The prone segment is the reference for registration; (b) the conformal maps of segments *A* in (a); (c) the result of supine segment registered to prone segment; (d) the checker-board texture mapping for consistency visualization; (e) the volume rendering results for the consistent views of a polyp.

3 Conformal Mapping

This section briefly explains the algorithm for computing the flattened colon by conformal mapping method. The colon surface is a topological cylinder with two boundaries. In practice, all surfaces are approximated by piecewise linear polygonal meshes. Here, we model the colon surfaces as triangular meshes.

Given such a mesh Q, in order to find a conformal mapping $\phi : Q \to \mathbf{C}$, which maps Q to a planar rectangle, we compute two harmonic functions $f_1, f_2 : Q \to \mathbf{R}$ with the Dirichlet boundary conditions [8]. The desired holomorphic 1-form is defined as $\omega = \nabla f_1 + \sqrt{-1}\lambda \nabla f_2$, where ∇f_1 is a closed harmonic 1-form, ∇f_2 is an exact harmonic 1-form, and λ is a scalar, such that $*\nabla f_1 = \lambda \nabla f_2$. The induced conformal mapping $\phi : Q \to \mathbf{C}$ is given by

$$\phi(p) = \int_q^p \omega,$$

where q is the base point and the path from q to p is arbitrarily chosen. Then, the surface is conformally mapped to a planar domain. By tracing the straight line perpendicular to the two boundaries, we obtain a rectangular fundamental domain.

As shown in Fig. 2, the supine and prone colon segments Q_1, Q_2 in (a) are the topological cylinders with two boundaries, cut from the flexures. We slice it open to a topological disk along the taenia coli, which connects the two boundaries. Then, we compute the harmonic functions and holomorphic differentials to conformally map the surfaces to rectangles in (b). The conformal maps are denoted as ϕ_1 and ϕ_2, respectively.

For the theoretical background and computational details about holomorphic differentials, we refer readers to previous works [6, 17, 18, 19].

4 Registration by Harmonic Map

This section explains the details of computing the harmonic mapping between supine and prone colon surfaces for registration purpose. Suppose the feature points are $\{p_0, p_1, \ldots, p_n\}$ on the supine surface and $\{q_0, q_1, \ldots, q_n\}$ on the prone surface, such that p_k corresponds to q_k. In order to enforce the alignments among these internal features, first we use an affine map $\eta : \mathbf{R}^2 \to \mathbf{R}^2$, which maps the rectangle of the supine to that of the prone. Then we compute two harmonic functions, $\mathbf{h} = (h_1, h_2)$, such that

$$\mathrm{h}(p_k) = \phi_2(q_k) - \eta \circ \phi_1(p_k), 0 \le k \le n,$$

and furthermore

$$\Delta h_1 = 0, h_1 \mid_{\gamma_2 \cup \gamma_4} = 0, \frac{\partial h_1}{\partial \mathrm{n}} \mid_{\gamma_1 \cup \gamma_3} = 0,$$

and

$$\Delta h_2 = 0, h_2 \mid_{\gamma_1 \cup \gamma_3} = 0, \frac{\partial h_2}{\partial \mathrm{n}} \mid_{\gamma_2 \cup \gamma_4} = 0.$$

Then, the final registration map from supine to prone $\Phi : S_1 \to S_2$ is given by

$$\Phi := \phi_2^{-1} \circ (\mathrm{h} + \eta \circ \phi_1).$$

Figure 2 shows a registration example of segments A (a) based on such harmonic maps. The prone segment is specified as the reference for registration. Compared to the initial conformal mappings in (b), it is clear that the registration map of the supine segment (c) achieves greater accuracy when using the internal features. The geometry registration is visualized by the consistent checker-board texture mapping in (d). With the motivation of enhancing the polyp detection accuracy, we locate the possible polyps in supine, then jump to the same location in prone and obtain the consistent view through the registration result. In this way, the physician can make more accurate decisions by the double confirmation. The volume rendering in (e) helps demonstrate exact appearance.

5 Experimental Results

We validate our algorithms using real VC colon data from the publicly available National Institute of Biomedical Imaging and Bioengineering (NIBIB) Image and Clinical Data Repository provided by the National Institute of Health (NIH). We perform electronic colon cleansing incorporating the partial volume effect [16], segmentation with topological simplification [9], and reconstruction of the colon surface via surface nets [5] on the original CT images in a pre-processing step. In this paper, the colon surface is modeled as a topological cylinder and discretely represented by a triangular mesh.

We evaluate our registration results by an objective analytic evaluation, whereby distances between corresponding points on the registered colons are calculated. We compute the 3D distance error in millimeters. For the two corresponding points p0 and q0 in R2, we know their locations r0 and s0 in R3. If we take the supine surface (containing p0) as the truth and wish to measure the registration error on the prone surface (containing q0), we can identify the point p1 = (uq, vq) in R2 on the supine surface and similarly its location r1, in R3. The distance error is then given to be | r1 - r0|. Previous works have most often focused on centerline alignment. The ground truth for colon deformation is the whole surface deformation; the centerline only conveys very limited information. Since our method uses this surface instead of the centerline, it is expected that we achieve better results than the cruder centerline methods. Our experiments on 6 pairs of supine-prone colons obtained an average R3 distance error of 7.85mm in terms of (a) the feature points and (b) polyps evaluation. Table 1 shows that our method produces a registration with significantly smaller distance error between corresponding points than other centerline methods with distance error, and similar results to another method based on the registration of haustral folds [4]. Unlike all the other methods, our algorithm provides a one-to-one and onto mapping between the two colon surfaces, allowing for precise localization of corresponding positions whether on a haustral fold or not.

Table 1. Comparison of average millimeter distance error between existing methods

Methods	**Distance Error**
Our Conformal Geometry Based Method	**7.85mm**
Haustral fold registration [4]	5.03 mm
Centerline registration + statistical analysis [12]	12.66mm
Linear stretching / shrinking of centerline [1]	13.20mm
Centerline feature matching + lumen deformation [14]	13.77mm
Centerline point correlation [3]	20.00mm
Taenia coli correlation [10]	23.33mm

6 Conclusion

Shape registration is very fundamental for shape analysis problems, especially for illness and abnormality detection in medical applications. We introduce an efficient

framework for the registration of supine and prone colons, through the use of conformal geometry, to improve the accuracy of polyp detection. Experimental results demonstrate that our registration method performs better than other existing methods. To the best of our knowledge, this is the first work to use the geometric mapping method for the supine and prone colon surface registration problem. In the future, we will investigate the registration for volume data.

Acknowledgements. This work has been supported by NIH grant R01EB7530 and NSF grants IIS0916235 and CCF0702699. The datasets have been provided through the NIH, courtesy of Dr. Richard Choi, Walter Reed Army Medical Center. The work is partially accomplished during the authors' visit to The Math Science Center at Tsinghua University, 2010. We are grateful for the support from the center.

References

1. Acar, B., Napel, S., Paik, D.S., Li, P., Yee, J., Jeffrey Jr., R.B., Beaulieu, C.: Medial axis registration of supine and prone CT colonography data. In: Proc. of Engineering in Medicine and Biology Society (EMBS), pp. 2433–2436 (October 2001)
2. Boykov, Y., Kolmogorov, V.: An experimental comparison of min-cut/maxflow algorithms for energy minimization in vision. IEEE Transactions on Pattern Analysis and Machine Intelligence 26(9), 1124–1137 (2004)
3. de Vries, H., Truyen, R., van der Peijl, J., Florie, J., van Gelder, R.E., Gerritsen, F., Stoker, J.: Feasibility of automated matching of supine and prone CT-colonography examinations. British Journal of Radiology 79, 740–744 (2006)
4. Fukano, M., Oda, T., Kitasaka, Y., Suenaga, T., Takayama, H., Takabatake, M., Mori, H., Natori, S., Nawano, S., Mori, K.: Haustral fold registration in CT colonography and its application to registration of virtual stretched view of the colon. Proc. SPIE Medical Imaging 7624, 1–11 (2010)
5. Gibson, S.F.F.: Constrained Elastic Surface Nets: Generating Smooth Surfaces from Binary Segmented Data. In: Wells, W.M., Colchester, A.C.F., Delp, S.L. (eds.) MICCAI 1998. LNCS, vol. 1496, pp. 888–898. Springer, Heidelberg (1998)
6. Gu, X., Yau, S.-T.: Global conformal parameterization. Symposium on Geometry Processing, 127–137 (2003)
7. Hong, L., Muraki, S., Kaufman, A., Bartz, D., He, T.: Virtual voyage: Interactive navigation in the human colon. In: Proc. of SIGGRAPH, pp. 27–34 (1997)
8. Hong, W., Gu, X., Qiu, F., Jin, M., Kaufman, A.: Conformal virtual colon flattening. In: ACM Symposium on Solid and Physical Modeling, pp. 85–93 (2006)
9. Hong, W., Qiu, F., Kaufman, A.: A pipeline for computer aided polyp detection. IEEE Transactions on Visualization and Computer Graphics 12(5), 861–868 (2006)
10. Huang, D., Roy, M., Summers, R.M.: Teniae coli guided navigation and registration for virtual colonoscopy. Proc. of IEEE Visualization, 279–285 (October 2005)
11. Johnson, D., Dachman, A.H.: CT colography: The next colon screening examination. Radiology 216(2), 331–341 (2000)
12. Li, P., Napel, S., Acar, B., Paik, D.S., Jeffrey Jr., R.B., Beaulieu, C.F.: Registration of central paths and colonic polyps between supine and prone scans in computed tomography colonography: Pilot study. Medical Physics 31(10), 2912–2923 (2004)

13. Näppi, J., Okamura, A., Frimmel, H., Dachman, A., Yoshida, H.: Region-based supine-prone correspondence of false-positive CAD polyp candidates in CT colonography. Academic Radiology 12, 695–707 (2005)
14. Suh, J.W., Wyatt, C.L.: Deformable registration of supine and prone colons for computed tomographic colonography. Journal of Computer Assisted Tomography 33(6), 902–911 (2009)
15. van Ravesteijn, V., Zhao, L., Botha, C., Post, F., Vos, F., van Vliet, L.: Combining mesh volume and streamline representations for polyp detection in CT colonography. In: Proc. of International Symposium on Biomedical Imaging (ISBI), pp. 907–910 (2009)
16. Wang, Z., Liang, Z., Li, L., Li, B., Eremina, D., Lu, H.: An improved electronic colon cleansing method for detection of colonic polyps by virtual colonoscopy. IEEE Transactions on Biomedical Engineering 53(8), 1635–1646 (2006)
17. Zeng, W., Lui, L.M., Gu, X., Yau, S.-T.: Shape analysis by conformal modules. Methods and Applications of Analysis 15(4), 539–556 (2009)
18. Zeng, W., Samaras, D., Gu, X.: Ricci flow for 3D shape analysis. IEEE Transactions on Pattern Analysis and Machine Intelligence 32(4), 662–677 (2010)
19. Zeng, W., Zeng, Y., Wang, Y., Yin, X., Gu, X., Samaras, D.: 3D Non-Rigid Surface Matching and Registration Based on Holomorphic Differentials. In: Forsyth, D., Torr, P., Zisserman, A. (eds.) ECCV 2008, Part III. LNCS, vol. 5304, pp. 1–14. Springer, Heidelberg (2008)

Colon Visualization Using Shape Preserving Flattening

Joseph Marino and Arie Kaufman

Stony Brook University, Computer Science Department,
Stony Brook, NY 11794, USA
{jmarino,ari}@cs.sunysb.edu

Abstract. Virtual colonoscopy is a well-known screening modality for colon cancer, and virtual colon flattening techniques have been proposed to map the 3D surface to the 2D domain. Performing this flattening with conformal geometry allows for the local shapes to be preserved. We explore here how these shape preserving flattened maps can be used for visualization of the colon and to enhance the VC environment. Our discussion focuses on two types of use of the flattened colon, using the flattened mesh alone and using it with integration into the 3D endoluminal view. For the mesh alone, flattened views can be generated using volume rendering to attain the same image quality present in a typical view. When integrated with the 3D endoluminal view, the flattened mesh can be used to assist in navigation through a colon, or in acquiring corresponding view points in two scans if there is a one-to-one and onto mapping between two flattened meshes.

Keywords: virtual colonoscopy, virtual colon flattening, visualization, medical imaging, volume rendering.

1 Introduction

Virtual colonoscopy (VC) has been developed as a non-invasive screening method, whereby a radiologist can explore a colon surface in a way similar to that of a gastroenterologist performing an optical colonoscopy [1]. There has been significant research into a number of alternatives, improvements, and additions for VC systems. Of interest here, virtual flattening techniques have been proposed for the colon surface, whereby the entire colon can be mapped from the 3D domain to a 2D rectangular domain.

A variety of colon-flattening methods have been proposed which will deform a 3D mesh model of the extracted colon to a flat 2D plane. Methods based on cylindrical projections of segments [2] and on mass-spring unfolding have been proposed [3]. Other techniques using conformal mapping have also been suggested [4, 5]. A conformal map of the geometry results in a mapping where local area distortion is minimized while the local angle is preserved, thus preserving the local shape characteristics of the colon surface and providing as undistorted a view of the colon anatomy as possible. Because shape characteristics are of utmost importance in searching for colon abnormalities, we employ conformal geometry for all of our flattening work.

H. Yoshida et al. (Eds.): Virtual Colonoscopy and Abdominal Imaging 2010, LNCS 6668, pp. 120–125, 2011.

These flattened colons can have a variety of uses in a VC system. Other work has focused on using the flattened meshes to encode geometric details (such as curvature) or has simply used traditional computer-graphics mesh rendering to observe the colon surface, whereby the normals for each vertex of the flattened mesh are appropriated from the original 3D colon mesh model. We demonstrate two general categories of using the flattened meshes in a VC system. In the first, we show how volume rendering can be used to give a view similar to that in the endoluminal view. For the second, we demonstrate how the flattened meshes can be used to assist in navigation through the 3D colon view.

2 Generating 2D Views

The flattened colon can be used alone to provide the user with an overview of the entire colon structure, ensuring that all areas are examined and no regions are missed due to folds or other structural obstructions. Because the flattened colon is in fact a mesh surface, conventional polygonal rendering methods have been used to visualize the colon [4]. Rendering the mesh as-is is of course inadequate, as only a rectangle without any structure would be seen. However, the per-vertex normal values from the original 3D colon mesh can be applied to the vertices of the flattened mesh. In this, rendering with lighting will give the sense of the structure of the colon surface. A common way of seeing the surface structure on this flattened mesh is to render with normals that are calculated on the original mesh surface rather than from the flattened mesh (where all normals will of course be in the same direction). Similarly, other geometric properties can also be rendered by encoding of values, such as curvature, as a color at each vertex, with interpolation at render time applying the correct colors across the entire surface.

However, these methods of polygonal rendering do not present to the user the same quality and look that are available in the endoluminal view of a VC system. In such an endoluminal view, the imagery is generated through the use of volume rendering through the original CT data using volumetric ray casting. We want to have this same sort of look and feel in our rendered 2D flattened colons, and thus we map the rendering from the 2D surface to the 3D volume, allowing us to present to the user a volume rendered image on the 2D flattened mesh. For each pixel in the 2D image, the starting position for the ray casting algorithm is given as the corresponding position in the original 3D model, with respect to the local coordinates of the CT volume. Rays are then cast from these points through the colon volume, using an appropriate transfer function to generate the desired image.

To obtain the direction of these rays, a view position must be obtained for each point. As the colon is a long, twisty, tubular structure, a single viewpoint for the entire structure is not feasible. As the flattened colon is created by slicing the colon open along an axis from cecum to rectum, each row of the image is equivalent to a loop on the colon surface. Therefore, by averaging the 3D positions across an image row, we can generate an estimated viewpoint which will be in the center of that row of pixels. Such a viewpoint can be generated along the entire mesh at a resolution

equivalent to that of the desired final rendered image. These view points are then used to obtain the direction vectors inside the volume rendering algorithm. These viewpoints can also be combined through the entire colon to create what we refer to as the *flattened centerline*, which differs from the conventional 3D skeletal centerline extracted for automatic VC navigation [6] (hereafter referred to as *skeleton*). The flattened centerline closely approximates the skeleton, but is more suitable for working with the flattened mesh. Note also that, with our method of conformal flattening [5], the mapping is periodic in the 2D domain, and thus a rectangular final mesh (and image) can be generated, allowing for a much cleaner view than having ragged edges.

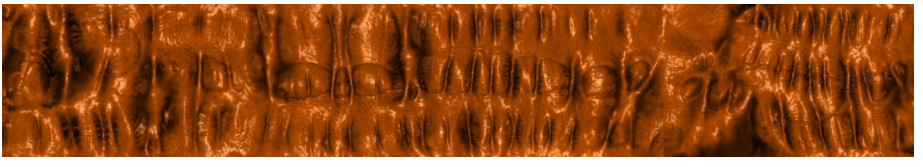

Fig. 1. Volume rendered flattened colon using an opaque transfer function

Rendering with a normal opaque transfer function gives an image of the colon surface as shown in Figure 1. However, more interesting effects are possible. For example, rendering with a translucent transfer function can allow for an electronic biopsy version of the rendering to be presented to the user, wherein density differences within the colon wall can be observed [7]. An example of such a rendered image is shown in Figure 2.

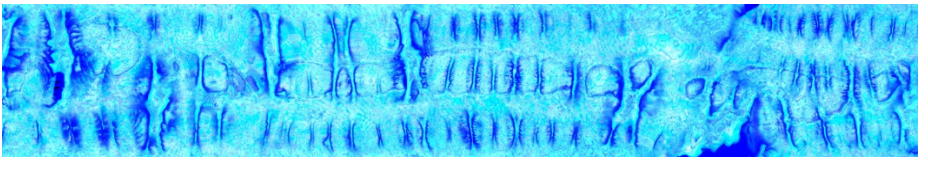

Fig. 2. Volume rendered flattened colon using a translucent transfer function

Viewing flattened colons can also be extremely helpful if there is a registration between two flattened colons that is one-to-one and onto. If such conditions exist, then the two flattened colons will be the same size, and a pixel in one rendered flat colon will correspond directly to the same pixel in the other flat colon. Such a correspondence makes it trivial to observe a region in one colon, and then observe the corresponding region in the other colon.

3 Integration for 3D Navigation

The flattened colon can assist in guiding 3D navigation. The first use is as a general map, whereby the user can select a point on the flattened image, and an endoluminal

viewpoint can be generated to look at the same region. To generate this view, a 3D viewpoint in the endoluminal view is required, as well as the three viewing vectors to orient the camera.

For this, in addition to the volume rendered structural colon image, a hidden image containing the first intersection point of the view ray and the colon wall is created. Selecting a pixel for a point to view on the volume rendered image then maps to selecting the same pixel in this position image, which will have encoded the (x, y, z) position in the 3D colon volume at which the view is to be directed. This point is referred to as p.

The viewpoint can be identified as the point on the flattened centerline for the row containing the selected pixel. If a viewpoint on the skeleton is desired, the closest point on the skeleton to the flattened centerline point can be used. The viewpoint is taken as the optical center of the camera, o. The two neighboring points on the flattened centerline (or skeleton) can be referred to as c_0 and c_1. If desired, several points to the left and right could be averaged to provide a smoother version of the axis.

Using the four points identified above, we can create three view vectors as such:

$$v_0 = \frac{p-o}{|p-o|}, \qquad v_1 = \frac{c_1-c_0}{|c_1-c_0|},$$

$$\upsilon_2 = \upsilon_o \times \upsilon_1$$

where the complete view frame can then be given as $\{o; v_0, v_1, v_2\}$. The vector v_0 is the view vector, formed by looking at the point of interest. Vector v_1 is the ground vector, formed along the flattened centerline (or skeleton). Vector v_2 is the up vector, taken as the cross product of v_0 and v_1.

Flattened views can also be useful if a one-to-one and onto mapping is formed between colon surfaces extracted from two scans. Such a mapping allows for the immediate identification in one scan of the corresponding location from the other scan. This, too, can be used for obtaining corresponding endoluminal viewpoints, similarly to the method described above.

Given a view point o_s on the flattened centerline (or skeleton) in the supine scan, the corresponding view point o_p in the prone scan can be identified (or vice versa). For the supine view, the view vector and up vector intersection points can be identified as s_0 and s_1. The corresponding points on the flattened prone colon can be then be identified as p_0 and p_1. Given these points based on the supine view frame, the three view vectors for the corresponding prone view can be created as such:

$$v_{p1} = \frac{p_0 - o_p}{|p_0 - o_p|},$$

$$v_{p0} = \frac{(p_1 - o_p) \times v_{p1}}{|(p_1 - o_p) \times v_{p1}|},$$

$$v_{p2} = v_{p0} \times v_{p1},$$

where the complete prone view frame can then be given as $\{o_p; v_{p0}, v_{p1}, v_{p2}\}$. As before, v_{p0} is the view vector, v_{p1} is the ground vector, and v_{p2} is the up vector. An example of two corresponding endoluminal views using the flattened maps to generate the matching viewpoints is shown in Figure 3.

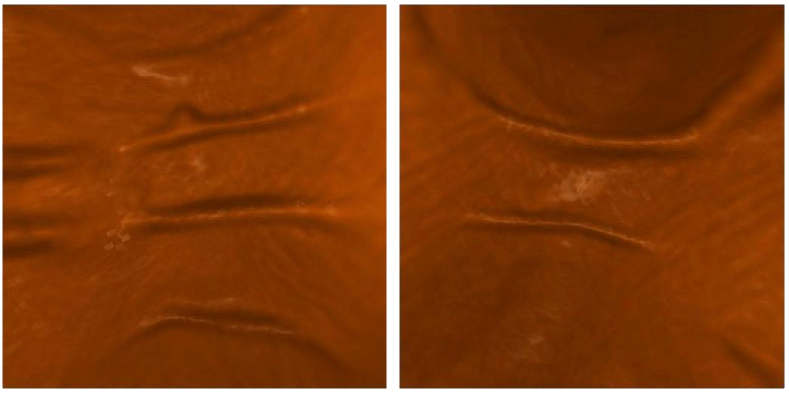

(a) (b)

Fig. 3. Corresponding views from (a) supine and (b) prone position

4 Conclusion

We have demonstrated the visualization possibilities presented by integrating shape-preserving flattened colons into a VC system. Using shape-preserving flattening allows for the flattened mesh to be used directly for visual inspection of the colon surface without obstruction due to haustral folds and bends. By using advanced rendering techniques, volume rendering can be used to generate 2D flattened images which preserve the look and feel of the traditional 3D endoluminal view. Also, the use of volumetric ray-casting allows for other rendering techniques, such as electronic biopsy, to be used.

The flattened mesh is not useful only for its own sake. The flattened colon can be used for integration into the 3D endoluminal view present in the typical VC user interface. The flat colon can be used to guide navigation, whereby a point selected on the flattened colon can be used to generate a corresponding view point in the endoluminal view which will present the same region to the user for inspection. If a correspondence between two flattened colons is present which is one-to-one and onto,

then they can be used as intermediaries to generate corresponding view points between two different scans in the endoluminal views.

In the future, we hope to explore advanced visualization uses of the shape preserving flattened colon meshes. Doctors are currently more used to viewing the endoluminal view than a flattened view, but we are interested in discovering just how useful the flattened view can be and whether doctors would be more likely to make use of it if further enhancements are introduced to tie it into the VC system.

Acknowledgments. This work has been supported by NIH grant R01EB7530 and NSF grants IIS0916235 and CCF0702699. The datasets have been provided through the NIH, courtesy of Dr. Richard Choi, Walter Reed Army Medical Center.

References

1. Hong, L., Muraki, S., Kaufman, A., Bartz, D., He, T.: Virtual Voyage: Interactive Navigation in the Human Colon. In: Proc. of SIGGRAPH, pp. 27–34 (1997)
2. Vilanova Bartroli, A., Wegenkittl, R., König, A., Gröller, E., Sorantin, E.: Virtual Colon Flattening. In: Proc. of VisSym 2001 Joint Eurographics – IEEE TCVG Symposium on Visualization, pp. 127–136 (2001)
3. Umemoto, Y., Oda, M., Kitasaka, T., Mori, K., Hayashi, Y., Suenaga, Y., Takayama, T., Natori, H.: Extraction of Taeniae Coli from CT Volumes for Assisting Virtual Colonoscopy. In: Proc. of SPIE Medical Imaging, p. 69160D (2008)
4. Haker, S., Angenent, S., Tannenbaum, A., Kikinis, R.: Nondistorting Flattening Maps and the 3-D Visualization of Colon CT Images. IEEE Trans. on Medical Imaging 19(7), 665–670 (2000)
5. Hong, W., Gu, X., Qiu, F., Jin, M., Kaufman, A.: Conformal Virtual Colon Flattening. In: Proc. of ACM Symposium on Solid and Physical Modeling, pp. 85–93 (2006)
6. Bitter, I., Kaufman, A.E., Sato, M.: Penalized-Distance Volumetric Skeleton Algorithm. IEEE Trans. on Visualization and Computer Graphics 7(3), 195–206 (2001)
7. Wan, M., Dachille, F., Kreeger, K., Lakare, S., Sato, M., Kaufman, A., Wax, M., Liang, J.: Interactive Electronic Biopsy for 3D Virtual Colonoscopy. In: Proc. of SPIE Medical Imaging, pp. 483–488 (2001)

Synchronized Display of Virtual Colonoscopic Views in Supine and Prone CT Images

Masahiro Oda[1,*], Eiichiro Fukano[2], Takayuki Kitasaka[3], Hirotsugu Takabatake[4], Masaki Mori[5], Hiroshi Natori[6], Shigeru Nawano[7], and Kensaku Mori[1,2]

[1] Information and Communications Headquarters, Nagoya University, Japan
[2] Graduate School of Information Science, Nagoya University, Japan
{moda,efukano}@mori.m.is.nagoya-u.ac.jp
[3] Faculty of Information Science, Aichi Institute of Technology, Japan
[4] Sapporo-Minami-Sanjo Hospital, Japan
[5] Sapporo-Kosei General Hospital, Japan
[6] Keiwakai Nishioka Hospital, Japan
[7] International University of Health and Welfare Mita Hospital, Japan
http://newves.org/~moda/index-e.html

Abstract. Colon diagnosis using CT images of supine and prone positions is time-consuming task because a radiologist has to control viewing fields of virtual colonoscopic (VC) views individually. We propose a method to display VC views of corresponding areas of the colons in the two positions. Viewpoints of VC views in the two positions are obtained by a point interpolation based on the result of the supine-prone correspondence finding. Up-directions of VC views defined based on body orientations of a patient. We generated synchronized VC views of the two positions using the proposed method. Positional difference of the viewpoints between the two positions was 5.03 [mm]. The method can synchronize viewpoints of the supine and prone positions without significant error.

Keywords: CT image, colon, virtual colonoscopic view, supine-prone, synchronization.

1 Introduction

CT-based colon diagnosis known as CT colonography (CTC) has become alternative choice for conventional examination methods [1]. Computer-aided diagnosis (CAD) system for CTC commonly generates virtual colonoscopic (VC) views from 3D CT images. A physician can freely navigate the inside of the colon.

Presence of residue materials in the colon such as fluid or fecal materials on CT images decreases quality and performance of diagnosis. Since fluid, fecal materials, colonic walls, haustral folds, and polyps show very similar CT values, it is difficult to differentiate them on CT images. To reduce areas covered by residue materials, two 3D CT images taken in the supine and the prone positions (two positions) for a patient

* Corresponding author.

H. Yoshida et al. (Eds.): Virtual Colonoscopy and Abdominal Imaging 2010, LNCS 6668, pp. 126–133, 2011.

are used for colon diagnosis. Submerged regions by residue materials can be observed in either of the CT images. However, utilization of the two CT images increases the number of CT images physicians have to refer while diagnosing. An ability to display VC views of corresponding areas of the colons in the two positions (synchronized display) is required for CTC CAD system. Conventional CTC CAD systems cannot perform the synchronized display of VC views. A physician has to manually synchronize the viewing fields of two VC views of the two positions while diagnosing. This is complicated work. Automated synchronized display of two VC views can reduce such load on physicians. To achieve the synchronization, supine-prone registration methods of the colon are utilizable.

Supine-prone registration methods have been proposed by several groups [2– 6]. Huang et al. [2] and Umemoto et al. [3] registered the colons using teniae coli. Their methods, however, cannot deal with shape changes of the colon by stretching and shrinking along the colon centerline. Nappi et al. [4] proposed a registration method using sharply-curved points of the colon centerline as landmarks. Since they establish correspondence at only four points, registration accuracy decreases in the areas distant from the corresponding points. Nain et al. [5] proposed a registration method using dynamic programming. They find correspondence of points on the colon centerlines between two positions using radial distance of the colon and distance along the colon centerline. However, the colon is quite flexible, shape and position of the colon largely change between two patient orientations. Registration accuracy of these methods decrease if the colon shapes change greatly between the two positions. Fukano et al. [6] proposed a method to find positional correspondence between the colons of two orientations based on position and volume of haustral folds. However, synchronized display of the supine and prone views of the colon CT images has not been achieved.

This paper presents a generation method for synchronizing VC views in the supine and the prone positions. We utilize positional correspondence between the colon in the two positions obtained by Fukano's method [6]. Our method synchronizes viewpoints of virtual cameras of the VC views between the two positions to display corresponding points in the both views. Up-direction of the VC view is calculated using body orientations of a patient. We applied the method for generation of synchronized VC views.

In Section 2, we describe synchronization method of VC views in the two positions. Experimental results using the proposed method are shown in Section 3. We add brief discussion in Section 4.

2 Synchronized Supine-Prone Views

2.1 Overview

The proposed method uses 3D abdominal CT images taken in the two positions. Positional correspondence between the colons of the two positions is found by using the method presented in the reference [6]. The proposed method synchronizes viewpoints of virtual cameras of VC views in the two positions based on the

positional correspondence. We briefly describe the method to find correspondence in 2.2, then explain the viewpoint synchronization in 2.3, and calculation of viewing-direction and up-direction of VC view in 2.4.

2.2 Supine-Prone Correspondence Finding

We extract centerpoints $p^s_{i^s}\,(i^s = 1,..., I^s)$ and $p^s_{i^p}\,(i^p = 1,..., I^p)$ forming a colon centerline in the supine and the prone positions from CT images, respectively. I^s and I^p show the total number of centerpoints for the supine and the prone positions, respectively. The method [6] finds correspondence between the centerpoints in the two positions. We represent the correspondence between the centerpoints in the two positions as $c_j = \{(p^s_{t^s_j}, p^p_{t^p_j}) \mid t^s_j \in S, t^p_j \in P\}\ (j = 1,..., J)$, where t^s_j and t^p_j are indices of the centerpoints p^s and p^p, respectively. J is the total number of correspondence between centerpoints. S and P are sets of indices of the centerpoints p^s and p^p that have correspondence found by the method [6].

2.3 Viewpoint Synchronization

We synchronize positions of viewpoints of VC views in the two positions. We use the centerpoints as viewpoints of VC views. Viewpoints in the supine and prone positions are described as $p^s_{i^s}$ and $p^s_{i^p}$ respectively. Since viewpoints at $p^s_{t^s_j}$ and $p^p_{t^p_j}$ are already synchronized by the method [6], we synchronize viewpoints between $p^s_{t^s_{j-1}}$ to $p^s_{t^s_j}$ and $p^p_{t^p_{j-1}}$ to $p^p_{t^p_j}$ by point insertion and a linear interpolation (See Fig. 1). We use a point pair of the centerpoints having the same index number both in the two positions as viewpoint of VC views displayed at the same time. We insert interpolating points to the sequence of centerpoints so that corresponding point pair of the centerpoints have the same index number.

We insert points to the centerpoints using two conditions

$$t^s_j - t^s_{j-1} > t^p_j - t^p_{j-1}, \tag{1}$$

$$t^s_j - t^s_{j-1} < t^p_j - t^p_{j-1}. \tag{2}$$

If the indices of the centerpoints satisfy Eq. (1), we insert $M^p = (t^s_j - t^s_{j-1}) - (t^p_j - t^p_{j-1})$ interpolated points between $p^p_{t^p_{j-1}}$ and $p^p_{t^p_j}$ of the centerpoint in the prone position. The number of the centerpoints between $p^p_{t^p_{j-1}}$ and $p^p_{t^p_j}$ is $N^p = t^p_j - t^p_{j-1} + 1$. Detail of the point insertion is described later. If the

indexes of the centerpoints satisfy Eq. (2), we insert $M^s = (t_j^p - t_{j-1}^p) - (t_j^s - t_{j-1}^s)$ interpolating points between $p_{t_{j-1}^s}^s$ and $p_{t_j^s}^s$ of the centerpoint in the supine position. The number of the centerpoints between $p_{t_{j-1}^s}^s$ and $p_{t_j^s}^s$ is $N^s = t_j^s - t_{j-1}^s + 1$. Schematic illustration of the point insertion is shown in Fig. 1.

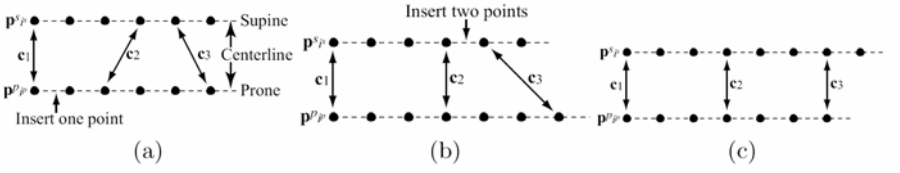

Fig. 1. Insertion of points to the centerpoints. Broken lines are centerlines in the supine and the prone positions. Black circles are centerpoints. Two-headed arrows indicate correspondence $\mathbf{c}_j$. (a) In a range between points corresponded by $\mathbf{c}_1$ and $\mathbf{c}_2$, numbers of points are four in supine and three in prone positions. One (difference of four and three) new point is inserted to prone position. (b) Two new points are inserted to supine position in a range between points corresponded by $\mathbf{c}_2$ and $\mathbf{c}_3$. (c) Centerpoints after the point insertion.

Insertion of M^p interpolating points to the N^p centerpoints in the prone position is performed as follows. We insert median points of $p_{t_{j-1}^p + k\left\lfloor \frac{N^p}{M^p+1} \right\rfloor}^p$ and $p_{t_{j-1}^p + k\left\lfloor \frac{N^p}{M^p+1} \right\rfloor + 1}^p$ $(k = 1,\ldots,M^p)$ to the sequence of centerpoints. Index numbers of all centerpoints having index number $t_{j-1}^p + k\left\lfloor \frac{N^p}{M^p+1} \right\rfloor + 1, \ldots, I^p$ are increased by one. The indices of the inserted points are $t_{j-1}^p + k\left\lfloor \frac{N^p}{M^p+1} \right\rfloor + 1$. This process inserts M^p points to the centerpoint between $p_{t_{j-1}^p}^p$ and $p_{t_j^p}^p$ at equal intervals of the index of the centerpoint. Point insertion to the centerpoint in the supine position is performed similarly.

2.4 Calculation of Viewing-Direction and Up-Direction

A viewing-direction of a VC view $d_{i^s}^s$ at $p_{i^s}^s$ is a unit tangent vector of the centerline at $p_{i^s}^s$.

We calculate up-direction vector of a VC view at each centerpoint $p^s_{i^s}$. Here up-direction means the vector defining the up-direction of VC view in the world coordinate system. An up-direction at $p^s_{i^s}$ is basically obtained by projecting an up-direction at $p^s_{i^s-1}$ to a plane perpendicular to the centerline. However, the up-direction obtained by the projection are quite different between the two positions. We calculate the up-direction that meets the two requirements: (a) angle between the up-direction and a posterior to anterior direction of a patient body is small, and (b) the up-directions at neighboring centerpoints have little difference. The requirement (a) makes upper directions in the two positions similar, and (b) makes smooth viewing field transition while flying-through using VC view along the centerline.

We calculate the up-directions as follows. We represent the up-direction of a VC view at $p^s_{i^s}$ as $u^s_{i^s}$. $\Pi^s_{i^s}$ is a plane perpendicular to the centerline at $p^s_{i^s}$. a^s is a posterior to anterior direction unit vector. We project a^s to $\Pi^s_{i^s}$ and obtain

$$\acute{\mathbf{a}}^s_{i^s} = \frac{\mathbf{a}^s - (\mathbf{a}^s \cdot \mathbf{d}^s_{i^s})\mathbf{d}^s_{i^s}}{\|\mathbf{a}^s - (\mathbf{a}^s \cdot \mathbf{d}^s_{i^s})\mathbf{d}^s_{i^s}\|}. \tag{3}$$

We project $u^s_{i^s-1}$ to $\Pi^s_{i^s}$ and obtain

$$\acute{\mathbf{u}}^s_{i^s} = \frac{\mathbf{u}^s_{i^s-1} - (\mathbf{u}^s_{i^s-1} \cdot \mathbf{d}^s_{i^s})\mathbf{d}^s_{i^s}}{\|\mathbf{u}^s_{i^s-1} - (\mathbf{u}^s_{i^s-1} \cdot \mathbf{d}^s_{i^s})\mathbf{d}^s_{i^s}\|}. \tag{4}$$

We calculate a value which indicates rotation direction by

$$s^s_{i^s} = (\acute{\mathbf{u}}^s_{i^s} \times \acute{\mathbf{a}}^s_{i^s}) \cdot \mathbf{d}^s_{i^s}. \tag{5}$$

Degree of the rotation is obtained by

$$r^s_{i^s} = \begin{cases} \lambda cos^{-1}(\acute{\mathbf{u}}^s_{i^s} \cdot \acute{\mathbf{a}}^s_{i^s}) & if \quad s^s_{i^s} > 0 \\ -\lambda cos^{-1}(\acute{\mathbf{u}}^s_{i^s} \cdot \acute{\mathbf{a}}^s_{i^s}) & if \quad s^s_{i^s} < 0 \\ 0 & otherwise, \end{cases} \tag{6}$$

where λ is a constant which controls degree of the rotation. We rotate $u'^s_{i^s}$ with respect to the rotation axis $d^s_{i^s}$ by $r^s_{i^s}$ degree. Resulting vector of the rotation is defined as $u^s_{i^s}$. We give an up-direction at the beginning point of the centerpoint as $u^s_0 = a'^s_0$. We calculate an up-direction vector $u^s_{i^s}$ at $p^s_{i^s}$ using above equations. Up-direction vectors in the prone position $u^p_{i^p}$ are calculated similarly.

3 Experiments

We implemented the proposed method on a PC platform (CPU: Intel Xeon 3.0GHz×2, Memory: 16GBytes). We generated the synchronized VC views of the

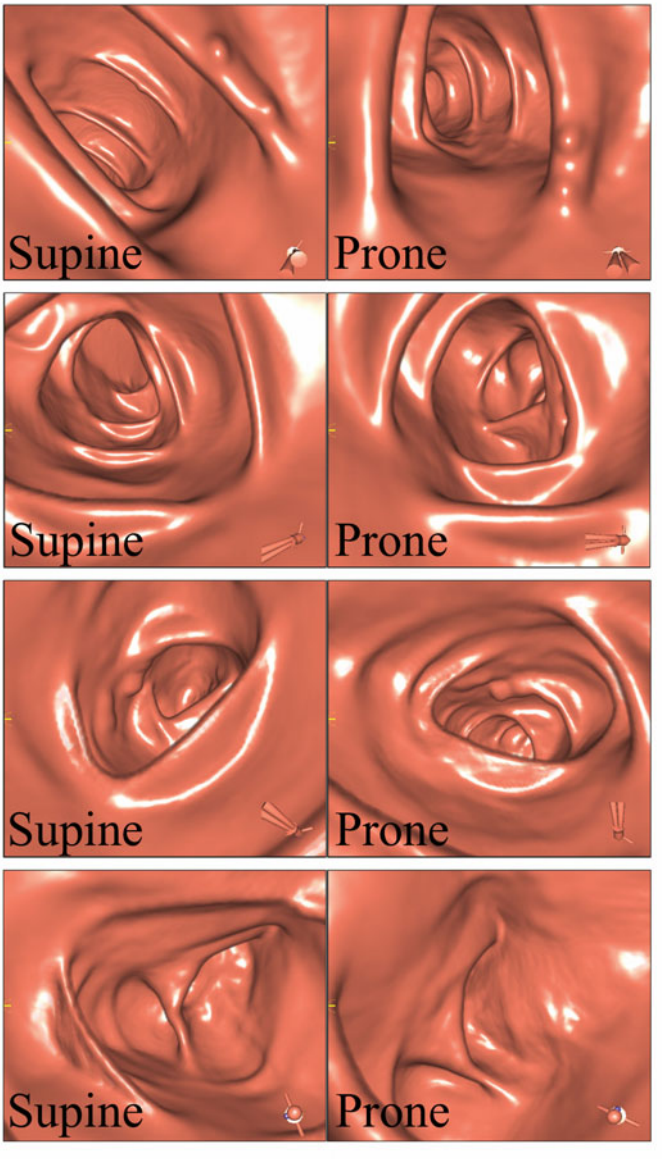

Fig. 2. Synchronized VC views of the two positions. Viewpoints of the views are automatically synchronized by the method.

two positions by a volume rendering method [7]. We evaluated positional difference of the viewpoints of the VC views along the centerlines between the two positions. Six pairs of 3D abdominal X-ray CT images taken in the two positions are used in this experiment. The acquisition parameters of the CT images are; image size: 512×512

[pixels], the number of slices: 405-825, pixel spacing: 0.54-0.70 [mm], slice spacing: 0.50-1.00 [mm], slice thickness: 0.50 [mm]. A parameter is set as $\lambda = 0.01$.

The results of the VC view synchronization are shown in Fig. 2. The views in Fig. 2 are generated using viewpoints, viewing-directions, and up-directions calculated by the proposed method. The method [6] finds correspondence between haustral folds in the two positions. Synchronization error of the viewpoints occurs at a point where the method makes miss-corresponding pair of haustral folds. We calculated positional difference along the centerlines between correct-corresponding pair and miss-corresponding pair for each pair that obtained by the method [6]. The positional difference was 5.03 [mm] in average.

4 Discussion

The synchronized VC views enable us to perform efficient observation of the colons in the supine and the prone positions. The proposed method is applicable for visualization of colon CAD systems. Automated synchronization of observing areas of two views enables seamless switching between CT images taken in the two positions. It reduces time of colon diagnosis using the two CT images.

The proposed method can synchronize viewing fields of VC views in the two positions. From the experimental results shown in Fig. 2, VC views display corresponding area of the colon in the two positions. The positional difference of the corresponding pair obtained by [6] between the two positions was 5.03 [mm]. It is small value enough for observing same region by VC views of the two positions. The proposed method can synchronize viewpoints of VC views without significant error. However, up-directions of VC views are different between the two positions. We employed a posterior to anterior direction of a patient body as up-directions of VC views. Shape of colon changes when a patient changes his/her position. Also, the colon may rotate around the centerline when the position changed. Use of the posterior to anterior direction as up-direction was not result in good synchronization of the up-direction of VC views. Our method need to be improved to synchronize up-direction of VC views based on anatomical features.

5 Conclusion

This paper presented a synchronization method of VC views in the supine and prone positions of a patient. This method finds corresponding viewpoints of VC views in the two positions. Viewing-direction and up-direction of VC view are calculated based on the centerline and the body orientation of a patient. We generated synchronized VC views of the two positions using the proposed method. The positional difference of the viewpoints was 5.03 [mm]. Future work includes calculation of up-direction of VC view based on anatomical feature, evaluation by physicians, and application for colon CAD system.

Acknowledgement. The authors thank our colleagues for suggestions and advices. Parts of this research were supported by the Grant-In-Aid for Scientific Research from the Ministry of Education (MEXT), Japan Society for the Promotion of Science (JSPS), the Japan Society for Promotion of Science, and the Grant-In-Aid for Cancer Research from the Ministry of Health and Welfare.

References

1. Yoshida, H.: Three-dimensional computer-aided diagnosis in ct colonography. Multidimensional Image Processing, Analysis, and Display: RSNA Categorical Cource in Diagnostic Radiology Physics 2005, 237–251 (2005)
2. Huang, A., Roy, D.A., Franaszek, M., Summers, R.M.: Teniae coli guided navigation and registration for virtual colonoscopy. IEEE Visualization, 279–285 (2005)
3. Umemoto, Y., Oda, M., Kitasaka, T., Mori, K., Hayashi, Y., Suenaga, Y., Takayama, T., Natori, H.: Extraction of teniae coli from CT volumes for assisting virtual colonoscopy. Proc. SPIE Medical Imaging 6916, 69160D–1–10 (2008)
4. Nappi, J., Okamura, A., Frimmel, H., Dachman, A., Yoshida, H.: Region-based supine-prone correspondence for the reduction of false-positive cad polyp candidates in CT colonography. Academic Radiology 12(6), 695–707 (2005)
5. Nain, D., Haker, S., Grimson, W.E.L., Cosman Jr, E., Wells, W.W., Ji, H., Kikinis, R., Westin, C.F.: Intra-Patient Prone to Supine Colon Registration for Synchronized Virtual Colonoscopy. In: Dohi, T., Kikinis, R. (eds.) MICCAI 2002. LNCS, vol. 2489, pp. 573–580. Springer, Heidelberg (2002)
6. Fukano, E., Oda, M., Kitasaka, T., Suenaga, Y., Takayama, T., Takabatake, H., Mori, M., Natori, H., Nawano, S., Mori, K.: Haustral fold registration in CT colonography and its application to registration of virtual stretched view of the colon. Proc. SPIE Medical Imaging 7624, 762420–1–11 (2010)
7. Mori, K., Suenaga, Y., Toriwaki, J.: Fast software-based volume rendering using multimedia instructions on pc platforms and its application to virtual endoscopy. Proc. SPIE Medical Imaging 5031, 111–122 (2003)

Colorectal Polyp Segmentation Based on Geodesic Active Contours with a Shape-Prior Model

Haiyong Xu[1,3], H. Donald Gage[2,3], Pete Santago[1,3], and Yaorong Ge[1,3]

[1] Department of Biomedical Engineering
[2] Department of Radiology
[3] Virginia Tech – Wake Forest University School of Biomedical Engineering and Sciences, Medical Center Blvd., Winston-Salem, NC 27157, USA
haxu@wfubmc.edu

Abstract. Automated polyp segmentation is important both in measuring polyp size and in improving polyp detection performance in CTC. We present a polyp segmentation method that is based on the combination of geodesic active contours and a shape-prior model of polyps. To train the shape model, polyps identified by radiologists are grouped by morphologic characteristics. Each group of polyps is used for building a shape-prior model. Then the geodesic active contours method is employed to segment polyps constrained by this shape-prior model. This method can reliably segment polyp boundaries even where the image contrast is not sufficient to define a boundary between a polyp and its surrounding colon tissue. As a pilot study, we developed one polyp shape-prior model for sessile polyps that are located on a relatively flat colon wall. We use the model to segment similar polyps, and the results are evaluated visually.

Keywords: CT colonography, polyp segmentation, geodesic active contours.

1 Introduction

Colorectal cancer is the second leading cause of cancer deaths in United States [1]. Colonoscopy is the current gold standard for the diagnosis of colorectal disorders, including colorectal cancers and their precursors, colorectal polyps. In recent years, CT colonography (CTC) has been shown to offer a minimally invasive alternative to conventional colonoscopy as an effective tool for detecting colorectal polyps. To reduce the interpretation time of the CTC studies and the diagnostic performance dependence on human factors such as experience, fatigue, and perception, computer-aided diagnosis (CAD) systems have been introduced for automatically identifying candidates of colorectal polyps.

A complete description of a colorectal polyp includes both its location and its three-dimensional extent. In CTC-CAD, the process of identifying the location of candidate polyps is usually called *polyp detection*, and the process of determining the extent of polyps is called *polyp segmentation*. Earlier approaches to CTC-CAD mostly focused on polyp detection by use of surface-based geometric features, and the polyp extent was left to the physician to determine visually.

H. Yoshida et al. (Eds.): Virtual Colonoscopy and Abdominal Imaging 2010, LNCS 6668, pp. 134–140, 2011.

More recently, automated methods for polyp segmentation have been proposed as a way to increase the efficacy of colon CAD as well as to provide additional diagnostic information to the radiologist. Specifically, the inclusion of all voxels within the three dimensional extent of polyps would allow new features to be obtained, for example, intensity distribution, volume, and texture. These new features could then be used to improve polyp detection performance. Furthermore, accurate determination of polyp size is important for determining treatment options. Current measurements made by radiologists using the largest apparent dimension are subject to interoperator variability. Computer based generation of polyp size provides a more accurate estimate and removes this variability. Finally, a complete description of a polyp that includes both its location and all voxels that are associated with it is essential for creating a ground truth database for training, testing, and validating CTC-CAD systems.

Polyp segmentation is a challenging task. First, whereas the image intensity difference between a polyp and colon lumen (air) is apparent, the image intensity is quite similar between the polyp and its surrounding colon tissue. The low image contrast in a polyp's baseline region (define the polyp *baseline* region as the non-lumen side of a polyp) makes automated polyp segmentation difficult. Second, polyps vary in shape, size, and location (for example, haustral folds versus the flat colon wall). Thus, a single shape or densitometry template is not sufficient to characterize all polyps.

A number of polyp segmentation methods have been reported in the literature. For example, Jerebko et al. [2] used a Canny operator and the Radon transform to detect polyp boundaries. Yao et al. [3] employed a deformable model and an adaptive deformable model to segment polyps. Tan et al. [4] evolved geodesic active contours with a modified speed function on the colon surface to detect polyp neck regions. Nappi et al. [5] utilized a level-set method to extract the polyp mass region. Lu et al. [6] proposed a classification scheme to segment polyps. Recently, Grigorescu et al. [7] used an LH histogram to determine the threshold that would separate polyps from their surrounding tissue. All of these methods exploited only the image features, for example, intensity, gradient, curvature, etc., which are regarded as local information.

We propose a model-based approach that incorporates prior knowledge of polyp shape into the segmentation process. By incorporating the prior knowledge of polyp shape, our method can reliably segment polyp boundaries even if the image contrast is not sufficient to define the non-lumen side of a polyp or if the initial position of the active contours is far from the polyp center. With our method, accurate measurement of polyp size can be obtained because the pose of a polyp is well-defined after the algorithm converges. In this paper, we present early results of segmenting sessile polyps on relatively the flat colon wall.

2 Method

2.1 Overview

Our segmentation method combines geodesic active contours with a shape-prior polyp model. Geodesic active contours evolve a higher dimensional function such that

the zero active contour converges to the boundary of the object to be segmented. With the addition of a shape-prior model, each step of the evolution also computes the *maximum a posteriori (MAP)* estimation of the position and shape of the polyp. Thus, the active contours evolve globally toward the *MAP* estimate and locally toward optimal image gradients and curvature. Fig. 1 shows the evolution of the zero active contour and the *MAP* estimate of the shape-prior model for five steps in the segmentation process.

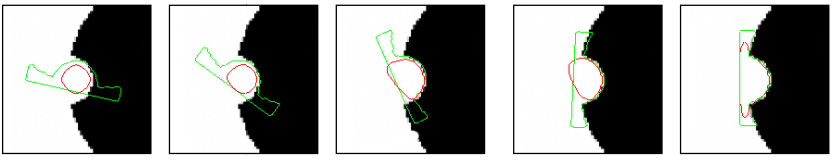

Fig. 1. Evolution of active contour (red curve) and *MAP* estimation of shape-prior model (green curve) in five steps during the segmentation process

Incorporating shape information into geodesic active contours has been described by Leventon et al. [8]. Our method addresses two additional issues pertaining to polyp segmentation. First, there is no strong image contrast support for a large part of the polyp boundary - the polyp baseline area. We draw the polyp baseline in the training samples and modify the algorithm to avoid local minima when a large part of a boundary in an image is obscured. Second, we adaptively change the weights of image features and the shape-prior model during the evolution of active contours to improve reliability.

2.2 Construction of the Shape-Prior Model

The first step in the construction of a shape-prior model is to embed the polyp boundary of each training sample, a closed curve in 2-D and a closed surface in 3-D, as the zero-level set of a higher-dimensional function. The value of this embedding level-set function, u, at each point, x, is the signed distance from x to the nearest point on the boundary, with negative values inside the boundary, positive values outside the boundary, and zero on the boundary. Representing a set of n training samples of polyps using level set functions, we obtain a set of n level-set functions $\{u_1, u_2, ...u_n\}$. Fig. 2 is an example of training samples and a level-set function.

Fig. 2. Example of training samples and a level set function u

Next, we build the shape-prior model over the collection of level-set functions. The mean shape, function μ, is computed as the mean of the n level-set functions. The variance in shape, called mode, is computed by use of principal-component analysis (PCA). The mode v_i is the eigenvector corresponding to the i^{th} largest eigenvalue of the matrix, whose i^{th} column is the vectorized offset function $u_i - \mu$. An approximation of a new shape of the same class of objects can be represented by mean shape μ and k modes: $u_{new} = \mu + \sum_{i=1}^{k} \alpha_i v_i$, where α_i is a coefficient to be determined.

2.3 Polyp Segmentation

Polyp segmentation using geodesic active contours and a shape prior model is an iterative process. Each iteration is carried out in two steps. In the first step, the active contours are evolved under the influence of both image features and the shape-prior model. In the second step, the shape-prior model is deformed and transformed according to the current active contours.

In the first step, the influence of image features is computed using the geodesic active contours [9]. In brief, a contour, which is embedded as the zero level set of function u, is evolved according to the following differential equation, which is a solution to a functional optimization problem [9]:

$$\frac{\partial u}{\partial t} = g(c + \kappa)|\nabla u| + \nabla u \cdot \nabla g$$

where g is a smoothed function of the image gradient, c is a force added to make the contour flow outward, and κ is the mean curvature. Segmenting a polyp with only geodesic active contours will fail because of the weak image contrast support for the boundary between the polyp and its surrounding colon tissue.

In the second step, the shape-prior model is deformed and transformed using the maximum a posteriori (MAP) approach as described in [8]. The shape parameters, $\alpha = \{\alpha_1, \alpha_2, ..., \alpha_k\}$, control the deformation of the shape-prior model. The pose parameters, p, control the translation and rotation of the shape-prior model. We seek to estimate the shape parameters and pose parameters of the final shape by using a MAP approach:

$$\arg\max_{\alpha, p} P(\alpha, p \mid u, \nabla I),$$

where u is the level-set function in the current iteration and ∇I is the image gradient. Let u^* be the estimated final shape, which can be computed from α and p. The probability $P(\alpha, p \mid u, \nabla I)$ is expanded using Bayes' Rule as:

$$P(\alpha, p \mid u, \nabla I) = \frac{P(u, \nabla I \mid \alpha, p) P(\alpha, p)}{P(u, \nabla I)} = \frac{P(u \mid \alpha, p) P(\nabla I \mid \alpha, p, u) P(\alpha) P(p)}{P(u, \nabla I)}$$

The final new active contours are computed as the combination of the image feature influence, v , and the final shape influence $u^* - u(t)$:

$u(t+1) = u(t) + \lambda_1 v + \lambda_2 (u^* - u(t))$, where v is obtained from equation (1).

The authors in [8] use constant weights, λ_1 and λ_2, for these two influences. We find that constant weights are not effective in the polyp baseline region, where image contrast support is weak. In our formulation, we use adaptive weights according to the strength of image features. We would like to make the image features act as a major contributor where there is strong image contrast support, such as the boundary segment between a polyp and colon lumen. But in the image areas where the image contrast support is weak, such as in the polyp baseline region, we would like the shape-prior model to be the major contributor in evolving active contours. Hence we compute the weights as follows:

$$\lambda_1 = \frac{\text{volume inside shape}}{\text{volume inside current contour}} \times \frac{\nabla \mathrm{I}}{1+\nabla \mathrm{I}}, \quad \lambda_2 = \frac{\text{volume inside current contour}}{\text{volume inside shape}} \times \frac{1}{1+\nabla \mathrm{I}}.$$

3 Experiments and Results

We selected five sessile polyps on a relatively flat colon wall as training samples from a database of polyps that were identified by a radiologist in our CTC studies [10]. We built a shape-prior model based on these polyps. We then selected three additional polyps that fall in the same category for testing. The computer segmented polyp boundaries were overlaid in corresponding CT images (Fig. 3) for visual evaluation of the segmentation result.

In constructing a shape-prior model, we extracted a 60x60x60mm^3 sub-volume around the polyp center from the CTC image volume and visualized the colon wall in ParaView (Fig. 3.a, 3.b). Then, we manually generated polyp boundaries based on the training sample polyps (Fig. 3c, 3d). All manually generated polyp boundaries are scaled to a polyp size of 10mm before they are embedded into the level set function. Finally, we used the method described in section 2 to construct the shape-prior model.

To segment a polyp, the user sets the start position by clicking a point inside a polyp. The initial active contour and shape-prior model are centered at the user-clicked point. The active contours are evolved and the shape-prior model is deformed and transformed iteratively. The number of iterations was set at 1000 in this study. The segmentation results (zero-level active contour) and the deformed and transformed shape-prior model are displayed in 3-D and 2-D (Fig. 3). As shown in Fig. 3g and 3k, our segmentation algorithm can not only accurately segment each polyp, but also reliably capture the baseline region of the polyps with the help of a shape prior model. In Fig. 3f/3h and 3j/3l, we can see that the shape-prior model is properly aligned with the polyp. We believe that the transformation parameters for the

shape-prior model offer an added advantage to our method because the model information provides an important framework for further analysis. For example, the polyp orientation determined from the transformed model will be critical for accurate measurement of polyp size.

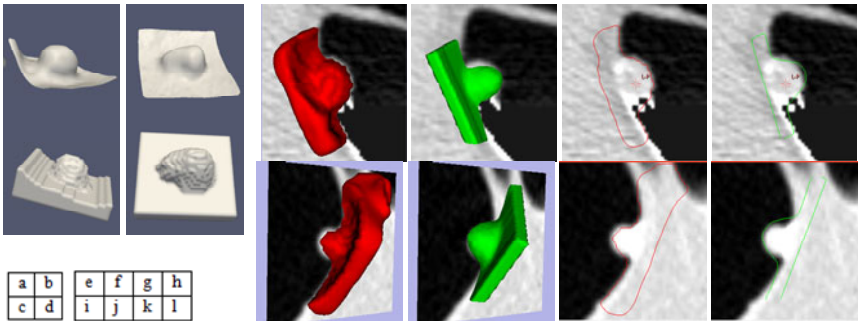

Fig. 3. Left: construction of a shape-prior model (a-d). Right: segmentation results (e-l). The red surface (e, i) and curve (g, k) represent the zero-level active contour, and the green surface (f, j) and curve (h, l) represent the deformed and transformed shape-prior model.

4 Discussion and Conclusions

The size of a polyp may be significantly different for different patients. The shape-prior model, however, is constructed from manually generated polyps with a predefined size (10mm in our experiment). This shape-prior model can be used directly for segmenting ~10mm polyps. In order to segment smaller polyps, e.g., 6mm, or larger polyps, e.g., 15mm, the shape-prior model needs to be scaled down or up before the segmentation process. The scale of the shape-prior model is controlled by a user-specified parameter. For example, one sets the scale equal to 0.6 for small polyps and to 1.5 for large polyps. It will be of great interest in future research to include this scale parameter during the segmentation process and to let the shape-prior model shrink or expand, automatically adapting to the image being segmented.

In Fig. 3g and 3k, which show the original image overlapped with the 2-D segmentation result (red curve), there is a large baseline region in the segmentation result. This is due to the fact that we include a baseline region in our shape-prior model in order to determine the orientation of the shape-prior model to match the polyp orientation in the CT image. During the segmentation process, this baseline region in the shape-prior model is the only force to stop the active contours from expanding around that area in the image. The size of the baseline region in the segmentation result depends on the size of the baseline region in the shape-prior model and the weight parameters λ_1 and λ_2. When $\lambda_1 > \lambda_2$ due to the noise in segmented CT images, there will be a large baseline region in the segmentation results, as is the case shown in Fig. 3g and 3k. However, because the protrusion region in the segmentation result is more important than the baseline region in

calculating the polyp size and other information, this relatively large baseline region will not hinder us from further analysis of the segmented polyps.

In conclusion, we propose a new method for polyp segmentation in CTC that combines geodesic active contours with a shape-prior model. Results from initial experiments demonstrate the effectiveness of this algorithm to segment polyps reliably with low contrast, non-lumen side boundaries. Beside the segmentation result, our method also provides information on polyp orientation, which is important for size measurement and further analysis. In this paper, the shape-prior model is constructed based on few polyps. Further work is under way to include greater number and types of polyps.

References

1. Levin, B., et al.: Screening and surveillance for the early detection of colorectal cancer and adenomatous polyps, A joint guideline from the American cancer society, the US multi-society task force on colorectal cancer, and the American college of radiology. CA: A Cancer Journal for Clinicians 58, 130–160 (2008)
2. Jerebko, A.K., Teerlink, S., Franaszek, M., Summers, R.M.: Polyp segmentation method for CT Colonography computer-aided detection. SPIE Medical Imaging 5031, 359–369 (2003)
3. Yao, J., Summers, R.M.: Adaptive deformable model for colonic polyp segmentation and measurement on CT Colonography. Medical physics 34, 1655–1664 (2007)
4. Tan, S., Yao, J., Ward, M.M., Summers, R.M.: Linear measurement of polyps in CT Colonography using level sets on 3D surfaces. In: Engineering in Medicine and Biology Society, 2009. Annual International Conference of the IEEE, pp. 3617–3620 (2009)
5. Näppi, J.J., Frimmel, H., Dachman, A.H., Yoshida, H.: Computerized detection of colorectal masses in CT Colonography based on fuzzy merging and wall-thickening analysis. Medical physics 31, 860–872 (2004)
6. Lu, L., et al.: Accurate polyp segmentation for 3D CT Colongraphy using multi-staged probabilistic binary learning and compositional model. In: IEEE Conference on Computer Vision and Pattern Recognition, pp. 1–8 (2008)
7. Grigorescu, S.E., et al.: Automated detection and segmentation of large lesions in CT Colonography. IEEE Transactions on Biomedical Engineering 57 (2010)
8. Leventon, M.E., Grimson, F.O.: Statistical shape influence in geodesic active contours. In: Proceedings IEEE Conference on Computer Vision and Pattern Recognition, vol. 1, pp. 316–323 (2000)
9. Caselles, V., Kimmel, R., Sapiro, G.: Geodesic Active Contours. Int. J. Comput. Vision 22, 61–79 (1997)
10. Kimberly, J.R., et al.: Extracolonic findings at virtual colonoscopy: an important consideration in asymptomatic colorectal cancer screening. J. Gen. Intern. Med. 24(1), 69–73 (2009)

Author Index